UNIVERSITY OF CALIFORNIA SAN DIEGO

MICROMAGNETIC MODELING OF THERMAL AND OPTO-MAGNETIC EFFECTS IN NANOMAGNETIC MATERIALS

A dissertation submitted in partial satisfaction of the requirements for the degree Doctor of Philosophy

in

Electrical Engineering (Photonics)

by

Marco Menarini

Committee in charge:

Professor Vitaliy Lomakin, Chair
Professor Eric Fullerton
Professor William Griswold
Professor Vlado Lubarda
Professor Paul Seigel

2020

The Dissertation of Marco Menarini is approved, and it is acceptable in quality and form for publication on microfilm and electronically:

_____

_____

_____

_____

_____

Chair

University of California, San Diego

2020

DEDICATION

To my family and friends.

EPIGRAPH

nos esse quasi nanos gigantium humeris insidentes, ut possimus plura eis et remotiora videre, non utique proprii visus acumine, aut eminentia corporis, sed quia in altum subvehimur et extollimur magnitudine gigantea

Bernard of Chartres

TABLE OF CONTENTS

LIST OF ABBREVIATIONS

σ_+, σ_+, π	Left circularly polarized light, right circularly polarized light, and linearly polarized light
m	Magnetization vector
p, q	Polarization for σ_+ and σ_- light source
d,b,r	Fast decay channels
$B_S(x), L(x)$	Brillouin and Langevin functions
$\widehat{\mathcal{H}}$	Hamiltonian operator
$\hat{\rho}$	Density matrix operator
$\hat{L}_k$	Krauss operator
$\hbar$	Planck constant
ξ_0	Reduced field
γ	Gyromagnetic ratio
T	Temperature
T_e, T_l	Electron bath and lattice bath temperature
T_{amb}	Ambient temperature
T_C	Curie Temperature
λ	Atomistic damping coefficient
$\alpha_{\parallel/\perp}$or $\alpha_{1/2}$	Parallel and perpendicular damping
$\zeta_{1/2}$	Parallel and perpendicular thermal field
H_{eff}	Effective Field

H	Applied Field
H_{eff}	Exchange, Anisotropy, and Magnetostatic Field
$H_E, H_{E,\parallel}, H_{E,\perp}$	Molecular Field, and their longitudinal and transverse projection
J_0	Micromagnetics exchange integral
A	Exchange constant
H_K	Anisotropy field
μ_0	Magnetic moment
$\mu_{14/23}$	Transition dipolar moment
μ_B	Bohr magneton
Γ_d	Coulomb collapse rate
Γ_l	Longitudinal Decay rate
Γ_t	Transverse Decay rate
Γ^*	Pure dephasing
G_l, G_t	Longitudinal and transverse effective Optical Pumping
Ω	Rabi frequency
E^+, E^-	Amplitude of the electrical field of σ_+ and σ_-
I(t)	Optical laser intensity
F(t)	Laser fluence
C_e, C_l, G_{e-l}	Thermal capacity of the electron bath, lattice bath, and thermal exchange between the electron and thermal bath
2TM	Two Temperature model
HAMR	Heat Assisted Magnetic Recording

HD-AOS	Helicity Dependent All Optical Switching
HD-DWD	Helicity Dependent Domain Wall Displacement
FDT	Fluctuation-Dissipation theorem
FP	Fokker-Planck equation
LL	Landau-Lifshitz model
LLB	Landau-Lifshitz-Bloch model
LLG	Landau-Lifshitz-Gilbert model
LLΛ/LLL	Landau-Lifshitz-Λ model
NUFFT	Non-uniform fast fourier transform
GPU	Graphical processor unit

LIST OF FIGURES

LIST OF TABLES

ACKNOWLEDGEMENTS

I would like to acknowledge my advisor Professor Vitaliy Lomakin and Professor Sham for their support and advice. This work would not have been possible without their help. I want to thank all my coauthors and all members of my research team for their valuable suggestions. Finally, I thank all the members of my thesis committee for reading this manuscript and providing valuable feedback.

Chapter 3, in part, is a reprint of material as appeared in M. Menarini, M. V. Lubarda, R. Chang, S. Li, S. Fu, B. Livshitz and V. Lomakin, "Micromagnetic Simulator for Complex Granular Systems Based on Voronoi Tessellation," in Journal of Magnetism and Magnetic Materials (2019). The dissertation author was the primary investigator and author of the text used in this chapter. This work was possible due to the support from the Western Digital Corporation and NSF grants #1117911 and #1202583.

Chapter 4, in part, is a reprint of material as appeared in M. Menarini, R. Medapalli, E. E. Fullerton and V. Lomakin, "Micromagnetic simulation of THz signals in antiferromagnetic FeRh by sub-picosecond thermal pulses," in AIP Advances 9, 035040 (2019). The dissertation author was the primary investigator and author of the text used in this chapter. This work was supported as part of the Quantum-Materials for Energy Efficient Neuromorphic-Computing (Q-MEEN-C), an Energy Frontier Research Center funded by the U.S. Department of Energy, Office of Science, Basic Energy Sciences under Award # DE-SC0019273.

Chapter 5, in part, is a reprint of material as appeared in M. Menarini, L. J. Sham, V. Lomakin, "A Theory of Optoelectronic Reversal of Ferromagnetic Magnetization." currently

being prepared for submission. The dissertation author was the primary investigator and author of this material.

Chapter 7, in part, is a reprint of material as appeared in M. Menarini, and V. Lomakin, "Thermal Fluctuations in The Landau-Lifshitz-Bloch Model." Submitted to Physical Review B and currently in review. The dissertation author was the primary investigator and author of this material.

VITA

2008 B.S in Energy Engineering, University of Bologna, Italy

2010 M.S in Energy Engineering, University of Bologna, Italy

2014 M.S. in Electrical Engineering (Photonics), University of California, San Diego

2020 Ph.D. in Electrical Engineering (Photonics), University of California, San Diego

PUBLICATIONS

M. Menarini, L. J. Sham, V. Lomakin, "A Theory of Optoelectronic Reversal of Ferromagnetic Magnetization." forthcoming

M. Menarini, and V. Lomakin. "Thermal Fluctuations in The Landau-Lifshitz-Bloch Model." *Physical Review B*, submitted

M. Menarini, R. Medapalli, E. E. Fullerton, and V. Lomakin. "Micromagnetic simulation of THz signals in antiferromagnetic FeRh by sub-picosecond thermal pulses." *AIP Advances*, vol 9, no. 3 (2019): 035040.

S. Fu, R. Chang, I. Volvach, M. Kuteifan, M. Menarini, and V. Lomakin. "Block Inverse Preconditioner for Implicit Time Integration in Finite Element Micromagnetic Solvers." *IEEE Transactions on Magnetics* 55, no. 12 (2019): 1-11.

M. Menarini, M. V. Lubarda, R. Chang, S. Li, S. Fu, B. Livshitz, and V. Lomakin. "Micromagnetic simulator for complex granular systems based on Voronoi tessellation." *Journal of Magnetism and Magnetic Materials* 482 (2019): 350-357.

S. Fu, R. Chang, S. Couture, M. Menarini, M. A. Escobar, M. Kuteifan, M. Lubarda, D. Gabay, and V. Lomakin. "Micromagnetics on high-performance workstation and mobile computational platforms." *Journal of Applied Physics* 117, no. 17 (2015): 17E517.

R. Chang, S. Fu, M. V. Lubarda, M. Menarini, and V. Lomakin. "Numerical modeling of heat assisted magnetic recording system." *2014 USNC-URSI Radio Science Meeting (Joint with AP-S Symposium)* (2014): 293-293.

D. Bessette, M. Breschi, C. Calzolaio, A. Devred, M. Menarini, and K. Seo. "Sensitivity analysis of Tcs measurement on ITER TF conductors." *IEEE Transactions on Applied Superconductivity* 20, no. 3 (2010): 1488-1491.

CONFERENCE PRESENTATIONS

M. Menarini, and V. Lomakin. "Thermal Fluctuations in the Landau-Lifshitz-Bloch equation" *2019 Annual Conference on Magnetism and Magnetic Materials*, Las Vegas, NV, USA, Nov 4-8, 2019.

M. Menarini, R. Medapalli, V. Lomakin, and S. Mangin. "Simulation of Optical Reversal and Domain Wall Displacement Using the Landau Lifshitz Lambda Model." *2018 Joint MMM-Intermag Conference*, Washington, DC, USA, Jan 14-18, 2019.

M. Menarini, R. Medapalli, E. Fullerton, and V. Lomakin. "Macromagnetic Simulation of THz signals in antiferromagnetic FeRh by ultrafast thermal pulses" *2018 Joint MMM-Intermag Conference*, Washington, DC, USA, Jan 14-18, 2019.

M. Menarini, P. Scheid, R. Medapalli, Y. Quessab, S. Mangin, and V. Lomakin. "Simulations of All-Optical Switching and Domain Wall Displacement in a Ferromagnetic material" *21st International Conference on Magnetism*, San Francisco, CA, Jul 15-20, 2018.

M. Menarini, P. Scheid, S. Mangin, and V. Lomakin. "Modeling of All-Optical Domain Wall Displacement in Ferromagnets Using a Three-levels Landau-Lifshitz Dynamics" *61st Annual Conference on Magnetism and Magnetic Materials,* Pittsburgh, PA, Nov 6-10, 2017.

M. Menarini, L.J. Sham, and V. Lomakin. "Modeling All Optical Switching in Granular FePt." *61st Annual Conference on Magnetism and Magnetic Materials*, New Orleans, LA, Oct 31-Nov 4, 2016.

M. Menarini, V. Lomakin, B. Livshitz, K. Eason, and E. Champion. "Analysis of HAMR using Landau-Lifshitz-Bloch and Xu-Zhang formulation" *13th Joint MMM-Intermag Conference*, San Diego, CA, USA, Jan 11-15, 2016

M. Menarini, V. Lomakin, E. E. Fullerton, L.J. Sham, P. Mangin, S. Fu, and D. Gabay. "Modelling of All Optical Switching by circular polarized laser pulses in granular FePt media" 59th Annual Conference on Magnetism and Magnetic Materials, Honolulu, HI, Nov 3-7, 2014.

M. Menarini, M. Lubarda, B. Livshitz, S. Mangin, E. Fullerton, V. Lomakin, "Modeling high-temperature demagnetization and recording in FePt granular media," *IEEE International Magnetics Conference*, Dresden, Germany, May 4-8, 2014.

FIELD OF STUDY

Major Field: Electrical Engineering

Sub-fields: Photonics, Thermal dynamics

ABSTRACT OF THE DISSERTATION

MICROMAGNETIC MODELING OF THERMAL AND OPTO-MAGNETIC EFFECTS IN NANOMAGNETIC MATERIALS

by

Marco Menarini

Doctor of Philosophy in Electrical Engineering (Photonics)

University of California, San Diego, 2020

Professor Vitaliy Lomakin, Chair

Magnetic materials are vital components of many existing and future applications, ranging from data storage and spin-logic devices, to terahertz sensors and artificial synapses from neuromorphing computing. Driven by the need to faster responses and high-density storage, the focus of this work is the modeling of thermal and optical excitation of magnetic materials by an external laser source.

Many models focus on the use of fields or current as the primary driving force behind the change in magnetization and the models, without taking into account the optical contribution of the light, which has been shown to produce changes in magnetizing on a faster timescale than the ones observed with the use of either current or field.

Moreover, granular media, which are at the core of many magnetic materials, are usually modelled using simplistic finite difference approach or numerically intensive finite-elements

approach to model every grain. These approaches lead to either an unrealistic description of the media or to an over-sampling of the geometrical nodes of the problem, increasing significantly the computational time required to run the simulations.

This dissertation improves upon the state of the art of micromagnetic modelling by introducing a Voronoi tessellation model to simulate realistic granular structures at elevated temperature for high anisotropy materials. This approach considers the geometry of the grains for computing the far-field contribution. The approach has been proven effective in modeling realistic media for heat assisted magnetic recording and perpendicular media in general. The model presented also introduces in the dynamics of the magnetizing optical contributions and helps describe complex phenomena, such as the ultrafast-demagnetization and the helicity dependent optical reversal of magnetic material subjected to an external optical source.

While the model provides a qualitative interpretation of the experiments, additional data is required to evaluate the quantitative contribution of the optical excitation and the correctness of the thermal fluctuations.

This dissertation is structured as follow. In Chapter 1 and 2 introduce key concepts of magnetism and the basic micromagnetic model that is used as the basis for the numerical simulations.

Chapter 3 introduces a micromagnetic code based on Voronoi tessellation and the non-uniform fast Fourier transform (NUFFT) method. The code is capable of efficiently and accurately simulating magnetization dynamics in large and structurally complex granular systems, such as multilayer granular media used for perpendicular magnetic recording, bit patterned media, granular nanowires, and read heads. In these systems the granular microstructure and distributions in grain and interface properties play an important role in

device performance. The presented Voronoi simulator allows comprehensive studies to be performed as it accounts for the detailed granular microstructure and distributions that characterize true systems. Simulation time is greatly reduced by the NUFFT algorithm and implementation on graphics processing units (GPUs). Simulations of conventional magnetic recording, heat-assisted magnetization reversal, domain wall dynamics in granular nanowires, and particulate tape recording are presented.

Chapter 4 explores the generation of electromagnetic field signals in the terahertz frequency (THz) range using antiferromagnets (AFM). Using micromagnetic model simulations, we investigated a potential mechanism for laser-induced THz signals in the AFM phase of FeRh/Pt bilayer films. In the simulations, FeRh films are modelled as two Fe-sublattices coupled via intra-lattice exchange field and subjected to a sub-picosecond thermal pulse. Our simulations expose a partial canting between the magnetizations of two Fe-sublattices, within the first picosecond after the excitation. This short-lived state relaxes abruptly into the initial AFM phase, injecting a spin current into the Pt layer via spin pumping, which is eventually converted into charge current oscillating at THz frequency.

Chapters 5 and 6 discuss the phenomenon of all-optical switching of the magnetization in magnetic nanostructures. While all-optical switching of the magnetization in magnetic nanostructures by femtosecond circularly polarized laser pulses without an external magnetic field has been demonstrated in several systems, a theoretical framework that convincingly explains the phenomenon is still missing. In Chapter 5 we propose a theory where the ferromagnetic macrospin ground state is optically excited by the circularly polarized light to a spin reversed state, which is then “Coulomb collapsed” to the magnetization reversed ground state. The optical excitation lasts for the duration of the laser pulse and the system relaxes at a

fast rate due to the electron-electron interaction. In Chapter 6, we present a computational model based on this theory. We construct a three-state model for the magnetization dynamics, the Landau- Lifshitz-Lambda (LLL) model, as an ensemble of such states to account for the temperature effects. After the optical excitation lapses, the LLL model reduces to the Landau-Lifshitz-Bloch (LLB) formulation, allowing to consider the magnetization relaxation dynamics at elevated temperatures. We apply the theory to simulate all-optical switching (AOS) in FePt films subject to multiple femtosecond circular polarized laser pulses. The simulation results demonstrate characteristic AOS features and agree with recent experiments.

Chapter 7 identifies problems in the performance of the established stochastic model in micromagnetics in modeling the thermal fluctuations of longitudinal and transverse components of the magnetization at elevated temperature. A correct estimation of the thermal fluctuation is paramount to develop multiscale atomistic-micromagnetic models. The chapter presents a consistent solution for the diffusion coefficients that satisfy the corresponding Fokker-Planck equation and provide the correct equilibrium magnetization at elevated temperature.

Finally, Chapter 8 contains concluding remarks and an outlook on future research.

CHAPTER 1 - INTRODUCTION

This chapter presents a brief overview of magnetism. The discussion starts with the introduction of the basic concepts of magnetism and the basic concepts that are used later in the dissertation to develop the micromagnetic code to study the optical and magnetic interactions in complex granular systems and films, including the concepts of magnetism and molecular field that are used in the following chapters to develop a micromagnetic model to simulate optical and thermal effects on nanomagnetic materials.

1.1 BASIC CONCEPTS OF MAGNETISM

It is known from the experiments that a material subjected to a magnetic field $\mathbf{H}$ may acquire a magnetic moment $\boldsymbol{\mu}$. The average magnetic moment per unit volume is defined as magnetization and it is denoted by the vector $\mathbf{M}$. The relationship between the magnetization and the applied field may in some cases be described by the relationship:

$$\mathbf{M} = \chi \mathbf{H} \ , \tag{1.1}$$

where χ is the magnetic susceptibility. If the magnetic moments align in the direction of $\mathbf{H}$ (i.e. $\chi > 0$) the material is classified as paramagnetic. If the magnetic moment align in the direction opposite of $\mathbf{H}$ (i.e. $\chi < 0$), the material is classified as diamagnetic. In many practical cases, it is inappropriate to consider the susceptibility χ as a constant. For high enough fields, the relationship between $\mathbf{M}$ and $\mathbf{H}$ approaches a finite saturation value M_S called saturation magnetization.

Some material, however, do not follow the relationship given by Eq. (1.1). The most common example are ferromagnets in which a spontaneous magnetization persists

macroscopically even in the absence of an applied field $\mathbf{H} = 0$. In this kind of materials, the magnetization is not a one valued function of $\mathbf{H}$ and its value is a function of the history of the applied field.

The susceptibility χ is proportional to the inverse of the temperature, (i.e. $\chi \propto 1/T$). In ferromagnetic materials, the spontaneous magnetization decreases as the temperature is increased to a critical value T_C , known as Curie temperature. Above T_C, a ferromagnet behaves as a paramagnetic material. In 1907, Pierre Weiss theorized that the interaction between magnetic molecules, described as a "molecular field", could act on the magnetization as an external field generating a spontaneous magnetization.

The magnitude of this field was assumed proportional to the magnetization itself and to a material dependent parameter $\mathbb{N}$. Thus, the magnetization could be expressed as:

$$M = f\left(\frac{H + \mathbb{N}M}{T}\right), \tag{1.2}$$

where f is an odd function of its argument. At high temperature, the value of f can be replaced by the leading term of the Taylor series:

$$M \approx \frac{C}{T}\left(H + \mathbb{N}M\right), \tag{1.3}$$

where C is the material dependent Curie constant. From Eq. (1.3), it is possible to predict a Curie temperature at $M/H = \infty$. Equation (1.1), can then be rewritten, using Eq. (1.3), in the form of the Curie-Weiss law that is followed qualitatively by all ferromagnets:

$$\chi = \frac{M}{H} = \frac{C}{T - T_C}, \tag{1.4}$$

where $T_C = C\mathbb{N}$.

It is important to note that the Weiss assumption of a molecular field is sufficient to both explain the paramagnetic behavior above the Curie temperature and the temperature dependence of the magnetization. In order to explain the field dependence, Weiss assumed the existence of several small domains, each one of them magnetized to its saturation value $M_S(T)$, but which direction varies domain to domain. The applied field rotates these domains into its own direction, and for a large enough field, the overall magnetization would be equal to the saturation value.

It is important to note that to understand the origin of the molecular field, it is necessary to use quantum physics, since in pure classical physics, the electrons do not interact with an applied field. The shortcoming of a pure classical approach can be shown by considering the Bohr-Van Leewen theorem as shown by John Hasbrouck Van Vleck [1] that says: "for classical non relativistic electron, at any finite temperature, and in all finite applied electrical or magnetic fields, the net magnetization of a collections of electrons in thermal equilibrium vanishes identically".

To prove the theorem, let us consider a classical system of N electrons. Their behavior is described by 3N coordinates, q_i , and their 3N momenta, p_i . If each electron has a charge e. A free electron moving with velocity $\mathbf{v}$ creates a current density $\mathbf{j} = e\mathbf{v}$ and a magnetic moment:

$$\boldsymbol{\mu} = \frac{1}{2c}\mathbf{r} \times \mathbf{j} = \frac{e}{2c}\mathbf{r} \times \mathbf{v} \ , \tag{1.5}$$

where c is the speed of light and $\mathbf{r}$ represent their position is space. Since from Eq. (1.5), the magnetic moment of a single electron is a linear function of the $\mathbf{v}$, the total magnetic moment $\mathbf{m}$ is a linear function of all the electron velocities. Thus, it is possible to define the total magnetic moment along the direction z as a function of the form:

$$m_z = \sum_{i=1}^{3N} a_i^z(q_1, q_2, \ldots, q_{3N})\dot{q}_i \ , \tag{1.6}$$

where the coefficients a_i^z are a function of the position of all the electrons q_i , but not of their momenta, and the velocity is defined as the derivative of the position in time (i.e. $\dot{q}_i = v_i$). The canonical equation of a classical motion is:

$$\dot{q}_i = \frac{\partial \mathcal{H}}{\partial p_i} \qquad \dot{p}_i = -\frac{\partial \mathcal{H}}{\partial q_i} \ . \tag{1.7}$$

The Hamiltonian $\mathcal{H}$ for electron and magnetic field is defined as:

$$\mathcal{H} = \underbrace{\sum_{i=1}^{3N} \frac{1}{2m_e}\left(\mathbf{p}_i - \frac{e}{c}\mathbf{A}_i\right)}_{\text{kinetic energy}} + \underbrace{eV(q_1,\ldots.q_{3N})}_{\text{potential energy}} \ . \tag{1.8}$$

where m_e is the mass of the electron, $\mathbf{A}_i$ is the magnetic vector potential, and eV is the potential energy due to the interaction of the electrons among themselves and with any other fixed potential. Using Eq.(1.8) we can rewrite Eq. (1.6) as:

$$m_z = \sum_{i=1}^{3N} a_i^z(q_1, q_2, \ldots, q_{3N}) \frac{\partial \mathcal{H}}{\partial p_i} \ . \tag{1.9}$$

The thermal average of a classical system is obtained using the Maxwell-Boltzmann distribution as:

$$M_z = \frac{\int m_z exp(-\beta\mathcal{H}) dq_1 \ldots dq_{3N} dp_1 \ldots dq_{3N}}{\int exp(-\beta\mathcal{H}) dq_1 \ldots dq_{3N} dp_1 \ldots dq_{3N}} \ . \tag{1.10}$$

Using Eq. (1.9) in Eq. (1.10), we can see that for every electron, each of the components in the sum of m_z is proportional to:

$$\int_{-\infty}^{\infty} \frac{\partial \mathcal{H}}{\partial p_i} \exp\left(-\beta\mathcal{H}\right) dp_i = -\frac{\exp\left(-\beta\mathcal{H}\right)}{\beta}\bigg|_{p_i=-\infty}^{\infty} = 0 \ . \tag{1.11}$$

The integral in Eq. (1.11) disappear for all p_i, since the Hamiltonian is proportional to p_i^2 for large values of $|p_i|$. We can see how, for a purely classical system, there is no magnetic moment

for any applied field. Thus, in the classical model no interaction between electrons and field is possible. Thus, a semi-classical approach is required to explain the origin of magnetism.

1.2 QUASI-CLASSICAL THEORY OF MAGNETISM

As seen in the previous paragraph, a pure classical theory of magnetism is not able to explain the basic concept of magnetism. Classical electrons, for example, cannot move around the atom orbit without radiating energy and collapsing into the center. On the other hand, using a purely quantum mechanical approach would only be practically applicable to simple ferromagnetic systems.

It is usually preferred to use a hybrid approach to magnetism where the results obtained from quantum mechanics are applied to the classical theory. To do so, some assumption needs to be made:

1) A semi-classical electron can orbit around the nucleus without collapsing.
2) The electrons have a quantum spin that only assume discrete values.
3) The spins are treated as classical vectors and interact between each other and with an external field.

Under these assumptions, we can consider an ensemble of atoms each one with a fixed magnetic moment $\boldsymbol{\mu}$. The unit of the magnetic moment is given by the Bohr magneton:

$$\mu_B = \frac{e\hbar}{2m_e c} = 0.927 \times 19^{-20} \text{ erg/G} \ , \tag{1.12}$$

where $\hbar$ is the Plank constant and m_e is the mass of the electron. The magnetic moment experienced by each atom is given by:

$$\mu_0 = g\mu_B S \ , \tag{1.13}$$

where g is the Landé factor and S_z is the is the projection of the spin along z. One of the properties of the quantum spin is that its projection along z, S_z, can only assume discrete values

$(-S, -S+1, \ldots, S)$. If the spins do not interact with each other but only with the applied field (*paramagnetic materials)*, it is possible to write the energy of system as:

$$E(\mu) = -\boldsymbol{\mu} \cdot \mathbf{H} \ . \tag{1.14}$$

If we assume $H = H_z$, we can write the integral of Eq.(1.10) as a sum over all the possible configuration of S_Z :

$$\langle m_z \rangle = \frac{\sum \mu_z e^{-\beta m_z H}}{\sum e^{-\beta m_z H}} = \frac{\sum_{n=-S}^{S} g\mu_B n e^{-g\mu_b n\beta H}}{\sum_{n=-S}^{S} e^{-g\mu_b n\beta H}} = \frac{\sum_{n=-S}^{S} g\mu_B n \varsigma^n}{\sum_{n=-S}^{S} \varsigma^n} \ , \tag{1.15}$$

where the last form of the equation has been obtained by introducing the geometric series:

$$\begin{aligned} \sum_{n=-S}^{S} \varsigma^n &= \frac{\varsigma^{-S} - \varsigma^{S+1}}{1-\varsigma} \\ \sum_{n=-S}^{S} n\varsigma^{n-1} &= \frac{S(\varsigma^{S+1} - \varsigma^{-S-1}) - (S+1)(\varsigma^S - \varsigma^{-S})}{(1-\varsigma)^2} \end{aligned} \ . \tag{1.16}$$

Substituting the relationship in Eq. (1.16) into (1.15), and using the relationship between hyperbolic functions, we obtain the value of the average magnetization along z:

$$\langle m_z \rangle = \frac{\langle S_z \rangle}{S} = \frac{2S+1}{2S} \coth\left(\frac{2S+1}{2S}\xi_0\right) - \frac{1}{2S}\coth\left(\frac{\xi_0}{2S}\right) = B_S\left(\xi_0\right) \ . \tag{1.17}$$

The relationship obtained in Eq. (1.17) is the Brillouin function, B_S , and its value is a function of both the spin number S and the reduced field:

$$\xi_0 = \frac{\mu_0 H}{T} \ . \tag{1.18}$$

In the classical limit, we can assume that the momentum align continuously with the field and S can assume all possible values (i.e. $S \to \infty$). This leads to a simplified form of $B_S(\xi_0)$ known as Langevin function $L(\xi_0)$:

$$\langle m_z \rangle = L(\xi_0) = \coth(\xi_0) - \frac{1}{\xi_0} \ . \tag{1.19}$$

The Langevin function and the Brillouin function describes the average magnetization of a paramagnetic particle subjected to an external field. It can be shown that for small values of H or elevated values of T (i.e. $\eta \ll 1$), the Brillouin and the Langevin function can be expressed as:

$$\begin{aligned} B_S(\eta) &= \frac{(S+1)}{3S}\eta + O(\eta^3) \\ L(\eta) &= \frac{\eta}{3} + O(\eta^3) \end{aligned} \ . \tag{1.20}$$

Thus, if the field is small enough the magnetization can be described by the first term of the Taylor series in Eq. (1.20). In most cases of interests, the magnetization induced by an external field does not deviate from the linear behavior even for the largest applied field. We can then define a linear susceptibility, as the one defined in Eq. (1.1):

$$\chi = \lim_{H\to 0} \frac{\partial \langle M_z \rangle}{\partial H} = \lim_{H\to 0} \frac{\partial N g \mu_b \langle S_z \rangle}{\partial H} = \frac{C}{T} \ , \tag{1.21}$$

where N is the number of spins per unit of volume, and the Curie-Weiss constant is given by

$$C = \frac{N(g\mu_B)^2}{3k_B} \begin{cases} S(S+1) & \text{for the Brillouin function} \\ 1 & \text{for the Langevin function} \end{cases} \ . \tag{1.22}$$

For very large values of the argument (i.e. $\eta \gg 1$), the magnetization reaches saturation $B_S(\infty) = L(\infty) = 1$. This means that all the spin contains in the volume V are aligned in the direction of the external field. In fact, the presence of a magnetic field only changes the direction of the individual spins but not their magnitude. In paramagnetic materials, the Curie-Weiss constant is proportional to the spin number of the single atom, thus the effective susceptibility, and the field required to reach the saturation magnetization at room temperature is of the order of ~ 100 T, much larger than the field commonly used in experiments. Normally, any ferromagnetic and ferrimagnetic material, undergoes a transition to a paramagnetic state when $T \geq T_C$. However,

it is possible for ferro- and ferri-magnetic nanoparticles to form large domains even below the Curie temperature while having overall zero magnetization. The effective spin value of each nanoparticle is given by the sum of the spin in each atom and can reach values of the order of $S \sim 10^3 - 10^4$. When this happen, the material is said to be in the *superparamagnetic* state and saturation can be obtained for small values of the field.

1.3 MOLECULAR FIELD

In practice, we usually are interested in the case where the atoms interact with each other and not only with an external magnetic field. We now consider a simplified case, where the total energy of the system is due to both the exchange interaction between the spins S_i and S_j, and the applied field:

$$E = -\sum_{ij} J_{ij} \mathbf{S}_i \cdot \mathbf{S}_j - \sum_i g \mu_B \mathbf{S}_i \cdot \mathbf{H} \ , \tag{1.23}$$

where J_{ij} is the exchange integral. If $J_{ij} > 0$ the energy of the system is minimized when the spin are parallel (ferromagnetic coupling), and if $J_{ij} < 0$ the energy of the system is minimized when the spin are anti-parallel (antiferromagnetic coupling). In general, the value of J_{ij} can be positive or negative for different sites i and j. The intensity of the exchange integral varies with the distance, so we can have different value for the nearest neighbor $J_{\langle 001 \rangle}$ and the next-nearest neighbors $J_{\langle 011 \rangle}$. If both $J_{\langle 001 \rangle}$ and $J_{\langle 011 \rangle}$ are greater than zero (Figure 1.3-1a) the material is a ferromagnet, if $\left|J_{\langle 001 \rangle}\right| > \left|J_{\langle 011 \rangle}\right|$ with $J_{\langle 001 \rangle} < 0$ and the magnetic moment of the atoms is compensated, the material is an antiferromagnet (Figure 1.3-1b), if the moment of the atoms is not compensated, the material shows a non-zero total magnetization at the equilibrium and it shows ferrimagnetic behavior (Figure 1.3-1c).

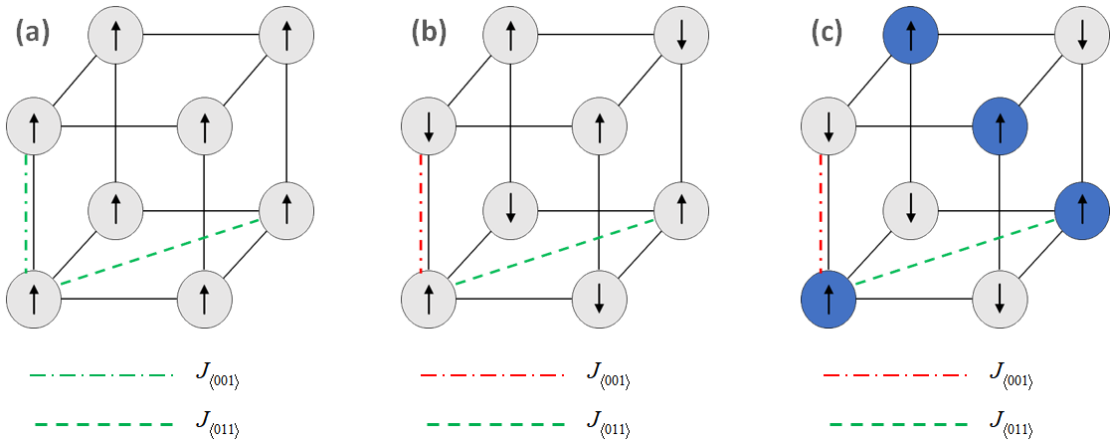

Figure 1-1: Ferromagnetic $J_{ij} > 0$ (green line) and antiferromagnetic $J_{ij} < 0$ (red lines) coupling for the nearest neighbor $J_{\langle 001\rangle}$ (dash-dotted line) and next-nearest neighbor $J_{\langle 011\rangle}$ (dashed line). The figure show the case of (a) ferromagnetic lattice with a single type of atoms, (b) antiferromagnetic lattice where the momentum of the atoms is compensated and the total momentum is zero, and (c) ferrimagnetic lattice where the two sublattice momentum (blue and grey atoms) has different values that leads to a non-zero magnetization.

In practice, computing the exchange interaction directly for a finite volume V in Eq. (1.23) is a complex endeavor given the large number of bodies involved in the exchange interaction, and so some approximation need to be made. The simplest of these approximations is the molecular mean-field approximation. The approximation proceeds in two steps:

1) A single spin is "tagged", and its dynamic is treated exactly, while the surrounding spins are replaced by their expectation value $\langle \mathbf{S} \rangle$.

2) The self-consistency condition is imposed, such that every spin in the system is subjected to the same mean field from the other spins. Thus, the result obtain for a single spin is the same obtained for all the other spins in the system.

In the next sections we derive, using the mean-field approximation, the molecular field generated by the exchange interaction for both a ferromagnetic exchange and an antiferromagnetic exchange.

A Ferromagnetic molecular field

We first focus on a ferromagnetic material, where $J_{ij} > 0$. The energy of the system can then be expressed as:

$$E_i = -\frac{1}{2}\sum_{ij} J_{ij}\mathbf{S}_i \cdot \langle \mathbf{S}_j \rangle - g\mu_b \mathbf{S}_i \cdot \mathbf{H} = -\mathbf{S}_i \cdot \mathbf{H}_i^{MFA} \ , \tag{1.24}$$

where the mean field approximation of the field $\mathbf{H}_i^{MFA}$ is given by

$$\mathbf{H}_i^{MFA} = \mathbf{H} + \frac{1}{g\mu_B}\sum_j J_{ij} \langle \mathbf{S}_j \rangle \approx \mathbf{H} + \frac{xJ}{g\mu_B}\langle \mathbf{S}_j \rangle \ , \tag{1.25}$$

where the last approximation in Eq.(1.25) is obtained by assuming that J_{ij} is non zero only for the x nearest neighbors of the spin, and where J is the average exchange integral between the neighbors. Using Eq. (1.25), it is possible to reduce the problem of spin interacting with each other to the case discussed in the previous section, i.e. the one of an isolated spin interacting with an applied field. Thus, the expected value of the z-component of S_i is given by:

$$\langle S_{z,i} \rangle = SB_S\left(\frac{\mu_0 H_i}{k_b T}\right) . \tag{1.26}$$

Applying the self-consistency condition, there is no difference between the spin i and the other spins appearing in the summation in Eq. (1.25). Thus, we can rewrite explicitly:

$$\langle S_z \rangle = SB_S\left(\frac{\mu_0}{k_b T}\left[H + H_E\right]\right) , \tag{1.27}$$

where the molecular field H_E for a ferromagnet is given by:

$$H_E = \frac{xJ}{g\mu_B}\langle \mathbf{S} \rangle = \frac{J_0 S^2}{\mu_0}\mathbf{m} \ . \tag{1.28}$$

where the exchange integral $J_0 = xJ$ and the magnetic moment μ_0 is given by Eq.(1.13). Equation (1.27) shows that a ferromagnet has a finite magnetization even in the absence of an

external field due to the presence of the molecular field H_E induced by the spin interaction. At high temperature, the magnetization tends to zero, and at low temperature a spontaneous magnetization arises. If we consider the transition between these two states, it is possible to obtain a relationship between the exchange integral J_0 as a function of the Curie temperature T_C, by expanding Eq. (1.27) around the transition point. For a finite spin S, the relationship between T_C and J_0 is given by

$$k_b T_C = S(S+1) J_0 / 3 , \tag{1.29}$$

and for the classical limit (i.e. $S \to \infty$):

$$k_b T_C = J_0 / 3 \ . \tag{1.30}$$

B Antiferromagnetic molecular field

In ferrimagnetic and antiferromagnetic materials, the exchange integral between nearest neighbor is negative (i.e. $J_0 < 0$) and tends to align neighboring spin antiparallel to each other. Using Neel approximation, it is possible to split the lattice into two sublattices A and B (Figure 1.3-2). Each sublattice is treated as in the ferromagnetic case with $J_{A/B} > 0$, and the two sublattices are coupled locally by the antiferromagnetic exchange coefficient $J_{AB} < 0$, with $|J_{AB}| > J_{A/B}$.

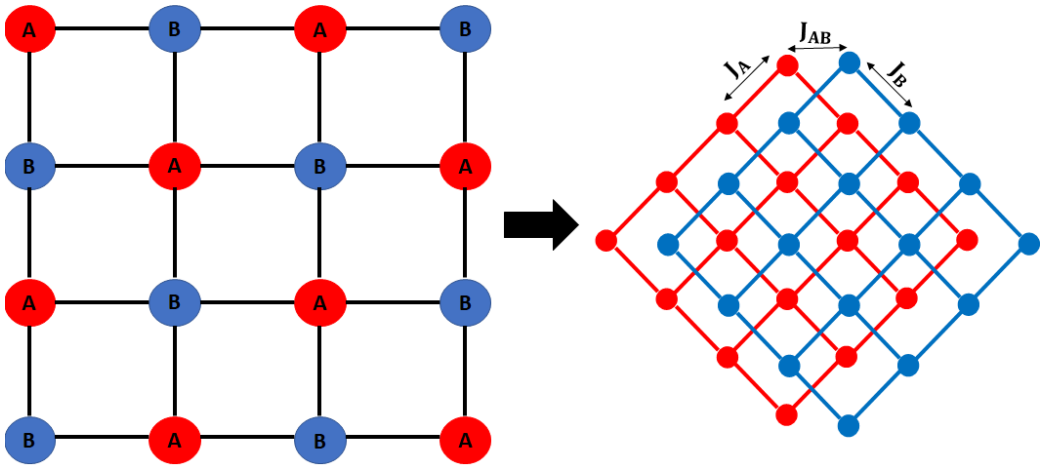

Figure 1-2: Ferrimagnetic lattice composed by two atoms A and B (on the left). The system is approximated by two sublattices (on the right) each one composed only by either atoms A (red) or the atom B (blue). Each sublattice is treated as a ferromagnetic material with $J_{A/B} > 0$, the two lattices are coupled locally with an exchange coefficient $J_{AB} < 0$.

It is possible to define an effective field for the two sublattices as in the ferromagnetic case:

$$H_A = H + \frac{J_{0,A}}{g_A \mu_B}\langle S_A \rangle + \frac{J_{0,AB}}{g_A \mu_B}\langle S_B \rangle \ , \tag{1.31}$$

$$H_B = H + \frac{J_{0,B}}{g_B \mu_B}\langle S_B \rangle + \frac{J_{0,AB}}{g_B \mu_B}\langle S_A \rangle \ , \tag{1.32}$$

where $J_{0,A/B} = x_{A/B} J_{A/B}$, $J_{0,AB} = x_{AB} J_{AB}$, x_A and x_B are the numbers of nearest neighbors in the sublattice A and B, respectively, and x_{AB} is the number or nearest neighbors in the original lattice.

The consistency condition is given by solving for the transcendental equations:

$$\langle S_{A,z} \rangle \approx S_A B_S\left(\frac{\mu_{0,A}}{k_b T}\left[H + \frac{J_{0,A} S_A}{\mu_{0,A}}\langle S_{A,z} \rangle + \frac{J_{0,AB} S_A}{\mu_{0,A}}\langle S_{B,z} \rangle\right]\right), \tag{1.33}$$

$$\langle S_{B,z} \rangle \approx S_B B_S\left(\frac{\mu_{0,B}}{k_b T}\left[H + \frac{J_{0,B} S_B}{\mu_{0,B}}\langle S_{B,z} \rangle + \frac{J_{0,AB} S_B}{\mu_{0,B}}\langle S_{A,z} \rangle\right]\right), \tag{1.34}$$

where $\mu_{0,A/B} = g_{A/B}\mu_B S_{A/B}$ is the magnetic moment of the atoms in the sublattice A/B and the two g-factors g_A and g_B are identical if $\langle S_A \rangle = -\langle S_B \rangle$ at the equilibrium. The molecular field for the antiferromagnetic interaction is given by:

$$\mathbf{H}_{E,A} = \frac{J_{0,A} S_A^2}{\mu_{0,A}} \mathbf{m}_A + \frac{J_{0,AB} S_A S_B}{\mu_{0,A}} \mathbf{m}_B \ , \tag{1.35}$$

$$\mathbf{H}_{E,B} = \frac{J_{0,B} S_B^2}{\mu_{0,B}} \mathbf{m}_B + \frac{J_{0,AB} S_A S_B}{\mu_{0,B}} \mathbf{m}_A . \tag{1.36}$$

In the general case, when $|\langle S_A \rangle| \neq |\langle S_B \rangle|$ it is possible to define a Curie temperature for the two sublattices, solving the transcendental Eq.(1.33)-(1.34) close to the transition point:

$$\langle S_A \rangle = \frac{S_A(S_A+1)}{3k_b T} \left(g_A \mu_B H + \tilde{J}_{0,A} \langle S_A \rangle \right) , \tag{1.37}$$

$$\langle S_B \rangle = \frac{S_B(S_B+1)}{3k_b T} \left(g_B \mu_B H + \tilde{J}_{0,B} \langle S_B \rangle \right) , \tag{1.38}$$

where the effective sublattice exchange integrals for the two sublattices are given by:

$$\tilde{J}_{0,A} = x_A J_A + x_{AB} J_{AB} \frac{S_B}{S_A} \frac{\mathbf{m}_A \cdot \mathbf{m}_B}{m_A^2} \ , \tag{1.39}$$

$$\tilde{J}_{0,B} = x_B J_B + x_{AB} J_{AB} \frac{S_B}{S_A} \frac{\mathbf{m}_A \cdot \mathbf{m}_B}{m_A^2} \ . \tag{1.40}$$

In the absence of an applied field, the relationship between the Curie temperature and the effective sublattice exchange is given by:

$$k_b T_{C_A} = S_A (S_A + 1) \tilde{J}_{0,A} / 3 \ , \tag{1.41}$$

$$k_b T_{C_B} = S_B (S_B + 1) \tilde{J}_{0,B} / 3 . \tag{1.42}$$

CHAPTER 2 - MICROMAGNETIC MODEL OF MAGNETISM

If the previous chapter, we focused on the interactions between the magnetic moment and the field on an atomistic level. By neglecting the atomistic nature of the matter, it is possible to approximate the magnetization and the material properties of the material as continuous variable. Such classical approach was first introduced by W.F. Brown [2] to study the dynamics of the domain walls, and since then it has been routinely used to describe and simulate the magnetic phenomena on the mesoscale.

Part of the classical approach is to replace the spin with a vector and to replace the quantum-mechanical interactions in the limit of a continuous material. In this chapter, we first introduce the classical energy for a ferromagnetic material with biaxial anisotropy. The effective field is then derived by minimizing the free energy of the system. Finally, we introduce the semi-classical dynamic model, described by Landau-Lifshitz-Bloch model for ferromagnetic and ferrimagnetic. This model forms the base of the study of the magnetization dynamics that is used in the rest of the dissertation.

2.1 MICROMAGNETIC FREE ENERGY

We consider the classical ferromagnetic model with the biaxial anisotropic exchange interactions described by the Hamiltonian:

$$\mathcal{H} = -\mu_0 \sum_i \mathbf{H} \cdot \mathbf{S}_i - \frac{1}{2} \sum_{ij} J_{ij} \left(\eta_x S_{x,i} S_{x,j} + \eta_y S_{y,i} S_{y,j} + S_{z,i} S_{z,j} \right) , \tag{2.1}$$

where $\eta_x \le \eta_y \le 1$ are the anisotropic coefficients. By introducing the anisotropy coefficients $\eta'_{x,y} = 1 - \eta_{x,y}$, and only considering the exchange between nearest neighbors it is possible to rewrite the Hamiltonian as:

$$\mathcal{H} = -\mu_0 \sum_i \mathbf{H} \cdot \mathbf{S}_i - \frac{J}{2} \sum_{n.n} \left(\mathbf{S}_i \cdot \mathbf{S}_j \right) + \frac{J}{2} \sum_{n.n} \left(\eta'_x S_{x,i} S_{x,j} + \eta'_y S_{x,i} S_{x,j} \right) , \tag{2.2}$$

where the second term in Eq. (2.2) is the exchange interactions and the third term represents the anisotropy contribution. If we introduce the anisotropic field coefficients $H_{K,x} = JS^2 \eta'_x / 2\mu_0$ and $H_{K,y} = JS^2 \eta'_y / 2\mu_0$, we can write the mean field approximation of the field for a ferromagnetic material as:

$$\mathbf{H}_{local}^{MFA} = \mathbf{H} + \frac{J_0 S^2}{\mu_0} \mathbf{m} - \left(H_{K,x} \mathbf{m}_x + H_{K,y} \mathbf{m}_y \right), \tag{2.3}$$

or in the case of a ferrimagnetic material, we can write the mean field approximation of the field for the two sublattices as:

$$\mathbf{H}_{A,local}^{MFA} = \mathbf{H} + \frac{J_{0,A} S_A^2}{\mu_{0,A}} \mathbf{m}_A + \frac{J_{0,AB} S_A S_B}{\mu_{0,A}} \mathbf{m}_B - \left(H_{K_A,x} \mathbf{m}_{A,x} + H_{K_A,y} \mathbf{m}_{A,y} \right), \tag{2.4}$$

$$\mathbf{H}_{B,local}^{MFA} \approx \mathbf{H} + \frac{J_{0,B} S_B^2}{\mu_{0,B}} \mathbf{m}_B + \frac{J_{0,AB} S_A S_B}{\mu_{0,B}} \mathbf{m}_A - \left(H_{K_B,x} \mathbf{m}_{B,x} + H_{K_B,y} \mathbf{m}_{B,y} \right) \tag{2.5}$$

The free energy of the system can then be expressed for a continuous ferromagnetic system of volume V as:

$$\mathcal{E}_{H_{local}^{MFA}} = -\mu_0 \int \left[\mathbf{m} \cdot \mathbf{H} - \frac{J_0 S^2}{2} m^2 - \frac{1}{2} \left(H_{K,x} m_x^2 + H_{K,x} m_y^2 \right) \right] dV , \tag{2.6}$$

or in the case of a ferrimagnetic material, the free energy of the system is given for each sublattice by:

$$\mathcal{E}_{H_{B,local}^{MFA}} = -\mu_{0A}\int\left[\mathbf{m}\cdot\mathbf{H} + \frac{J_{0,A}S_A{}^2}{2}\left(m_A^2 + \frac{J_{0,AB}S_B}{J_{0,A}S_A}\mathbf{m}_A\cdot\mathbf{m}_B\right) - \frac{\left(H_{K_A,x}m_{A,x}^2 + H_{K_A,y}m_{A,y}^2\right)}{2}\right]dV \ , \qquad (2.7)$$

$$\mathcal{E}_{H_{B,local}^{MFA}} = -\mu_{0B}\int\left[\mathbf{m}\cdot\mathbf{H} + \frac{J_{0,B}S_B{}^2}{2}\left(m_B^2 + \frac{J_{0,AB}S_A}{J_{0,B}S_B}\mathbf{m}_A\cdot\mathbf{m}_B\right) - \frac{\left(H_{K_B,x}m_{B,x}^2 + H_{K_B,y}m_{B,y}^2\right)}{2}\right]dV \ . \qquad (2.8)$$

The terms $\mathcal{E}_{H_{local}^{MFA}}$ given in Eq.(2.6)-(2.8) contains all the local components of the energy for a ferromagnetic and ferrimagnetic continuous media. Besides the terms discussed so far, there are other two terms that play a role in determining the overall magnetization in a continuous material: the magnetostatic energy (long range) and the classical exchange (short range). In the next subsection we discuss these long- and short-range interactions.

A Magnetostatic energy

The magnetostatic energy is originated from the classical interaction among the dipoles. For a continuous media, this interaction is described by the Maxwell equations. In the absence of a current, the curl of magnetic field is zero:

$$\nabla\times\mathbf{H} = 0 \ . \qquad (2.9)$$

The vector $\mathbf{H}$ can then be expressed by a scalar potential U, such that $\mathbf{H} = -\nabla U$. Using the potential relationship, it is possible to express the Gaussian's law for magnetism in CGS units as:

$$\nabla\cdot\mathbf{B} = \mu_o\nabla\cdot\left(\mathbf{H}+\mathbf{M}\right) = 0 \quad \Rightarrow \quad \nabla^2 U = \begin{cases}\nabla\cdot\mathbf{M} & \forall\mathbf{r}\in\Omega \\ 0 & \forall\mathbf{r}\notin\Omega\end{cases} \ . \qquad (2.10)$$

where Ω is the region occupied by the magnetic body. Applying the continuity condition at the interface of the magnetic body, we find:

$$\frac{\partial U^+}{\partial n} - \frac{\partial U^-}{\partial n} = \left(\mathbf{H}\cdot\mathbf{n} + \mathbf{M}\cdot\mathbf{n} - \mathbf{H}\cdot\mathbf{n}\right) = \mathbf{M}\cdot\mathbf{n} \ , \qquad (2.11)$$

where U^+ is the potential at the interface inside Ω, U^- is the potential outside Ω, and $\mathbf{n}$ is the unit normal to the close surface $\partial\Omega$. The potential is assumed to be bounded at infinity, which means $|rU|$ and $|r^2\nabla U|$ are finite for $r \to \infty$. The condition of the bounded potential means that at long distances, the magnetic field can be considered as the one originating from a point dipole. The magnetostatic field $\mathbf{H}_{MS}(\mathbf{r})$ can then obtained by solving for the potential and the magnetostatic energy is given by:

$$\mathcal{E}_{MS} = \frac{1}{2}\int \mathbf{M}(\mathbf{r}) \cdot \mathbf{H}_{MS}(\mathbf{r}) d\mathbf{r}^3 \ . \tag{2.12}$$

The magnetostatic energy, together with the exchange energy, is responsible for the existence of magnetic domains. The system tends to minimize its energy. If we consider a discrete series of macrospins, each with a uniform magnetization $\mathbf{M}_i$, the magnetostatic energy can be expressed as:

$$\mathcal{E}_{MS} = \frac{1}{2}\sum_{i=1}^{N}\sum_{\substack{j=1 \\ i\neq j}}^{N} M_i \cdot H_j(\mathbf{r}_i), \tag{2.13}$$

where $\mathbf{H}_j(\mathbf{r}_i)$ is the field acting on M_i and generated by M_j. Equation (2.13) shows that the energy of the system is reduced when the magnetic moments are antiparallel. However, the exchange interaction for ferromagnetic material minimize the energy when neighbor spins are parallel to each other's. The system then only breaks into domains if the total energy of the system when two domains are presents is lower than the energy required to have a single domain.

B Exchange Energy

While the magnetostatic energy is a long range effect that is affected by the interactions of several hundred unit cells, the exchange interaction J_{ij} is a strong interaction that only affects the

nearest neighbors or the next-nearest neighbors. The system minimizes its energy by creating a small angle between two nearby spins, instead of creating an abrupt transition. If we consider the exchange integral J to be non-zero only between the nearest neighbors, it is possible to rewrite the exchange energy in Eq. (1.23) as:

$$E_{ex} = -2JS^2 \sum_{n.n} \cos(\theta_{ij}), \tag{2.14}$$

where $\cos(\theta_{ij})$ is the angle between the spin $\mathbf{S}_i$ and the spin $\mathbf{S}_j$. Below T_C, the exchange between spins is strong enough to keep the neighbor spins almost parallel. Thus, it is reasonable to assume for the angle between two neighbor spin to be small (i.e. $\theta_{ij} \sim 0$). We can then rewrite the exchange energy as:

$$E_{ex} \approx -2JS^2 \sum_{n.n.} \left(1 - \frac{\theta_{ij}^2}{2}\right) = \text{const} + JS^2 \sum_{n.n} \theta_{ij}^2 \approx \text{const} + JS^2 \sum_{n.n} \left|\mathbf{m}_i - \mathbf{m}_j\right|^2 \ . \tag{2.15}$$

Considering the condition of continuity of the magnetization inside the magnetic domain, it is possible to rewrite the difference between the magnetization of neighbor spin as a continuous function:

$$\left|\mathbf{m}_i - \mathbf{m}_j\right| = \Delta \mathbf{r}_{ij} \nabla \mathbf{m} \ , \tag{2.16}$$

where Δr_{ij} is the distance between the lattice points i and j. Substituting Eq. (2.16) in to Eq.(2.15) and substituting the sum over all the sites i with a continuous integral over the magnetic body, it is possible to write the exchange energy as

$$\mathcal{E}_{ex} = \int A \left[\left(\nabla m_x\right)^2 + \left(\nabla m_y\right)^2 + \left(\nabla m_z\right)^2 \right] dV \ , \tag{2.17}$$

where the exchange constant A is given by:

$$A = \frac{nJS^2}{6} a^2 \ , \tag{2.18}$$

where a is the lattice spacing and n is a number dependent on the type of lattice.

2.2 MICROMAGNETIC EFFECTIVE FIELD

Let us consider a ferromagnetic body of an arbitrary shape. The total energy of the system $\mathcal{E}_M$ in the mean-field approximation is given by:

$$\mathcal{E}_M = \mathcal{E}_{H^{MFA}} + \mathcal{E}_{ex} + \mathcal{E}_{MS} = -\int \left[\mathbf{M} \cdot \mathbf{H}_{local}^{MFA} + A\left(\nabla^2 \mathbf{m}\right) + \mathbf{M}(r) \cdot \mathbf{H}_{MS}(\mathbf{r}) \right] dV \ . \tag{2.19}$$

This expression allows us to determine the energy of the system, if the value of the magnetization $\mathbf{m}(\mathbf{r})$ is known. The problem here is to determine the magnetization $\mathbf{m}(\mathbf{r})$ that minimizes the energy of the system under the constraint $B(\mu_0 \beta H) = m_0$. The easiest way to do so is to introduce a new function $\mathcal{L}$ such that:

$$\mathcal{L}(\mathbf{m}, \lambda) = \mathcal{E}_M + \int \lambda \left((B_S(\mu_0 \beta H_{eff}))^2 - m_0^2 \right) dV \ , \tag{2.20}$$

where λ is the Lagrange multiplier. By setting $\nabla \mathcal{L}(\mathbf{m}, \lambda) = 0$, it is possible to obtain the value of the magnetization at the equilibrium:

$$\begin{aligned} 0 = \frac{\delta \mathcal{L}}{\delta \mathbf{M}} = -\int \left[\mathbf{H} + \frac{J_0 S^2}{\mu_0} \mathbf{m} - H_k \left(\mathbf{m}_x + \mathbf{m}_y \right) + \frac{2A}{\mu_0} \nabla^2 \mathbf{m} + \mathbf{H}_{ms} - 2\lambda \mathbf{m} \right] dV \\ + \oint 2A \left(\frac{\partial \mathbf{m}}{\partial \mathbf{n}} \right) dS \end{aligned} \ , \tag{2.21}$$

$$B_S\left(\mu_0 \beta H_{eff}\right) = m_0 \ , \tag{2.22}$$

where for simplicity we chose $H_K = H_{K,x} = H_{K,y}$. The total mean field approximation of the field acting on the material is given by:

$$\mathbf{H}^{MFA} = \mathbf{H}_E + \mathbf{H}_{eff} \ , \tag{2.23}$$

$$\mathbf{H}_E = \frac{J_0 S^2}{\mu_0} \mathbf{m}, \qquad \mathbf{H}_{eff} = \mathbf{H} + \mathbf{H}_{ex} + \mathbf{H}_{ms} + \mathbf{H}_{ani} \ , \tag{2.24}$$

where the anisotropy field $\mathbf{H}_{ani}$ and the exchange field $\mathbf{H}_{ex}$ are given by:

$$\mathbf{H}_{ex} = \frac{2A}{M_S}\nabla^2\mathbf{m} \ , \tag{2.25}$$

$$\mathbf{H}_{ani} = (H_{K,x}\mathbf{m}_x + H_{K,y}\mathbf{m}_y) \ . \tag{2.26}$$

The only condition for the infinitesimal variation in magnetization $\delta\mathbf{m}$ that satisfies the constrains given by Eq. (2.22), is a rotation $\delta\vec{\theta}$ of the vector field $\mathbf{m}$, that is

$$\delta\mathbf{m} = \mathbf{m}\times\delta\vec{\theta} \ . \tag{2.27}$$

The equilibrium condition given in Eq. (2.21) is valid for any arbitrary elementary rotation $\delta\mathbf{m}$. By multiplying the integral over the surface by $\delta\mathbf{m}$, it is possible to obtain the boundary condition on the surface of the magnetic domain $\partial\Omega$:

$$\mathbf{m}\times\frac{\partial\mathbf{m}}{\partial\mathbf{n}} = 0 \quad \rightarrow \quad \left.\frac{\partial\mathbf{m}}{\partial\mathbf{n}}\right|_{\partial\Omega} = 0 \ . \tag{2.28}$$

For ferrimagnetic materials, the formulation of the applied field is slightly more complicated. The molecular field in each sublattice is given by:

$$\mathbf{H}_{E,v} = \mathbf{H}_{E,v}^{\parallel} + \mathbf{H}_{E,v}^{\perp}, \tag{2.29}$$

$$\mathbf{H}_{E,v}^{\parallel} = \frac{\tilde{J}_{0,v}}{\mu_{0,v}}\mathbf{m}_v, \qquad \mathbf{H}_{E,v}^{\perp} = \frac{J_{0,vk}}{\mu_{0,v}}\mathbf{\Pi}_k \ , \tag{2.30}$$

where $v,k = A,B$, and

$$\mathbf{\Pi}_v = -\frac{\left[\mathbf{m}_k\times\left(\mathbf{m}_k\times\mathbf{m}_v\right)\right]}{m_k^2} \ . \tag{2.31}$$

The instantaneous equilibrium magnetization for the ferrimagnetic case is given by the projection of the field on the direction of the magnetization such that:

$$m_0(\mathbf{H},T) = B_S(\xi_{0,v}), \qquad \xi_{0,v} = \mu_0\beta\left(H_{E,v}^{\parallel} + \frac{\mathbf{m}\cdot\mathbf{H}_{eff,v}^{'}}{m}\right), \tag{2.32}$$

where $\mathbf{H}'_{eff,v} = \mathbf{H} + \mathbf{H}_{ex,v} + \mathbf{H}_{ms,v} + \mathbf{H}_{ani,v}$. The effective field acting on the magnetization for each sublattice is given by:

$$\mathbf{H}_{eff,v} = \mathbf{H}'_{eff,v} + \mathbf{H}^{\perp}_{E,v} \ . \tag{2.33}$$

2.3 LANDAU-LIFSHITZ-BLOCH EQUATION

A magnetic material subjected to an external field is subjected to a precessional motion described by the Landau-Lifshitz equation [3]:

$$\frac{d\mathbf{m}}{dt} = \gamma \mathbf{m} \times \mathbf{H} \tag{2.34}$$

where $\gamma = 1.760859 \times 10^{11}$ $\mathrm{s^{-1}T^{-1}}$ is the gyromagnetic ratio. For a given applied field, the frequency of the precession of the magnetization is given by the Larmor frequency:

$$\omega_L = \gamma H \ . \tag{2.35}$$

The process described by Eq. (2.32) is a Hamiltonian conservative process. Due to physical defects and the interaction with the environment, the magnetic system is subjected to dissipative forces. This effect is modelled with non-linear spin relaxation that aligns the magnetization in the direction of the field [4]:

$$\frac{d\mathbf{m}}{dt} = -\gamma \mathbf{m} \times \mathbf{H}_{eff} - \frac{\gamma \alpha_{\perp}}{m^2}\left[\mathbf{m} \times \left(\mathbf{m} \times \mathbf{H}_{eff}\right)\right] , \tag{2.36}$$

where $\alpha_{\perp}$ is the transverse damping coefficient and is a function of the temperature T:

$$\alpha_{\perp} = \lambda\left(1 - \frac{1}{\beta J_0}\right) , \tag{2.37}$$

where $\lambda \leq 1$ is the atomistic damping coefficient.

At elevated temperature, the length of the magnetization is a function of both the field and the instantaneous temperature. To model the longitudinal dynamics of the magnetization, we

define the instantaneous equilibrium magnetization, as function of the reduced field $\boldsymbol{\xi}_0 = \mu_0 \beta \mathbf{H}^{MFA}$:

$$\mathbf{m}_0(\boldsymbol{\xi}_0) = B_S(\xi_0)\frac{\boldsymbol{\xi}_0}{\xi_0} \ . \tag{2.38}$$

Assuming only small deviations from the instantaneous equilibrium (i.e. $\mathbf{m} \approx \mathbf{m}_0$), we can write the equation of motion for the magnetization as [5]:

$$\frac{d\mathbf{m}}{dt} = -\gamma \mathbf{m} \times \mathbf{H}_{eff} - \gamma \alpha_{\|} \frac{\left(1 - \frac{\mathbf{m} \cdot \mathbf{m}_0}{\mathbf{m}^2}\right)}{\mu_0 \beta B_S'(\xi_0)} \mathbf{m} - \frac{\gamma \alpha_{\perp}}{m^2}\left[\mathbf{m} \times \left(\mathbf{m} \times \mathbf{H}_{eff}\right)\right] \ , \tag{2.39}$$

where $B_S'(\xi_0)$ is the derivate of the Brillouin function with respect to ξ_0, and $\alpha_{\|}$ is the longitudinal damping coefficient and it is a function of the temperature given by:

$$\alpha_{\|} = \frac{2\lambda}{\beta J_0} \ . \tag{2.40}$$

The equation given by Eq. (2.39) is known as the Landau-Lifshitz-Bloch equation for ferromagnetic materials. If we use the magnetization vector as our frame of reference, we can understand the contribution of the precession, transverse, and longitudinal relaxation as the variation in time of the three orthogonal components ϕ , θ , and r in spherical coordinates (Figure 2-1a). In ferromagnetic materials for temperature below the Curie temperature, the molecular field is much larger than the effective field (i.e. $\left|H_E\right| \gg \left|H_{eff}\right|$). Thus, the only way to reverse the magnetization is by precession (Figure 2-1b).

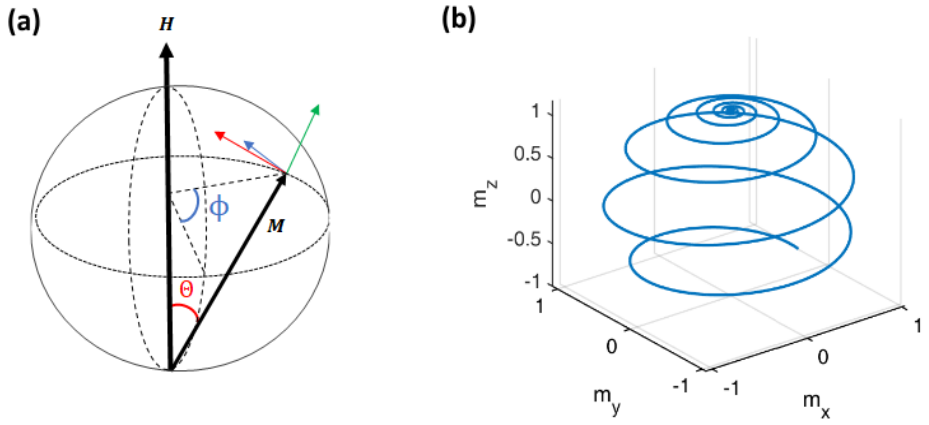

Figure 2-1: Magnetization dynamics of single particle immersed in an applied field $H = H_z$. (a) Shows the contribution of the precession (blue arrow), the transverse damping (red arrow), and the longitudinal relaxation (green line) on the instantaneous magnetization vector $\mathbf{m}$. (b) Shows the evolution in time of such system.

For ferrimagnetic material, the equation of motion is given by two equations of motion for ferromagnets, one for each sublattice, coupled by the intra-lattice exchange given by Eq. (1.35)-(1.36):

$$\frac{d\mathbf{m}_v}{dt} = -\gamma \mathbf{m}_v \times \mathbf{H}_{eff,v} - \gamma \alpha_{\|,v} \frac{\left(1 - \frac{\mathbf{m}_v \cdot \mathbf{m}_{0,v}}{m_v^2}\right)}{\mu_{0,v} \beta B_S'(\xi_{0,v})} \mathbf{m} - \frac{\gamma \alpha_{\perp,v}}{m_v^2} \left[\mathbf{m}_v \times \left(\mathbf{m}_v \times \mathbf{H}_{eff,v}\right)\right], \tag{2.41}$$

where $\alpha_{\|,v} = 2\lambda_v / \beta \tilde{J}_{0,v}$, $\alpha_{\perp,v} = 2\lambda_v \left(1 - 1/\beta \tilde{J}_{0,v}\right)$ and $\tilde{J}_{0,v}$ for the two sublattices is given by Eq. (1.39)-(1.40). The reduced field $\xi_{0,v}$ for the ferromagnetic sublattice is given by Eq. (2.32), while the effective field $\mathbf{H}_{eff,v}$ is given by Eq. (2.33).

2.4 STOCHASTIC LANDAU-LIFSHITZ-BLOCH EQUATION

To describe the magnetization dynamics at elevated temperature it is necessary to consider the fluctuations generated by the interactions between the magnetization and the thermal bath. Brown suggested to introduce these fluctuations as formal random fields whose properties are defined by

the equilibrium solution of the corresponding Fokker-Planck (FP) equation. Chapter 7 covers the derivation of a new formulation of the stochastic field based on the rigorous solution of the FP equation. Here, we introduce two forms of the stochastic LLB equation commonly used in micromagnetics. In both formulations, the random fields are described by a stationary white Gaussian noise with zero mean and:

$$\left\langle \zeta_i^{\mu}(t) \right\rangle = 0 \qquad \left\langle \zeta_i^{\mu}(0)\zeta_j^{\nu}(t) \right\rangle = 2D_{\mu}\delta_{ij}\delta_{\mu\nu}\delta(t) \ , \tag{2.42}$$

where δ_{ij} is the Kronecker delta, $\delta(t)$ is the Dirac delta function, $\mu,\nu = \|,\perp$ define the longitudinal and transverse components of the noise, and $i,j = x,y,z$ defines the cartesian coordinates of the field. The diffusion coefficients D_{μ} are obtained by solving the FP equation.

The first model, defined as LLB-I, was introduced by Garanin [6]. In this formulation, the thermal fluctuations are introduced as two multiplicative noise fields $\boldsymbol{\zeta}_{\perp}$ and $\boldsymbol{\zeta}_{\|}$ acting on the transverse and longitudinal damping component, respectively:

$$\left.\frac{d\mathbf{m}}{dt}\right|_{\text{LLB-I}} = -\gamma\mathbf{m}\times\mathbf{H}_{eff} - \gamma\alpha_{\|}\left[\frac{\left(1-\dfrac{\mathbf{m}\mathbf{m}_0}{\mathbf{m}^2}\right)}{\mu_0\beta B_S'(\xi_0)} - \frac{\mathbf{m}\boldsymbol{\zeta}_{\|}}{m^2}\right]\mathbf{m} - \frac{\gamma\alpha_{\perp}}{m^2}\left[\mathbf{m}\times\left(\mathbf{m}\times\left(\mathbf{H}_{eff}+\boldsymbol{\zeta}_{\perp}\right)\right)\right] \ , \tag{2.43}$$

where the diffusion coefficients $D_{\mu,\text{LLB-I}}$ with $\mu = \|,\perp$ are given by:

$$D_{\mu,\text{LLB-I}} = \frac{k_b T}{\gamma M_S V \alpha_{\mu}} \ . \tag{2.44}$$

The second model, defined as LLB-II, was introduced by Evans in 2012 [7]. In this formulation, the field acting on the transverse damping component is introduced as a multiplicative noise field, $\boldsymbol{\zeta}_{\perp}$, while the second field is introduced as an additive noise field , $\boldsymbol{\zeta}_{\|}$:

$$\frac{d\mathbf{m}}{dt} = -\gamma\mathbf{m}\times\mathbf{H}_{eff} - \gamma\alpha_{\|}\frac{\left(1-\dfrac{\mathbf{m}\mathbf{m}_0}{\mathbf{m}^2}\right)}{\mu_0\beta B_S'(\xi_0)}\mathbf{m} - \frac{\gamma\alpha_{\perp}}{m^2}\left[\mathbf{m}\times\left(\mathbf{m}\times\left(\mathbf{H}_{eff}+\boldsymbol{\zeta}_{\perp}\right)\right)\right] + \boldsymbol{\zeta}_{\|} \ , \tag{2.45}$$

where the diffusion coefficients are given by:

$$D_{\perp,\text{LLB-II}} = \frac{k_b T\left(\alpha_\perp - \alpha_\parallel\right)}{\gamma M_S V \alpha_\perp^2}, \qquad D_{\parallel,\text{LLB-II}} = \frac{\gamma k_b T \alpha_\parallel}{M_S V} \ . \tag{2.46}$$

The two formulations only noticeably differ for temperature close to T_C, and both formulations displace the value of the equilibrium magnetization $m_e = B_S(\beta J_0 m_e)$ in the absence of an external magnetic field. In the rest of the dissertation, we consider the LLB-I formulation as the stochastic model used in the simulation if not explicitly stated.

CHAPTER 3 - MICROMAGNETIC SIMULATOR FOR COMPLEX GRANULAR SYSTEMS BASED ON VORONOI TESSELLATION

This chapter presents a micromagnetic Voronoi code that was developed with the primary aim of simulating granular systems. The code relies on Voronoi tessellation for the discretized representation of the granular structure. Each grain is represented as a single Voronoi cell or a vertical stack of several Voronoi cells. Such a representation produces the least number of unknowns needed for modeling single domain grains and results in a non-stiff system in the case of uncoupled or weakly coupled grains.

A GPU-based NUFFT algorithm was implemented by my colleague Marko V. Lubarda to reduce the order of operations in the calculation of the magnetostatics field from $O(N^2)$ to $O(N\log(N))$, where N is the number of grains in our model.

The generality of the code allows sophisticated modeling of complex multilayered granular structures, and distributions in material and structural properties of the grains and interfaces. Such granular films can be postprocessed to obtain nanowires, BPM, spin valves, read heads, and other structures of arbitrary geometry.

The use of highly efficient methods for computing the exchange fields using a natural neighbor approach, a core contribution of the thesis author, and porting the bulk of computations to GPUs results in orders of magnitude speedups compared to conventional simulation approaches. The resulting simulator is a powerful tool for fast and accurate characterization, design and performance studies of granular nanomagnetic systems of a complexity and size not before amendable to simulation.

The ability to model such structures enables the computationally aided interpretation of experimental results involving both small- and large-scale granular systems and devices.

3.1 GRANULAR SYSTEM MODELING

Granular magnetic films are the basis for a number of current and emerging nanotechnologies including heat assisted magnetic recording (HAMR) [8,9] magnetic random access memories (MRAM) [10] and all optical switching (AOS) [11,12]. The geometry of granular systems and distribution of the material parameters from grain to grain can significantly impact the performance of granular magnetic devices and affect results of experimental studies. It is of interest, therefore, to be able to model and characterize such systems, and investigate their performance over a wide range of parameter space, as well as to explore new designs for overcoming existing technological challenges in related fields.

In previous works, granular systems were either modeled using regular finite difference (FD) approach or finite elements methods (FEM). These methods have both shortcomings and advantages.

The FD methods:

- Easy to implement and lower number of unknowns
- Existing support for FD micromagnetic models like OOMMF [13]
- Cannot account for irregular microstructures
- Produce numerical artifacts due to the periodicity of the discretization

The FEM methods:

- Accurate discretization of complex structure using tetrahedron or hexahedron discretization

- Over discretization of the system
- Difficult to implement
- Numerically stiff due to the size of the mesh

The Voronoi modeling tries to combine the advantages of FD methods with the advantages of the FEM reducing or eliminating all the shortcomings.

In the Voronoi model, each grain is represented by a Voronoi cell, which is treated as a single domain particle. Using a Voronoi discretization to model granular structures allows controlling the distribution of size and shapes commonly observed in a realistic granular structure [14]. To generate the tessellation, we follow an iterative process. We first define an area of work A, larger than the effective area, and the average diameter of the grain D. Dividing the area of the average grain by the working area, we obtain the numbers of seed points. The seed layer is created inside the working area using a user-defined distribution of co-planar seed points.

The coordinates of the seed points are then used to generate the Voronoi tessellation (Figure 1.3-1a) using a simple implementation of the Fortune's algorithm [15]. The Voronoi cells can be separated to model the segregation between grains observed in real granular media (Figure 3.1-1b). The 2D structure is then extruded vertically into one or multiple layers, each on with its own physical parameters, to model single films or multilayer structures (Figure 3.1-1c). Each layer can also be subdivided in sublayers if necessary, to capture the magnetization dynamics inside the grain.

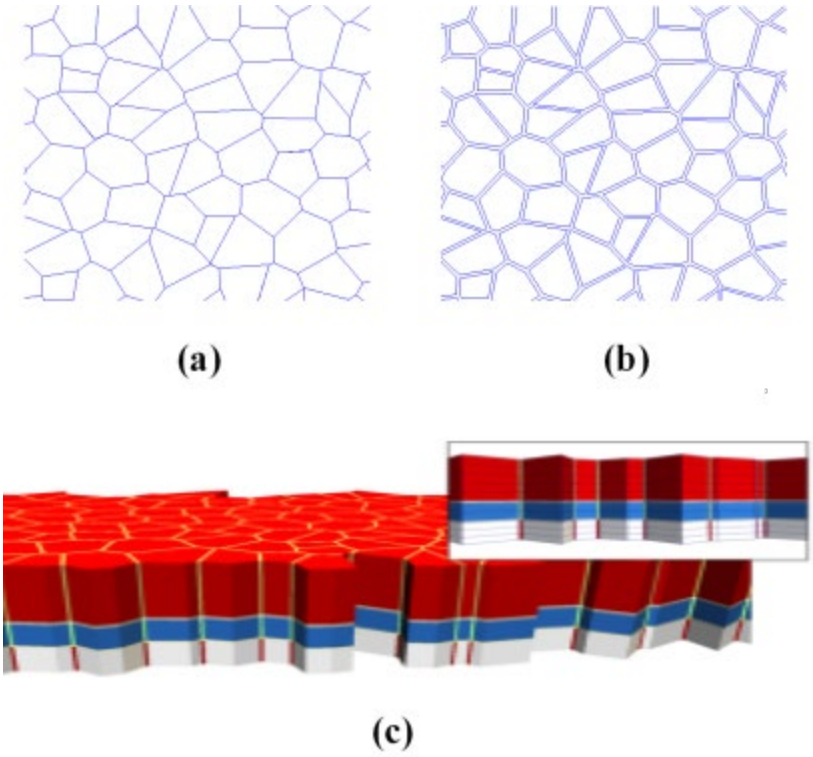

Figure 3-1: (a) Voronoi tessellation based on a user-defined distribution of seed points. (b) Segregation of the cells to simulate granular structure. (c) Extrusion of the 2D cells into a 3D multilayered structure. The image is reproduced with permission from the original paper Ref. [16]

3.2 NUMERICAL IMPLEMENTATION OF THE LLB MODEL

In the granular model, each Voronoi cell of each layer (or sublayer) is modelled using the macrospin approximation (i.e. inside each cell the temperature and the magnetization is homogeneous).

The continuous LLB equation given in Eq. (2.43), is replaced by a system of $3N$ equation, where N is the number of Voronoi cells. Thus, we can write for each cell i the equation of motion for the magnetization as:

$$\frac{d\mathbf{m}_i}{dt} = -\gamma\left(\mathbf{m}_i \times \mathbf{H}_{\mathbf{eff},i}\right) - \gamma\alpha_{\|,i}\left(\frac{1 - B(\tilde{\xi}_{o,i})/m_i}{\mu_{0,i}\beta_i B'(\tilde{\xi}_{o,i})} - \frac{\mathbf{m}_i \cdot \boldsymbol{\zeta}_i^{\|}}{m_i^2}\right)\mathbf{m}_i - \frac{\gamma\alpha_{\perp,i}}{m_i^2}\mathbf{m}_i \times \left(\mathbf{m}_i \times (\mathbf{H}_{\mathbf{eff},i} + \boldsymbol{\zeta}_i^{\perp})\right), \tag{3.1}$$

where $\mathbf{m}_i$ is the normalized magnetization of the cell i, and $\mathbf{H}_{eff,i}$ is the effective field acting on the cell. The reduced field $\tilde{\xi}_0$ is defined by the projection of the field in the direction of the magnetization:

$$\tilde{\xi}_{0,i} = m\beta\tilde{J}_0 \ , \tag{3.2}$$

and the effective exchange integral $\tilde{J}_0$ is given by:

$$\tilde{J}_0 = J_0 + \mu_0 \frac{\mathbf{m} \cdot \mathbf{H}_{eff}}{m^2} \ . \tag{3.3}$$

Since in the stochastic differential equation given in Eq. (3.1) the fluctuations enter the system in a multiplicative way, the solution has to be interpreted and integrated numerically in the context of the Stratonovich calculus [17]. Thus, to integrate the LLB equation we can use the Heun numerical scheme [18] or by a semi-implicit method where the field does not depends on latest time-step. The semi-implicit scheme for the LLB equation is given by:

$$\begin{aligned}\mathbf{X}_i^{(k)} &= \mathbf{m}_i^{(k)} + h\frac{\mathbf{m}_i^{(k)} + \mathbf{X}_i^{(k)}}{2}\left[\times a_i\left(\mathbf{m}^{(k)}\right) + b_i\left(\mathbf{m}^{(k)}\right)\right] \\ &+\sqrt{h}\frac{\mathbf{m}_i^{(k)} + \mathbf{X}_i^{(k)}}{2}\left[\times\boldsymbol{\sigma}_{\perp,i}\left(\mathbf{m}_i^{(k)}, \boldsymbol{\xi}_{\perp,i}^{(k+1)}\right) + \sigma_{\|,i}\left(\mathbf{m}_i^{(k)}, \boldsymbol{\xi}_{\perp,i}^{(k+1)}\right)\right]\end{aligned}, \tag{3.4}$$

$$\begin{aligned}\mathbf{m}_i^{(k+1)} &= \mathbf{m}_i^{(k)} + h\frac{\mathbf{m}_i^{(k)} + \mathbf{m}_i^{(k+1)}}{2}\left[\times a_i\left(\frac{\mathbf{m}^{(k)} + \mathbf{X}^{(k)}}{2}\right) + b_i\left(\frac{\mathbf{m}^{(k)} + \mathbf{X}^{(k)}}{2}\right)\right] \\ &+\sqrt{h}\frac{\mathbf{m}_i^{(k)} + \mathbf{m}_i^{(k+1)}}{2}\left[\times\boldsymbol{\sigma}_{\perp,i}\left(\frac{\mathbf{m}_i^{(k)} + \mathbf{X}_i^{(k)}}{2}, \boldsymbol{\xi}_{\perp,i}^{(k+1)}\right) + \sigma_{\|,i}\left(\frac{\mathbf{m}_i^{(k)} + \mathbf{X}_i^{(k)}}{2}, \boldsymbol{\xi}_{\perp,i}^{(k+1)}\right)\right]\end{aligned}, \tag{3.5}$$

where h is the time-step, $\boldsymbol{\xi}_i^{(k+1)} = \left\{ \xi_{i,x}^{(k+1)}, \xi_{i,y}^{(k+1)}, \xi_{i,z}^{(k+1)} \right\}$ are i.i.d. Gaussian random variables with zero mean and unit variance, and

$$\mathbf{a}_i(\mathbf{m}) = -\gamma \mathbf{H}_{i,eff}\left(\mathbf{m}\right) - \frac{\gamma \alpha_{\perp,i}}{m_i^2} \mathbf{m}_i \times \mathbf{H}_{i,eff}\left(\mathbf{m}\right) , \tag{3.6}$$

$$b_i\left(\mathbf{m}\right) = \gamma \alpha_{\parallel} \frac{1 - B(\xi_{o,i}) / m_i}{\mu_{0,i} \beta_i B'(\xi_{o,i})} , \tag{3.7}$$

$$\boldsymbol{\sigma}_{\perp,i}(\mathbf{m}_i, \boldsymbol{\xi}_i) = \frac{\gamma \alpha_{\perp,i}}{m_i^2} \sqrt{2D_{\perp}}\, \mathbf{m}_i \times \boldsymbol{\zeta}_i , \tag{3.8}$$

$$\sigma_{\parallel,i}(\mathbf{m}_i, \boldsymbol{\xi}_i) = \frac{\gamma \alpha_{\parallel,i}}{m_i^2} \sqrt{2D_{\parallel}}\, \mathbf{m}_i \cdot \boldsymbol{\xi}_i \ . \tag{3.9}$$

The advantage of the semi-implicit method is that reducing the implicitness of the system, it is possible to solve analytically the system by direct inversion of linear 3×3 systems at each time step for each cell [19]. Thus, the semi-implicit scheme has the same computational complexity of the explicit scheme and allows the use of larger time-steps as compared to an explicit scheme. In particular, it allows using timesteps of 0.1ps in most cases, whereas the explicit Heun scheme is limited to a timestep of 0.01-0.05ps.

3.3 COMPUTATION OF NON-LOCAL EFFECTIVE FIELD

The effective field $\mathbf{H}_{eff}$ can be subdivided in 3 different parts, depending of the interaction of the field with the surrounding magnetization:

- Local field: the field computed only depends on the local value of the magnetization $\mathbf{m}_i$ in the i-th cell. The local field is composed of the anisotropy field $\mathbf{H}_{ani}$, the applied field $\mathbf{H}$, the thermal field $\boldsymbol{\zeta}_{\mu}$, and, in the case of ferrimagnets, the intra-lattice exchange $\mathbf{H}_E^{\parallel}$.

- Short range field: the field computed depends not only on the local magnetization $\mathbf{m}_i$, but also on the magnetization of all the cells surrounding cell i. The short-range field is represented by the exchange field $\mathbf{H}_{exc}$.
- Long range field: the field computed depends on the magnetization of all the cells in the media. The long-range field is represented by the magnetostatic field $\mathbf{H}_{ms}$.

The computation of the effective of the local field component is trivial and can be carried over by using directly the equation given in Sec. 2.2. The computation of the short- and long- range fields require a more accurate analysis and their implementation in the code will be discussed in the next sections.

A Exchange Field

The exchange field is a combination of two components: (i) a vertical exchange field, $\mathbf{H}_{ex1,i}$, between different layers, and (ii) a lateral exchange field, $\mathbf{H}_{ex2,i}$, between cells in the same layers. The resulting exchange field is given by:

$$\mathbf{H}_{ex,i} = \mathbf{H}_{ex1,i} + \mathbf{H}_{ex2,i} \tag{3.10}$$

The vertical exchange coupling between grains can be defined through the interfacial exchange energy density associated with the exchange interaction between mutually interfaced Voronoi cells. In this case, the exchange field acting on cell i is given by:

$$\mathbf{H}_{ex,i} = \sum_{j \in \text{interface}} \frac{J_{ij}^{ex} S_{ij}}{M_{S,i} V_i} \left(\mathbf{m}_j - \mathbf{m}_i \right), \tag{3.11}$$

where S_{ij} is the common area between cells i and j. For two cells i and j, J_{ij}^{ex} represents the interlayer exchange energy density:

$$J_{ij}^{ex} = \frac{2A_{ij}^{ex}}{\delta} \ , \tag{3.12}$$

where A_{ij}^{ex} denotes the bulk exchange stiffness of the encompassing grain, and δ is the cell thickness.

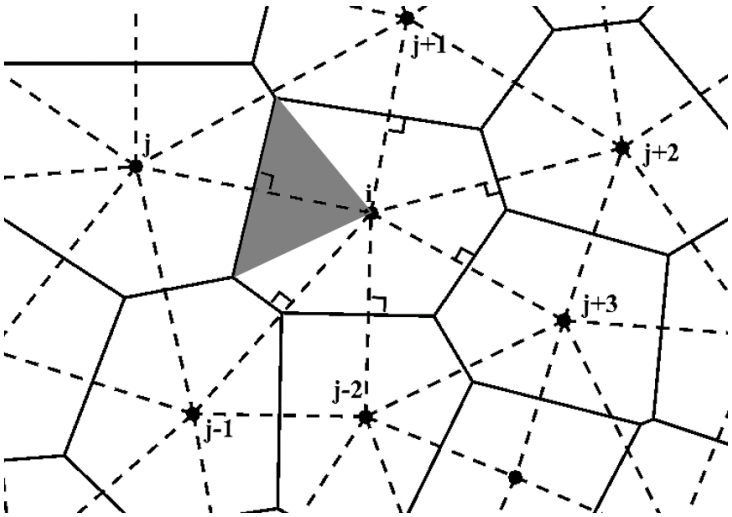

Figure 3-2: The Voronoi tessellation (solid lines) and its dual the Delaunay triangulation (dashed line) for a granular media. The natural neighbors of cell i are shown in the picture as the elements that shares one vertex of the Delaunay triangle with i. The shaded area represents the triangular section of the Voronoi cell i defined by its seed and the shared surface area S_{ij} between i and j .

To compute the lateral exchange, we define the exchange field acting on cell i using the natural neighbors approach with non-Sibsonian interpolation [20,21]. The Delaunay triangulation is constructed as the dual of the Voronoi tessellation. A cell j is said to be a natural neighbor of cell i, if i and j share a vertex in the Delaunay triangulation (Figure 3-2). The shared surface area between two natural neighbors is defined as S_{ij} and h_{ij} is the distance between their seeds. It is important to point out that the seeds and the centers of mass of the Voronoi cells are not generally the same points, unless the Voronoi tessellation is Central Voronoi Tessellation (CVT). Given the geometrical relationship between the Voronoi tessellation and the Delaunay triangulation, the surfaces and lines connecting the Voronoi cell seeds are perpendicular to each

other by construction. For non-segregated cells, we can define the Laplacian of a function u for the Voronoi element i as:

$$\nabla^2 u_i = \frac{1}{V_i}\int_{\partial\Omega} \frac{\partial u}{\partial \mathbf{n}} d\Gamma = \frac{1}{V_i}\sum_{j=1}^{N_i} \frac{S_{ij}}{h_{ij}}\left(u_j - u_i\right) = 4\sum_{j=1}^{N_i} c_{ij}\frac{\left(u_j - u_i\right)}{h_{ij}^2} \ , \tag{3.13}$$

where N_i is the number of natural neighbors for the cell i , and $c_{ij} = S_{ij}h_{ij}/(4V_i)$ is the ratio between the volume of the vertical extruded triangular section of the Voronoi cell i sharing an edge with the cell j (see shaded area in Figure 3-2), and the total volume of the cell. For a regular square grid, Eq. (3.13) becomes the finite-difference formula for the Laplacian of a function.

In the case of vector field, like the one used in the exchange field, the Laplacian is computed for each Cartesian component:

$$\left[\nabla^2 \mathbf{u}_i\right]_k = 4\sum_{j=1}^{N_i} c_{ij}\frac{\left[\mathbf{u}_j - \mathbf{u}_i\right]_k}{h_{ij}^2} \ , \tag{3.14}$$

where $k = x, y, z$ indicates the cartesian components. In case of segregated cells, the lateral exchange field acting on cell i can be expressed as:

$$\mathbf{H}_{ex2,i} = \sum_{j=1}^{N_i} \frac{A_{ij}^{ex}}{Ms}\alpha_{ij}\frac{\left(\mathbf{m}_j - \mathbf{m}_i\right)}{\Phi_i V_i} \ , \tag{3.15}$$

where $\alpha_{ij} = \phi_{ij}S_{ij}/h_{ij}$ is the non-Sibsonian interpolator between the two neighboring segregated elements, and $\phi_{ij} = S_{ij,seg}/S_{ij}$, and $\Phi_i = V_{i,seg}/V_i$ represent the surface and volume-degree of segregation. The area of the contact surface between cell i and j, and the volume of the cell i following the segregation process are defined by $S_{ij,seg}$ and $V_{i,seg}$, respectively.

In many practical applications, the distribution of grains can be represented by a central Voronoi tessellation (CVT) with a Gaussian or Poisson distribution of the grain size [22-25]. In this case, the distance between natural neighbors is approximately equal to the distance between

their centroids. Our simulations did not show any significant difference in the evaluation of the exchange field when using the centroid distance or the seed distance in the evaluation of the exchange.

Numerically, the computation of the exchange field at each cell is accomplished by generating a matrix of geometrical and material coefficients during the preprocessing stage, and by performing sparse matrix-vector products at every linear iteration of the time-evolution solver.

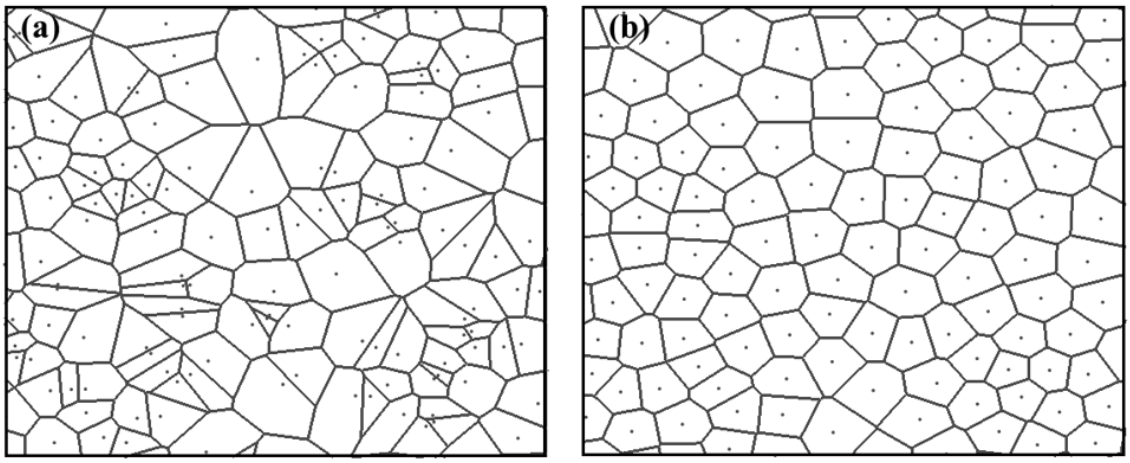

Figure 3-3: Voronoi tessellation obtained for a set of 250 seeds. The tessellation is obtained for (a) a random set of seeds and (b) a centralized Voronoi tessellation.

To validate the implementation of the exchange field given by Eq. (3.15), I studied the solution of the boundary value problem, $\nabla^2 u = f(x)$ in $\Omega = (0,1)\times(0,1)$, with $u(x) = g(x)$ on $\partial\Omega$ for a randomly distributed set of seeds (Figure 3-3a) and for a CVT tessellation (Figure 3-3b). Two tests were considered:

1) $\nabla^2 u = 0$ in Ω, with $g = x + y$ on $\partial\Omega$ (patch test),

2) $\nabla^2 u = 4$ in Ω, with $g = x^2 + y^2$ on $\partial\Omega$ (patch test).

The numerical solution for the set of the internal grains is in agreement with the analytical solution not only for the CVT, but also for a random distribution of seeds, as shown in Table 3-I.

Table 3-I: Numerical test for the Laplacian in $\Omega = (0,1)\times(0,1)$, for a random distribution of seeds (RNG) and for a centralized Voronoi tessellation (CVT). The error in the L^2 and L^∞ norm is evaluated between the analytical solution u and the numerical solution u^h for all the internal grains.

	$f(x,y)$	$u(x,y)$	$\|u-u^h\|_{L^2}$		$\|u-u^h\|_{L^\infty}$	
			RNG	CVT	RNG	CVT
I	0	$x+y$	2.62×10^{-13}	6.41×10^{-14}	2.18×10^{-12}	2.74×10^{-13}
II	4	x^2+y^2	1.95×10^{-14}	4.44×10^{-15}	2.37×10^{-12}	2.41×10^{-13}

To test the effect of the segregation on the exchange field, we consider a scalar function $u(x,y)=\sin(\pi x)\sin(\pi y)$ in $\Omega=(0,1)\times(0,1)$ for the random (RNG) and centralized (CVT) tessellation in Figure 1-1, assuming $A^{ex}/M_S = 1$ and a constant segregation coefficient ϕ_{ij} for all neighbor pairs. While the behavior of the exchange field is qualitatively similar for different chosen values of the segregation, it can be seen that for a segregation factor $\phi_{ij}=0.95$, the difference in strength between the segregated and unsegregated field reaches value of up to 10%. Under the assumption of a constant ϕ_{ij} , for both the RNG tessellation and the CVT tessellation, the reduction in strength has been found to be proportional to $1/\phi_{ij}$.

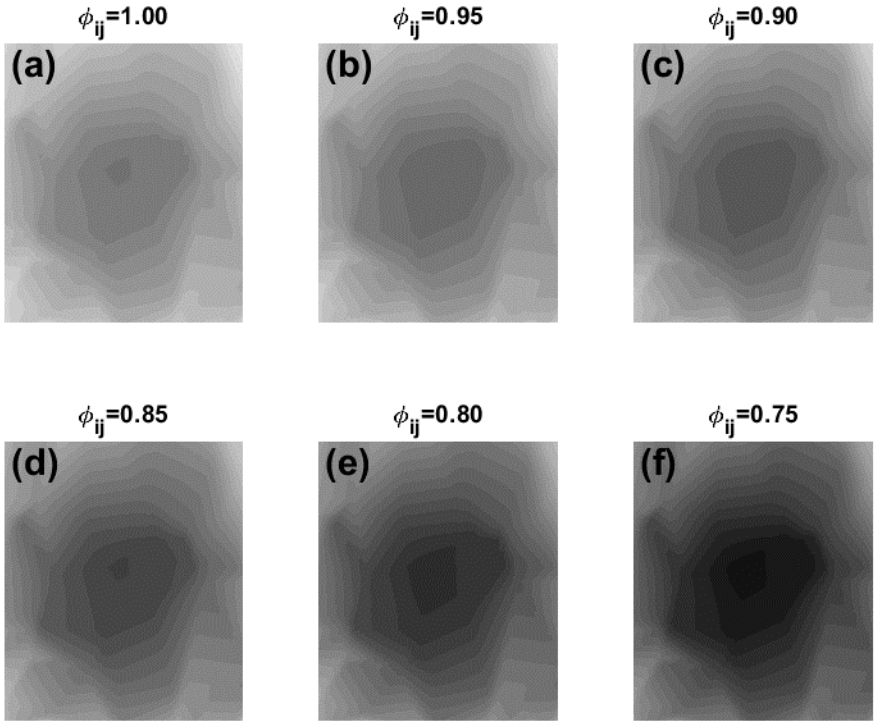

Figure 3-4: Numerical Laplacian of $u(x,y)=\sin(\pi x)\sin(\pi y)$ in $\Omega=(0,1)\times(0,1)$ for different values of the segregation coefficient ϕ_{ij} using a random distribution of the seeds.

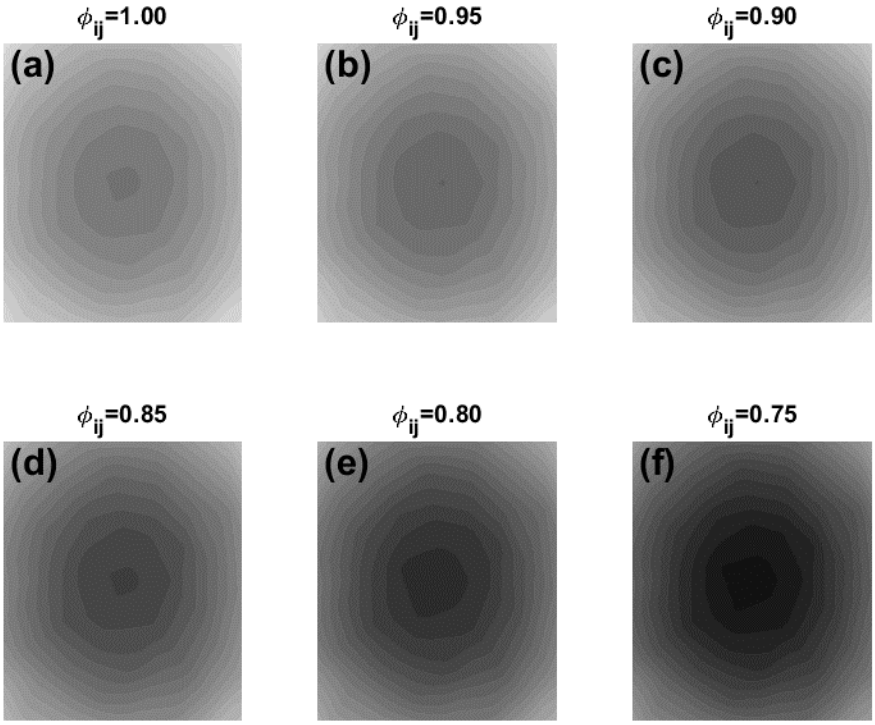

Figure 3-5: Numerical Laplacian of $u(x,y)=\sin(\pi x)\sin(\pi y)$ in $\Omega=(0,1)\times(0,1)$ for different values of the segregation coefficient ϕ_{ij} using a centralized Voronoi tessellation..

B Magnetostatic Field

Conventionally, the evaluation of the magnetostatic field is the most intensive component of computation. For a granular structure, the magnetostatic field is evaluated in two phases: (i) the magnetostatic field is computed in the dipole approximation, and (ii) the result is corrected by the exact tensorial contribution for the near field.

The point-dipole approximation assumes the magnetic dipole moment $\boldsymbol{\mu}_i$ of each Voronoi cell to be concentrated at its centroid and the shape of each individual cell is neglected:

$$\mathbf{H}_i^{dip} = \sum_{j \neq i} \begin{bmatrix} \frac{3r_x r_x - r^2}{r^5} & \frac{3r_x r_y}{r^5} & \frac{3r_x r_z}{r^5} \\ \frac{3r_y r_x}{r^5} & \frac{3r_y r_y - r^2}{r^5} & \frac{3r_y r_z}{r^5} \\ \frac{3r_z r_x}{r^5} & \frac{3r_z r_y}{r^5} & \frac{3r_z r_z - r^2}{r^5} \end{bmatrix} \boldsymbol{\mu}_i \ , \tag{3.16}$$

where $\mathbf{r}$ is the distance between the centroid of cell i and j. Equation (3.16) is written as a convolution between the summation kernel, representing the magnetostatic field due to a single point with unit magnitude, and the dipole moment $\boldsymbol{\mu}_i$.

To reduce the number of operations from $O(N^2)$ to $O(N\log(N))$ in performing the convolution, a non-uniform fast Fourier transform (NUFFT) is implemented [26]. In this approach the non-uniformly distributed dipoles are projected onto a regular grid of points. The FFTs are used for computing the spatial convolutions on this uniform grid to obtain the magnetostatic fields at the same grid points. The results are further corrected by computing the near-fields directly (without projections) through the point-dipole approximation summations going only over a small number of points surrounding each point.

The dipolar approximation alone is only sufficiently accurate when the source and observer Voronoi cells are sufficiently separated from each other. In general, it is necessary to introduce a correction for the near field. To estimate the near-field correction for cell i, a list of near-field cells j within a critical radius R_{crit} is created during the preprocessing. The critical radius is chosen such that for distances greater than R_{crit}, the dipolar approximation is accurate. The correction magnetization tensor N_{ij} is calculated for each pair (i, j) in the near-field list as:

$$\mathbf{N}_{ij} = \frac{1}{V_i}\left\{ \int_{S_i} \mathrm{d}\mathbf{S}_i \int_{S_j} \frac{\mathrm{d}\mathbf{S}_j}{|\,\mathbf{r}_i - \mathbf{r}_j\,|} - \begin{bmatrix} \frac{3r_x r_x - r^2}{r^5} & \frac{3r_x r_y}{r^5} & \frac{3r_x r_z}{r^5} \\ \frac{3r_y r_x}{r^5} & \frac{3r_y r_y - r^2}{r^5} & \frac{3r_y r_z}{r^5} \\ \frac{3r_z r_x}{r^5} & \frac{3r_z r_y}{r^5} & \frac{3r_z r_z - r^2}{r^5} \end{bmatrix} \right\}, \tag{3.17}$$

where the integration is carried over the surface of the cells i and j. The singularity of the inner integral in Eq. (3.17) is removed by using:

$$I = \int_{S_j} \frac{dS_j}{\left|\mathbf{r}_i - \mathbf{r}_j\right|} = \lim_{\epsilon \to 0} \int_{\partial(S - S_\epsilon)} \nabla_S' \cdot \left(\frac{R}{P} \hat{\mathbf{P}} \right) dS' + \lim_{\epsilon \to 0} \int_{S_j} \frac{dS'}{R} \ , \tag{3.18}$$

where $\mathbf{P}$ is the projection of the distance R on the plane of the surface [27]. Equation (3.18) trades the singular surface integral with a non-singular line integral, which can be calculated either numerically or analytically. After the singular inner integral is calculated, the remaining outer integral is calculated numerically by a quadrature rule. The resulting tensors N_{ij} are stored in the form of a sparse matrix, and the magnetostatic field acting on cell i due to the interaction with all the other cells is given as:

$$\mathbf{H}_i^{ms} = \sum_{|i-j| \le R_{crit}} N_{ij} \mathbf{M}_j + \mathbf{H}_i^{dip} \ . \tag{3.19}$$

The distance R_{crit} is chosen to ensure accuracy of the result above a prescribed threshold. To demonstrate the effect of R_{crit} on the accuracy and computational time, we consider a square surface, 300 nm in length, composed of 1200 grains with an average grain diameter of 7.1 nm. The average saturation magnetization is $M_S = 600\ \mathrm{emu/cm^3}$ with a standard deviation of $20\ \mathrm{emu/cm^3}$. The accuracy is evaluated by estimating the normalized mean square error (NMSE) between the

exact tensorial field obtained considering all $\mathcal{N}^2$ cell interactions (i.e. $R_{crit} \to \infty$), defined as $\widehat{\mathbf{Y}}_i$, and the approximated field for different values of R_{crit}, defined as $\mathbf{Y}_i$:

$$\epsilon_{R_{crit}} = \frac{\left\| \widehat{\mathbf{Y}}_i - \mathbf{Y}_i \right\|_{L^2}}{\left\| \widehat{\mathbf{Y}}_i \right\|_{L^2}} = \frac{\sum_{i=1}^{N} \left(\widehat{\mathbf{Y}}_i - \mathbf{Y}_i \right)^2}{\sum_{i=1}^{N} \widehat{\mathbf{Y}}_i^2} \ . \tag{3.20}$$

The error decreases exponentially fast for small values of R_{crit} , and asymptotically $\mathrm{NMSE}(R_{crit}) \propto 1/R_{crit}^2$ (Figure 3-6a). The results show that the error drops below 0.1% when we include in the tensorial correction not only the nearest-neighbor (nn) but also the next-nearest-neighbor (nnn) interaction, which is accurate enough for many practical purposes. For R_{crit} of the order of the cell diameter (i.e. only nn interaction), the time required to compute the tensorial and dipolar component of the magnetostatic field are of the same order, whereas for large R_{crit} the computation is dominated by the evaluation of the tensorial correction (Figure 3-6b). This is consistent with the fact that the tensorial computational cost scales quadratically with the number of surrounding cells. For $R_{crit} \sim 20\,\mathrm{nm}$, the time required to compute the tensorial correction is one order of magnitude larger than the time required to compute the dipolar field. Taking into account the NMSE and the computational time, the optimal R_{crit} appears to be the value for which only the nn and the nnn are accounted in the tensorial approximation.

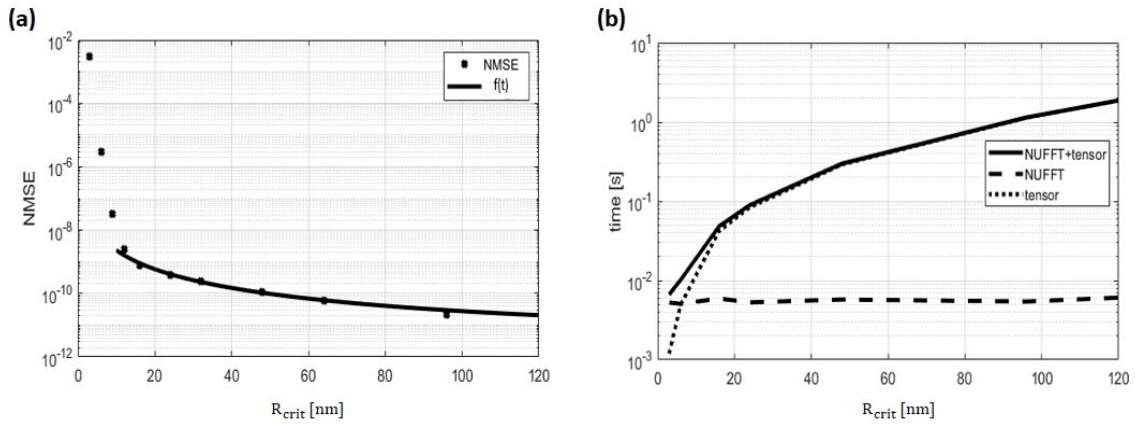

Figure 3-6: Evaluation of the magnetostatic field for a slab of $300\ \text{nm} \times 300\ \text{nm}$ with a $3\ \text{nm}$ thickness. In (a) is shown the NMSE between the semi-analytical solution and the NUFFT approximation at different R_{crit} . In (b) is shown the time required to compute the magnetostatic field (solid line), with the contribution of the dipolar field computed using NUFFT (dashed line), and the analytical tensor (dotted line), for different R_{crit} .

3.4 MODELING OF THE LASER HEATING

When a laser is shined on the surface of a ferromagnetic material, the material is heated up due to the absorption of photons by the ferromagnetic material. The heating effect of the laser is incorporated in the model by solving a coupled two temperature model (2TM), where the electron and photons are represented by two bath with electron temperature T_e and phonon temperature T_{ph}, in quasi-equilibrium, coupled via the electron-photon constant G_{e-ph}. The laser power is coupled with the electron bath, and the energy of the system is dissipated through diffusion in the electron bath. At the boundary, we implement a non-uniform boundary condition to take in account the energy dissipated outside of the system:

$$K_e \frac{\partial T_e}{\partial \mathbf{n}} = h_{bc}\left(T_e - T_{amb}\right) \qquad \text{on} \quad \partial\Omega \ , \tag{3.21}$$

where K_e is the thermal conductivity of the electron lattice, T_{amb} is the ambient temperature, and h_{bc} is the heat flux at the boundary. The magnetization dynamics and the thermal fluctuations are

coupled to the electron temperature of the system (i.e. $T = T_e(t)$). Thus, the electron temperature obtained by solving the 2TM, is used as input parameter in the LLB equation.

The thermal evolution of the electron and the phonon bath is governed by the equation:

$$C_e(T_e)\frac{\partial T_e}{\partial t} = \nabla\left[K_e(T_e, T_{ph})\nabla T_e\right] - G_{e-ph}\left(T_e - T_{ph}\right) + S(\mathbf{r}, t) \ , \tag{3.22}$$

$$C_{ph}\frac{\partial T_{ph}}{\partial t} = G_{e-ph}\left(T_e - T_{ph}\right) \ , \tag{3.23}$$

where C_e and C_{ph} denote the specific heat of the electron and the lattice, and G_{e-ph} is the coupling constant determining the energy exchange between the electron and the lattice system. For a sub-picosecond laser pulse, the value of the specific heat coefficient for the phonon bath C_{ph} and the value of the coupling constant G_{e-ph} can be assumed to be constant. The heat coefficient for the lattice and the thermal conductivity depend on the temperature [28-30]:

$$C_e(T_e) = \gamma_e T_e \ , \tag{3.24}$$

$$K_e(T_e, T_{ph}) = K_{e0}\frac{T_e}{T_{ph}} \ , \tag{3.25}$$

where γ_e and K_{e0} are material dependent constants, which are functions of the Fermi energy and the density of states. The optical source exciting the system is $S(\mathbf{r}, t) = I(\mathbf{r}, t)/\delta$, where $I(\mathbf{r}, t)$ is the laser intensity absorbed by the material and δ is the optical penetration. The laser intensity $I(\mathbf{r}, t)$ is modeled as a Gaussian pulse [31]:

$$I(\mathbf{r}, t) = 0.94\frac{F_0}{\tau_{pulse}}\exp\left[-\frac{z}{\delta} - \frac{x^2 + y^2}{w_0^2} - 2.77\frac{\left(t - 2\tau_{pulse}\right)^2}{\tau_{pulse}}\right] , \tag{3.26}$$

where $\mathbf{r} = \{x, y, z\}$ is the position vector, τ_{pulse} is the duration of the pulse, F_0 is the peak fluence of the laser, and w_0 is the radius of the laser spot.

For a sub-picosecond laser pulse, the temperature only depends on the properties of the material and, at most, on the initial magnetization of the system in the case of magnetic circular dichroism. Thus, it is possible to pre-compute the temperature dynamics as a function of space and time and use the result in solving the LLB equation. The diffusion term in Eq. (3.22) can be expressed as:

$$K_{e0}\frac{\partial}{\partial x}\left(\frac{T_e}{T_{ph}}\frac{\partial T_e}{\partial x}\right) = K_{e0}\left[\frac{T_e}{T_{ph}}\frac{\partial^2 T_e}{\partial x^2} + \frac{1}{T_{ph}}\left(\frac{\partial T_e}{\partial x}\right)^2 - \frac{T_e}{T_{ph}^2}\frac{\partial T_e}{\partial x}\frac{\partial T_{ph}}{\partial x}\right]. \tag{3.27}$$

Using Eq. (3.27) in Eq. (3.22) and discretizing the film into a regular square grid, it is possible to express the 2TM in a differential form:

$$\begin{aligned}\frac{\partial T_{e,i}}{\partial t} = {} & \frac{\alpha_i}{T_{ph,i}}\left[\left(T_{e,i+1} - 2T_{e,i} + T_{e,i-1}\right) + \frac{(T_{e,i+1} - T_{e,i-1})^2}{4T_{e,i}} - \frac{(T_{e,i+1} - T_{e,i-1})(T_{ph,i+1} - T_{ph,i-1})}{4T_{ph,i}}\right], \\ & - H_i\left(T_{e,i} - T_{ph,i}\right) + S_i(t)\end{aligned} \tag{3.28}$$

$$\frac{\partial T_{ph,i}}{\partial t} = H_i C_i (T_{e,i} - T_{ph,i}) \ , \tag{3.29}$$

where $\alpha_i = K_{e0}/(\gamma_e \Delta^2)$, $H_i = G_{e-ph}/(\gamma_e T_{e,i})$, and $C_i = \gamma_e T_{e,i}/T_{ph,i}$, with Δ as the discretization length. The source S_i is defined by the average intensity acting on the volume V_i . For a 2D grid, the finite difference scheme defined by Eq. (3.28)-(3.29) can be solved efficiently by using an alternating-direction-implicit (ADI) method, where the finite difference is split into two, (i) one taking the x-direction implicitly, and (ii) one taking the y-direction implicitly [32].

3.5 SIMULATIONS

This section presents numerical results demonstrating the performance and use of the Voronoi simulator. It includes two simulation examples illustrating the use of the simulator for modeling granular magnetic systems. The first example is a simulation of perpendicular heat assisted magnetic recording (HAMR), where each grain of the recording medium is modeled as a single domain Voronoi cell, and the temperature profile of the laser has been precomputed during preprocessing. The second example is a simulation of domain wall motion in a nanowire with strong intergranular exchange coupling.

A HAMR

Magnetic recording simulations in which the recording media is realistically and accurately modeled are invaluable for the analysis of signal quality and SNR versus areal density characteristics. Information gained from such analysis indicates the best way to optimize the recording system and the recording process for maximum storage capacity and reliability. As an example of the functionality of the simulator, we present recording simulations and analysis involving a single layer granular strip of FePt with a cross track width of 200 nm and length ranging from $1\,\mu\text{m}$ to $12\,\mu\text{m}$. The average grain diameter in the models is 7.1 nm and the thickness is 12 nm. The strip consists of ~ 500.000 grains. The material parameters are given by $M_S = 600\ \text{emu/cm}^3$, $H_K(0) = 90\ \text{kOe}$, $A_{ex}(0) = 2.2\times10^{-6}\ \text{erg/cm}$ with the easy axis along the z-axis and $\lambda = 0.1$. The anisotropy field and the exchange constant are functions of the temperature. For FePt, their dependency is given by $H_K(T) = H_K(0)m_e(T)^{0.1}$ and $A_{ex}(T) = A_{ex}(0)m_e(T)^{1.76}$, where $m_e(T)$ is the equilibrium magnetization [33].

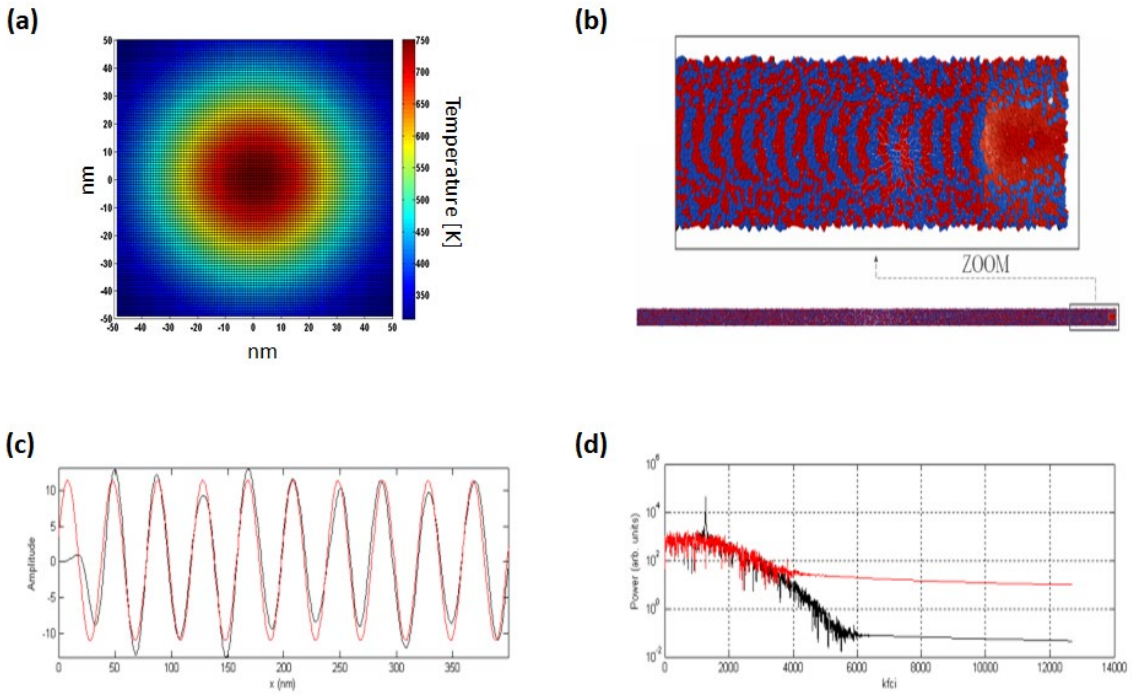

Figure 3-7: Results for the HAMR simulations. (a) Gaussian temperature profile induced by the laser. (b) Bit pattern recording for a $12\ \mu\text{m}$ strip and zoom-in showing the action of the write field. (c) Readback signal obtained from the recording (black line) and periodic fitting (red line). (d) Signal (black line) and noise (red curve) power as a function of the linear density.

The strip is subjected to an homogeneous applied field $\sim 10\ \text{kOe}$ with a switching period of $2\ \text{ns}$ (i.e. $1\ \text{ns}$ bit length), and a rise time of $\tau = 0.2\ \text{ns}$. While the laser heating is introduced by considering a Gaussian temperature profile that moves down-track at a speed of $v = 20\ \text{nm/ns}$ (Figure 3-7a). Figure 3-7b shows the pattern recorded at the linear density of $1270\ \text{kfci}$. The signal amplitude due to the finite size of the strip, the presence of thermal noise and the distribution of size and magnetic properties between grains, shows small periodic behavior that is expected in the ideal case (Figure 3-7c). The power spectrum was captured by first interpolating the magnetization pattern produced in the granular strip onto a square grid and then convolution the magnetization with the read sensitivity potential obtained for a modeled shielded red head. Comparing the signal statistics for strips of increasing length (Table 3-II), shows that the SNR

converges. The convergence is due to the increased amount of transitions being included in the statistics.

Table 3-II: Signal statistics of an HAMR simulation with a linear density of $1270\ \mathrm{kfci}$ for granular strips of different length.

	1 μm	3 μm	6 μm	9 μm	12 μm
Signal power	2.77×10^{7}	3.05×10^{8}	1.15×10^{9}	2.55×10^{9}	4.70×10^{9}
Noise power	5.29×10^{6}	2.50×10^{7}	9.26×10^{7}	1.92×10^{8}	3.72×10^{8}
SNR	7.18 dB	10.86 dB	10.93 dB	11.22 dB	11.02 dB
Jitter	3.05 nm	1.91 nm	1.88 nm	1.90 nm	1.83 nm

B Domain Wall Motion

Significant research effort has been devoted to fabrication and characterization of magnetic nanowires (NWs) for potential use in magnetic memory and logic devices. Materials fluctuations, defects, and edge roughness are known to affect domain wall (DW) propagation speed, DW pinning and depinning properties, and reproducibility, all which bear on the performance reliability of future DW-based applications[34,35]. Typical structures envisioned for such applications consist of strongly exchange coupled grains. Using the computational framework developed in this chapter it is possible to simulate domain wall motion across such structures.

Let us consider a magnetic granular film of $300\mathrm{nm}\times300\mathrm{nm}\times3\mathrm{nm}$. The left side of the film is initially magnetized “up”, while the right side of the film is initially magnetized “down”. The system is let relax, until a domain wall is created. Two cases are considered: (i) the domain wall displacement in a granular structure with a homogeneous distribution of the anisotropy field (i.e. $H_K = 12\ \mathrm{kOe}$), and (ii) the domain wall displacement in a granular structure where 3% of the grains

are pinned by an anisotropy of $H_K = 50\ \text{kOe}$. In both cases the system is assumed to be at a constant temperature $T = 300\ \text{K}$ for the duration of the simulation.

An external field H_z is applied along the negative z-direction. In the homogeneous case, the domain wall propagated freely along in the x-direction (Figure 3-8a), whereas when a distribution of the anisotropy is introduced, the domain wall shows significant deformation in the magnetic structure (Figure 3-8b). For a given applied field H_z the displacement is almost linear in the two cases (Figure 3-8c) and we can define an average velocity of the domain wall v_{steady}. The average velocity for a given external field is proportional to the average anisotropy field $\bar{H}_k$ [36], and it is given by the creep-scaling law:

$$v_{steady} = v_0 \exp\left(-\frac{\alpha}{k_b T} H^{-0.5} \right), \tag{3.30}$$

where α is the creep scaling factor. The velocity of the DW in the homogeneous and in the pinned cases for $T = 300\ \text{K}$ is fitted using Eq. (3.30) to obtain the dependence of α versus $\bar{H}_K$ (Figure 3-8d). If we define α_1 as the creep scaling factor in the homogeneous case, the results show that $\alpha \sim \left(\bar{H}_{K_1} / \bar{H}_{K_2} \right)^{5/8}$, where $\bar{H}_{K_1} = 12\ \text{kOe}$ is the anisotropy field in the homogenous case and $\bar{H}_{K_2}$ is the average value of the anisotropy field in the pinned case. This result is consistent with the experimental results [37]

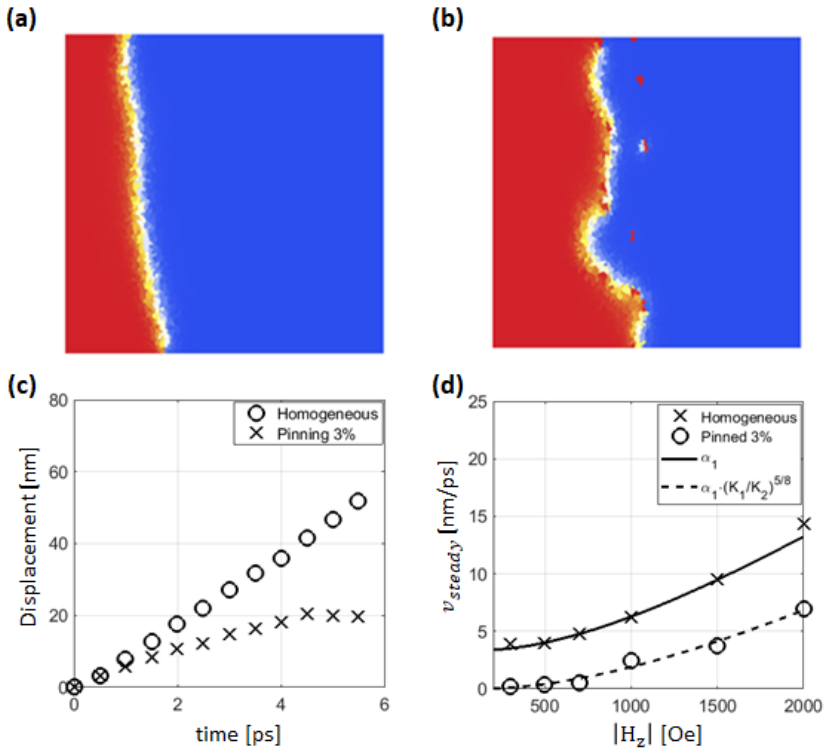

Figure 3-8: Results for the DWD. (a) Domain wall motion in a granular structure with homogeneous anisotropy after 4ps when and external field H_z is applied. (b) Domain wall motion in a granular structure where 3% of the grains are pinned with $H_K = 50\,\text{kOe}$. (c) Displacement of the domain wall as a function of time for the homogeneous (circles) and pinned (crosses) case. (d) Dependence of the domain wall speed v_{steady} as a function of the applied field. The results are fitted using the creep-law for different values of α_1.

ACKNOWLEDGEMENT

This chapter, in part, is a reprint of material as appeared in M. Menarini, M. V. Lubarda, R. Chang, S. Li, S. Fu, B. Livshitz and V. Lomakin, "Micromagnetic Simulator for Complex Granular Systems Based on Voronoi Tessellation," in Journal of Magnetism and Magnetic Materials (2019). The dissertation author was the primary investigator and author of the text used in this chapter.

Support for the work described in this chapter came from the Western Digital Corporation and NSF grants #1117911 and #1202583.

CHAPTER 4 - MICROMAGNETIC SIMULATION OF THZ SIGNALS IN ANTIFERROMAGNETIC FERH BY SUB-PICOSECOND THERMAL PULSES

This chapter presented a simulation framework for the study of THz electromagnetic field signals induced in antiferromagnetic (AFM) FeRh/Pt bilayer by sub-picosecond thermal pulses. Our model is based on the ferrimagnetic LLB model introduced in Chapter 2 and coupled with a 2TM and the simulational work has been carried out using the Voronoi simulator introduced in Chapter 3.

The FeRh film has been modeled as two identical sublattices $\mathbf{m}_1$ and $\mathbf{m}_2$, initially in the AFM state (i.e. $\mathbf{m}_1 = -\mathbf{m}_2$), coupled via an intra-lattice exchange field. The simulations showed how, due to the metamagnetic phase transition at the transition temperature T_M of this intra-lattice exchange with the temperature [38] and the break of symmetry between the sublattices produced by an external bias field, it is possible to induce a purely thermal THz spin current in the Pt due to ultrafast spin-pumping.

A similar effect was observed in a bi-axial antiferromagnetic NiO/Pt bi-layers when a canting angle θ_{12} between the magnetization of the two sublattices was generated in the direction of the hard axes with the aid of a polarized current **p** [39]. In our case, the FM intra-lattice exchange field $\mathbf{H}_{vk} = \mathbf{H}_{E,v}^{\perp}$ during the thermal excitation is at the origin of the angle between the sublattices θ_{12} . The intra-lattice exchange field acts then, as a THz field pulse when $T \leq T_M$ to bring the material back to its original configuration.

4.1 MODELING FERH/PT BYLAYER

Structurally-ordered FeRh (bcc crystal symmetry) are well known for exhibiting a first-order phase transition from antiferromagnetic (AFM) to ferromagnetic (FM) upon heating, and vice-versa upon cooling [40,41]. The magnetic phase transition in FeRh consists of three important stages: (i) nucleation, (ii) growth and (iii) coalescence of magnetic domains. During a heating event, most of the phase transition is characterized by coexistence of FM domains in a matrix of AFM domains. As the temperatures increases, densities of these domains change relatively until exchange interaction builds up between the FM domains to form large single domain. The magnetization across the transition temperature, T_M, is a continuous function of temperature yielding a transition that is relatively broad and it is about 10 K in the sample. This first order magnetic phase transition is related to the exchange constant $J_{0,vk}$ between the sub-lattices, and it is hysterical in temperature (Figure 4-1).

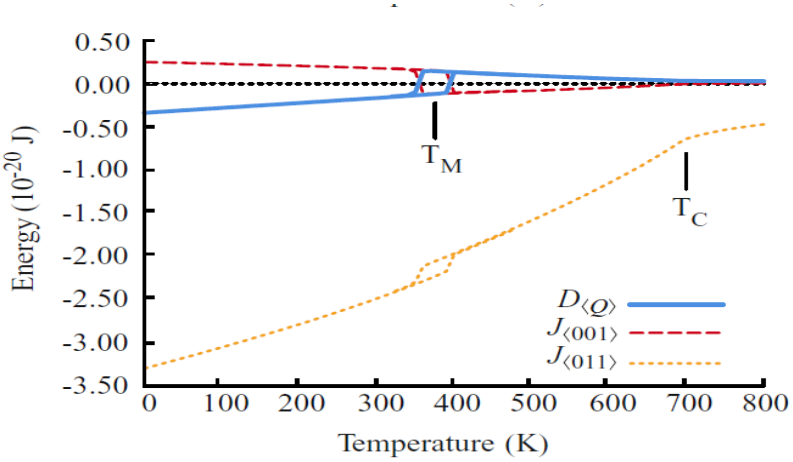

Figure 4-1: Energy contribution form the inter-lattice exchange interaction $J_{\langle 011\rangle} = J_{vk}$ (red dashed line) and the intra-lattice exchange $J_{\langle 011\rangle} = J_{v}$ (yellow dotted line). The contribution of the four-spin interaction $D_{\langle Q\rangle}$ can be included in the intra- and inter- lattice exchange. The results are reproduced from Ref. [38].

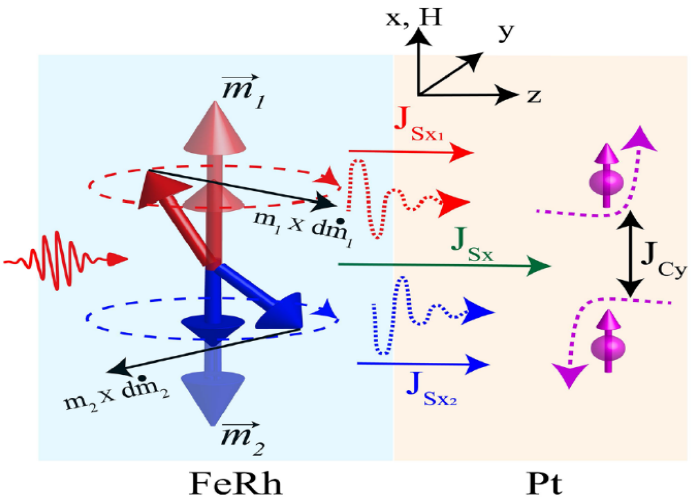

Figure 4-2: A schematic of the laser-induced spin currents at the FeRh/Pt interface. The FeRh is modeled by magnetic sublattices, $\mathbf{m}_1 = -\mathbf{m}_2$, initially in an AFM state and oriented along the direction of $\mathbf{H} = \mathrm{H}_0 \hat{\mathbf{x}}$. An ultrafast thermal pulse heats the FeRh above T_{M_2} and the intra-lattice exchange becomes FM. When the temperature drops below T_{M_2} , an spin-current $J_{S,x} = J_{S_1,x} + J_{S_2,x}$ is induced at the FeRh/Pt interface due to spin-pumping. $J_{S,x}$ is converted into a charge current $J_{C,y}$ by the ISHE. A voltage signal VISHE is generated at the output by $J_{C,y}$. The purple arrows in the Pt layer indicate electron motion bent by the spin-orbit interaction.

In order to obtain a control over the magnetic phase transition using ultrafast heating with fs-laser pulses, we investigated the generation of a thermally induced THz signal from FeRh/Pt bilayers (Figure 4-2). The magnetization in the FeRh sublattice is computed using the micromagnetic simulator. The net spin current at the interface with the Pt layer is computed from the magnetization dynamics as:

$$\mathbf{J}_{S,x} = \frac{\hbar g_{eff}^{\uparrow\downarrow}}{8\pi} \sum_{v=1}^{2} \sum_{i=1}^{N} \left[\mathbf{m}_{v,i} \times \frac{d\mathbf{m}_{v,i}}{dt} \right]_x , \tag{4.1}$$

where $\mathbf{m}_{v,i}$ is the magnetization vector of the sublattice v for the i-th cell, $\hbar$ is the Planck constant, and $g_{eff}^{\uparrow\downarrow}$ is the real part of the effective spin-mixed conductance, assumed for

simplicity equal in both sublattices [42]. The symbol $\left[\cdot\right]_x$ denotes the component x of spin current parallel to the applied field and to the FeRh/Pt interface. The injected spin current $J_{S,x}$ flowing in the *z*-direction, is converted into a charge current $J_{C,y}$ inside the Pt via inverse spin Hall effect (ISHE) [43]:

$$J_{C,y} = \theta_{ISHE}\left(\frac{2e}{\hbar}J_{S,x}\hat{\mathbf{z}}\times\boldsymbol{\sigma}\right), \tag{4.2}$$

where θ_{ISHE} is the spin Hall angle at the interface, which determines the spin-charge conversion, and $\boldsymbol{\sigma} \sim \mathbf{H}$ is the spin polarization vector. In the absence of the bias field $\mathbf{H}$ the spin polarization vector is zero and no spin current is observed in the Pt.

The magnetization dynamics of the FeRh film is model using the ferri-LLB equation given by Eq. (2.41). The effective field is obtained from the atomistic Hamiltonian is:

$$\begin{aligned}\mathcal{H} = &-J_{\langle 001\rangle}\sum_{i,j\in nn}\mathbf{S}_i\cdot\mathbf{S}_j - J_{\langle 011\rangle}\sum_{i,j\in nnn}\mathbf{S}_i\cdot\mathbf{S}_j + \frac{1}{3}\sum_{i,j,k,l}D_{ijkl}\Big[\left(\mathbf{S}_i\cdot\mathbf{S}_j\right)\left(\mathbf{S}_k\cdot\mathbf{S}_l\right)\\ &+\left(\mathbf{S}_i\cdot\mathbf{S}_k\right)\left(\mathbf{S}_j\cdot\mathbf{S}_l\right)+\left(\mathbf{S}_i\cdot\mathbf{S}_l\right)\left(\mathbf{S}_k\cdot\mathbf{S}_j\right)\Big]\end{aligned}, \tag{4.3}$$

where $J_{\langle 001\rangle}$ is the exchange energy interaction between nearest neighbors, $J_{\langle 011\rangle}$ is the exchange energy interaction between next nearest neighbors, and D_{ijkl} are the four spin exchange that plays a role in stabilizing the AFM domains. For simplicity, in the rest of the formulation the contribution of the 4-spins interaction has been neglected. The effective field and the molecular field are then equivalent to the ones introduced in Eq.(2.32)-(2.33) .The intra-lattice exchange can be rewritten as:

$$\mathbf{H}_{vk} = \mathbf{H}^{\perp}_{E,v} = \frac{J_{0,vk}}{\mu_0}\left[\mathbf{m}_k - \frac{\mathbf{m}_v\cdot\mathbf{m}_k}{|m_v||m_v|}\mathbf{m}_v\right], \tag{4.4}$$

where $J_{0,vk} = qxJ_{\langle 001 \rangle}$ is the micromagnetic exchange between sublattices, and $J_{\langle 001 \rangle}$ is the nearest neighbors exchange integral for FeRh, $x = 6$ is the number of nearest neighbors, and $q = 0.5$ is the density of elements for the sublattice v. For FeRh, the exchange integral $J_{\langle 001 \rangle}$ is a function of the temperature [38,44], and its value has a transition from AFM to FM while heated above $T_{M_2} = 400\ \mathrm{K}$ and from FM to AFM when cooled below $T_{M_1} = 350\ \mathrm{K}$. This transition is responsible for the change in sign of $\mathbf{H}_{vk}$ during the magnetization dynamics.

4.2 SIMULATION OF THZ SIGNAL

Let us consider a FeRh film of $300\ \mathrm{nm} \times 300\ \mathrm{nm} \times 3\ \mathrm{nm}$. The system is discretized into regular cubic cells with a length $L = 3\ \mathrm{nm}$. The system is initially in the AFM phase at a temperature $T = 300\ \mathrm{K}$ so that the magnetization of the two identical sublattices are antiparallel and directed along the x axis (i.e. $m_{1,x} = -m_{2,x}$). A bias field $\mathbf{H} = 5\ \mathrm{kOe}$ is applied along the x direction. At time $t = 0$ the film is subjected to a thermal excitation, modeling the laser with a duration of $\tau_{pulse} = 50\ \mathrm{fs}$. The pulse is modeled as a homogeneous power source along the xy plane, such that the absorbed intensity is given by:

$$I(t) = I_0 \exp\left[-2.77 \left(\frac{t - 2\tau_{pulse}}{\tau_{pulse}} \right)^2 \right], \tag{4.5}$$

where I_0 is the effective peak power absorbed by the material. The saturation magnetization in the two sublattice $M_{S,v}^0 = M_S^0 / 2$ is obtained from the saturation magnetization of FeRh in the FM state M_S^0. The parameters used in the simulations are given in Table 4-I.

Table 4-I: Magnetic and thermal properties for the FeRh film obtained from Ref. [38]

Symbol	Value	Unit	Description
λ	0.05		Atomistic damping
$M_{S,v}^{0}$	540	emu/cm^3	Saturation magnetization
$H_K(0)$	9	kOe	Anisotropy field
$J_{0,vk}(0)$	-1.2×10^{-14}	erg	Intra-lattice exchange energy
$A_{ex}(0)$	4×10^{-7}	erg/cm	Exchange constant
T_{M_1}	400	K	Transition temperature (AFM-FM)
T_{M_2}	350	K	Transition temperature (FM-AFM)
T_C	700	K	Curie Temperature
γ_e	3.5×10^{-3}	J mol^{-1}K^{-2}	Electron heat capacity constant
C_l	4.54×10^{1}	J mol^{-1}K^{-1}	Phonon specific heat capacity
G_{e-ph}	1.05×10^{12}	J mol^{-1}K$^{-1}s^{-1}$	Electron-photon coupling

Below the transition temperature T_{M_1}, the intra-lattice exchange scales with the saturation magnetization as $J_{0,vk}(T) \sim m_e(T)^{1.93}$. Above T_{M_2}, a crossover behavior occurs, and the exchange integral becomes positive. The transition from the AFM/FM state is gradual with a slope of $\Delta_{T_M} = 10\,\mathrm{K}$.

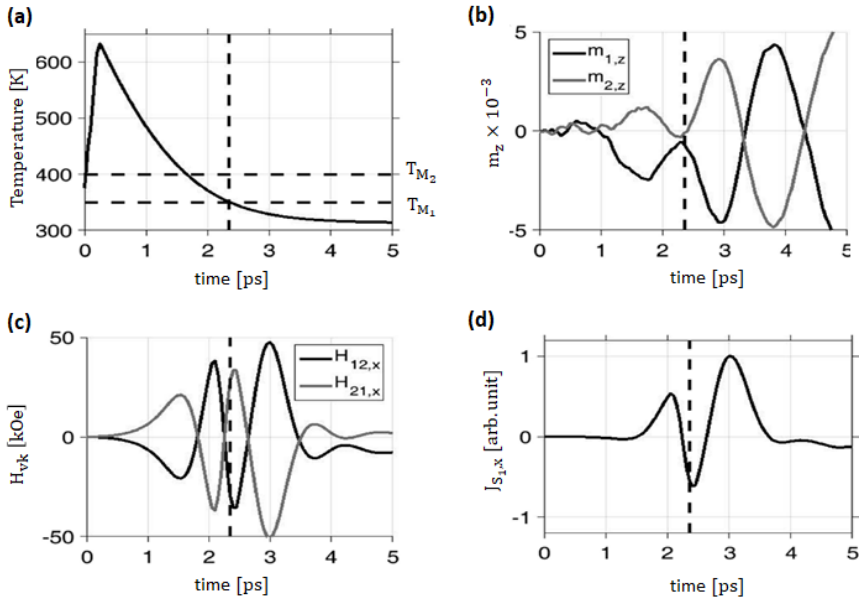

Figure 4-3: Results for the spin-current induced in FeRh. (a) Temperature dynamics induced by the laser. The horizontal dashed lines indicate the transition points T_{M_1} and T_{M_2}. The vertical dashed line indicates the time of transition from the FM to the AFM exchange. (b) Precession induced on the magnetization components $m_{1,z}$ and $m_{2,z}$. (c) Dynamics of the intra-lattice exchange induced on m_1 (black line) and on m_2 (grey line). (d) Renormalized value of the spin-current generate by the sublattice 1 into the Pt layer.

The thermal pulse given in Eq.(4.5) excites the film above T_{M_2} within ~ 10 fs and the intra-lattice exchange initially in the AFM state ($J_{0,vk}(T) < 0$) is in the FM state ($J_{0,vk}(T) < 0$) (Figure 4-3a). The magnetization of the sublattices are subjected to a longitudinal ultrafast demagnetization due to the rapid change in temperature. After T_e reaches its peak, the electron system starts to cooldown and within ~ 2 ps the electron bath reaches the equilibrium temperature $T_e = T_{ph} < T_{M_1}$. During the cooldown, the magnetization vector in the two sublattices are subjected to a small re-magnetization. The random fluctuations introduce small

deviations from the equilibrium on the yz plane. Since the sublattices are no longer anti-parallel, the intra-lattice exchange field is proportional to:

$$\mathbf{H}_{vk} \sim (1-\cos(\theta_{12})) \ , \tag{4.6}$$

where θ_{12} is the local angle between the two sublattices. Since the intra-lattice exchange is positive during the cooldown, the magnetization $\mathbf{m}_1$ and $\mathbf{m}_2$ starts to align decreasing the value of θ_{12} (Figure 4-3b). When the temperature is reduced below the transition point T_{M_1}, as the electron system cools down, the intra-lattice exchange energy decreases rapidly and return in the AFM state. The intra-lattice exchange field at the transition point acts on the two sublattices like a THz field pulse with $f_{vk} \sim 1\,\mathrm{THz}$ and with an amplitude $|H_{vk}| \sim 50\,\mathrm{kOe}$ in the x-direction (Figure 4-3c). The intra-lattice exchange generates a spin-current $J_{S_1,x}$ and $J_{S_2,x}$ in the two sublattices (Figure 4-3d). The net spin current induced on Pt is given by the sum of the spin currents in the sublattices.

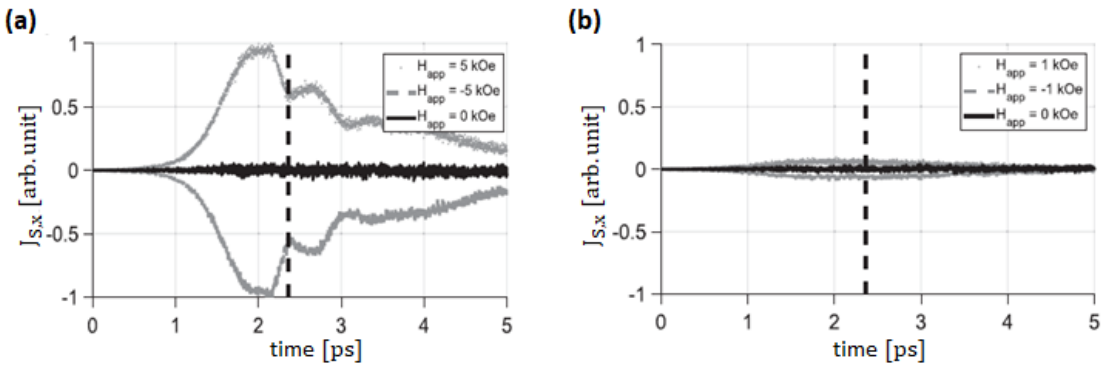

Figure 4-4: Renormalized net spin-current injected into the Pt layer by spin pumping for $\mathrm{H} = 5\,\mathrm{kOe}$ (dotted grey line), $\mathrm{H} = -5\,\mathrm{kOe}$ (dashed grey line), and $\mathrm{H} = 0\,\mathrm{kOe}$ (solid black line). The results are shown for (a) FeRh, and for (b) a hypothetical AFM magnetic material that doesn't show a phase transition below T_C.

In the absence of an applied field, the net spin current induced in Pt is zero. The presences of an external bias field in the direction of the magnetization is enough to break the symmetry between the two sublattices and generate a net non-zero spin current that is at the origin of the THz signal (Figure 4-4a). If the material does not present a phase transition below T_C (pure AFM), the net spin current is approximately zero even in the presence of a symmetry breaking field (Figure 4-4b).

4.3 SUMMARY

In this chapter, we presented a modified version of the LLB model for ferrimagnets to simulate the behavior of a material that shows a first-order phase transition from AFM to FM upon heating. The framework has been used to simulate the generation of a THz signal in a FeRh/Pt bilayer induced by a thermal pulse.

The results show that the intra-lattice exchange between the two sublattices generates a spin-current in the two sub-lattices. The net spin-current generated in zero, unless an external source breaks the symmetry between the two lattices. This symmetry breaking effect is produced in the model by an external bias field in the direction of the magnetization.

ACKNOWLEDGEMENT

This chapter, in part, is a reprint of material as appeared in M. Menarini, R. Medapalli, E. E. Fullerton and V. Lomakin, "Micromagnetic simulation of THz signals in antiferromagnetic FeRh by sub-picosecond thermal pulses," in AIP Advances 9, 035040 (2019). The dissertation author was the primary investigator and author of the text used in this

chapter. This work was supported as part of the Quantum-Materials for Energy Efficient Neuromorphic-Computing (Q-MEEN-C), an Energy Frontier Research Center funded by the U.S. Department of Energy, Office of Science, Basic Energy Sciences under Award # DE-SC0019273.

CHAPTER 5 - A PHENOMENOLOGICAL THEORY OF THE OPTICAL MAGNETIZATION REVERSAL

Increasing the magnetization reversal speed and the speed of domain wall motion has been a subject of interests in magnetic memory devices. In general, logics bits are obtained by selectively setting the magnetization vector of individual domains in a particular direction to represent binary strings of 0s and 1s. The fastest and most efficient of these systems available commercially involves precessional switching driven by a magnetic field. In these devices an external field B_p is applied as a write pulse over a time period τ. The magnetization vector precesses around the field until $B_p\tau$ reaches a certain value at which the switching occurs. However, for pulse of the duration on the order of $\tau \approx 1\,\text{ps}$, the switching occurs randomly over a wide range of magnetic fields [45] due to the non-uniform magnetization dynamics. This non-uniform excitation put a limit to how fast the magnetization reversal can be driven by using an external applied field.

A faster alternative to magnetic induced reversal was first demonstrated experimentally by Stanciu et al. [46] in ferrimagnetic GdFeCo using sub-picosecond circular polarized laser pulses. The reversal in such a material was attributed to a combination of two phenomena: (i) a helicity dependent difference in absorption by the media depending on the polarization of the light and the direction of the magnetization, due to a magnetic circular dichroism (MCD), (ii) a transient ferromagnetic exchange above the compensation temperature between the two antiferromagnetically coupled sublattices[47,48]. The combination of the two effect can give rise to reversal by both linear and circular polarizations.

Similar optical reversal has been observed in ferromagnetic CoPt multilayer films and granular FePt when excited by multiple sub-picosecond circular polarized pulses [24,49]. Due to the nature of these materials, and the lack of two antiferromagnetically coupled sublattices, the mechanism used to explain the magnetization reversal in ferrimagnetic material is not able to explain the optically induced reversal in ferromagnets.

This chapter presents a model of the physical process of the magnetization driven by an optical excitation and electronic demagnetization. The model can be used to describe the phenomenon of helicity-dependent all-optical magnetic switching (HD-AOS) and helicity-dependent domain wall displacement (HD-DWD) observed in ferromagnetic FePt and CoPt films and granular media subjected to a series of sub-picosecond laser pulse. Other models have tried to explain HD-AOS in ferromagnets using MCD, varying the fluency absorbed in the two temperature model based on the direction of the magnetization [50,51], or assuming the existence of a strong optically induced magnetic field produced by the interaction of the magnetic material with the light via the inverse Faraday effect (IFE).

The MCD studies showed that assuming a difference in absorption between the magnetization of the order of $\Delta_{MCD} = 3-5\%$ it is possible to simulate a partial reversal in FePt or CoPt. These values of Δ_{MCD} overestimate those observed in experiments, where the difference in absorption has been shown to be of the order of 1% [52-54]. In out simulations we find that for the difference of the order of 1% the effect of the thermal fluctuations is enough to counter the effect of the magnetic circular dichroism.

The existence of the IFE has been demonstrated in experiments [55-57]. The IFE is a special case of the angular momentum transfer mechanism from photon to electron spin,

confined to the second order of the oscillating electric field. The effective magnetic field that IFE is expected to produce bases on theoretical results and the duration of the field through the ultrafast laser pulse are inadequate to explain the AOS experiments. In particular, it has been shown that to produce a consistent switching the duration of the induced IFE field has to be 2-5 times longer than the laser pulse that generates it and the magnetic field strength has to be extremely strong [50].

In our model, the optical excitation rises naturally from the equation of motion of the magnetization, instead of being introduced through an artificial field or difference in absorption.

5.1 HELICITY-DEPENDENT OPTICAL EXCITATION

A ferromagnetic material with an out-of-plane uniaxial anisotropy has two possible stable state for the magnetization. The magnetization is defined to be "up" if the magnetization vector in the direction of the positive z-axis, and "down" if the magnetization vector is in the direction of the negative z-axis.

In the HD-AOS experiments, a magnetic material initially in a random magnetic state (i.e. demagnetized film or equal numbers of grains in the up/down state) is excited by a ~ 100 fs pulsed laser source and subsequently imaged via the Faraday rotation. The repetition rate of the laser is of the order of ~ 1 kHz giving enough time for the material to relax back to room temperature (no thermal accumulation). Figure 5.1-1a shows that in the presence of a circular polarized light a net magnetization (white and dark domains) is attained, while no net magnetization is observed with linear polarization. In particular, σ_+ polarization leads to a net magnetization in the "up" state and σ_- to a net magnetization in the "down" state. Figure 5.1-1b

shows that the generation of the domain is a function of the fluency of the laser. The nucleation of a domain is only observed for fluencies higher that a threshold value F_1. Increasing the fluence above F_2 only thermal demagnetization is observed. This behavior leads to the characteristic ring pattern observed in HD-AOS experiments where the center of the media is demagnetized (higher fluency), and the optical reversal is only observed in a small range of fluencies $F_1 \leq F \leq F_2$.

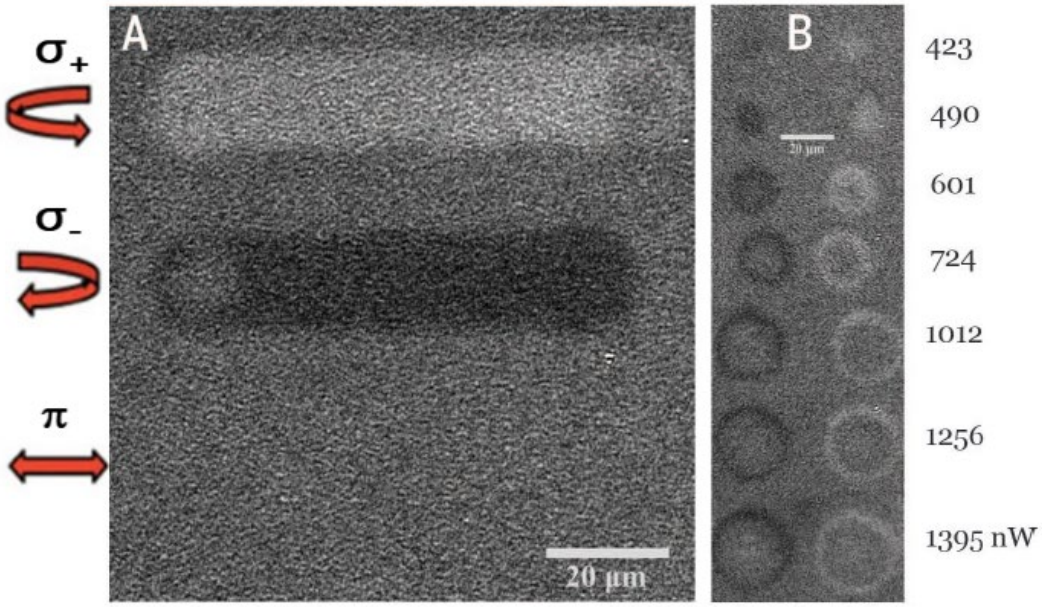

Figure 5-1: Magneto-optical response in zero field of a 15-nm FePt granular film sample starting from the demagnetized state. (A) laser scans for σ_+ , σ_- , and linear polarized light (π). (B) images of the magnetic domain written by keeping the laser at a fixed position of the sample for σ_+ (black domains) and σ_- (white domains) at different laser powers. Reproduced from the original work in Ref. [24].

Recent experiments have shown that the HD-AOS reversal in ferromagnets is the product of two effects [58]:

1) A domain nucleation that is skewed in the direction preferred by the circular polarization.
2) An ultrafast expansion of the domains favored by the circular polarization due to helicity-dependent domain wall displacement.

The helicity dependent domain wall displacement has been observed for fluencies below the one required to observe nucleation [52,59]. In these experiments, the center of the laser beam (i.e. the peak fluency) is focused between two domains. The system is then subjected to a series of *N* pulses and the displacement of the domain wall is measured (Figure 5.1-2a). The center of the laser represents the hottest region in the sample. For linearly polarized light, the domain wall tries to move toward the hottest region due to thermal displacement. When a circular polarized source is present, the domain wall moves from the hottest region expanding the domain based on the light helicity (i.e. σ_+ would expand the "up" domain, and σ_- would expand the "down" domain). If the fluence is too low, $F < F_0$, no significant domain wall displacement is observed.

For a given peak fluency of the laser, the displacement is then a function of the light helicity. Figure 5.1-2b shows the displacement as a function of the helicity. The maximum displacement happens for the circular polarized light (i.e. σ_+ and σ_-) and zero for the linear polarized light. We argue that HD-DWD results from the balance of 3 contribution:

1) Domain wall pinning: the optical/thermal energy must overcome the energy barrier to move the domain wall.
2) Light helicity: the helicity defines the speed and the direction of the displacement and tends to move the domain wall toward the colder region.

3) Temperature gradient induced by the laser heating: the temperature gradient counters the effect of the light helicity trying to move the domain wall toward the hottest region.

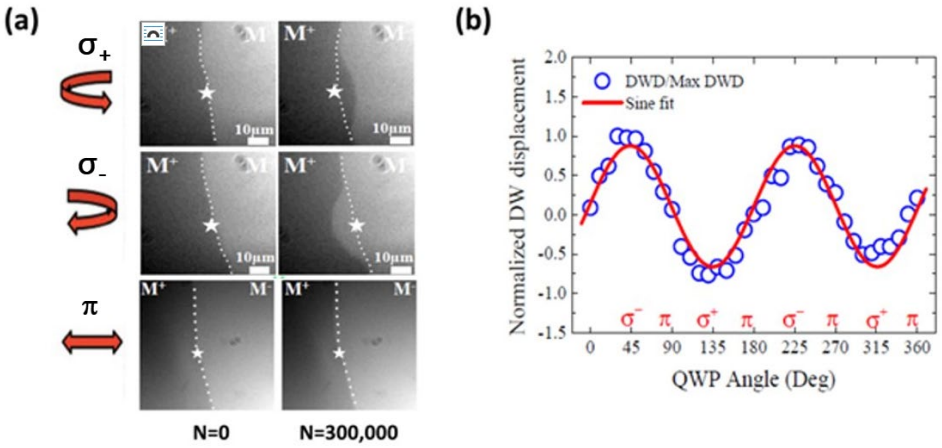

Figure 5-2: (a) Magneto-optical images of HD-DWD in CoPt for a ~ 40 fs laser pulse with circular polarization σ_+ , σ_- , and for linear polarization (π). The star indicates the center of the beam spot and N is the number of laser pulses. (b) Normalized domain wall displacement induced as a function of the percentage of light helicity. Reproduced from the original work in Ref. [59]

The balance between the thermal gradient and degree of helicity determines the maximum displacement of the domain wall. Decreasing the degree of helicity from the circular polarized to linear polarized light would displace gradually the domain wall toward the center of the laser.

5.2 THREE LEVEL LAMBDA SYSTEM

Our aim is to build a model (i) of the physical process of the magnetization reversal, which is driven by an optical excitation and electronic demagnetization, (ii) to which the thermal effects such as laser heating may be added, and (iii) ready for numerical simulations.

In this section, we concentrate on the first step. The model contains three key states: two ferromagnetic ground states separated by uniaxial anisotropy and an optically excited state.

We describe the basic optical process as the circularly polarized laser pulse exciting the initial ferromagnetic ground state to an excited state with energy above the anisotropy potential barrier between the two ground states and a sufficient amount of spin reversal to bias the state against reverting back to the original magnetic ground state. The excited state decays by the spin-conserved electron-electron interaction fast electron processes to the low-energy excited states in the anisotropy energy valley of the reversed magnetization ground state. The decay to the final ground state is dominated by interactions between phonons and magnons. The optical excitation leg is reasoned to be supported by the extant experiments and theories and the fast decay leg supported by the electronic causes of the demagnetization process, both of which are incorporated in this section.

In a ferromagnet, the proximate energy above the two ground states and around the optically excited state are the charge and spin states, the latter including the magnons in the Heisenberg model or the spin-flip excitations in the Stoner model [60,61]. This scenario is equivalent to rendering the skeleton three states to an open system. Thus, the Λ system may be treated by the quantum dynamics of a standard three-level system [62], governed by coherent and incoherent optical excitations with the upper level subject to a fast dissipation to the reversal state. The continua around these three states are represented by three probability distributions of the three states to provide the fluctuation effects of the magnetic sector and of the optical sector. The equations of motion with fluctuations are equivalent to the modified Bloch equations for the two-level system [63,64].

The three key basis states of all the spins of the system, shown in Figure 5.2-1, are $|1\rangle$, $|2\rangle$, the two macrospin ferromagnetic ground states in a uniaxial anisotropy system and $|3\rangle$ an optically excited state. State $|2\rangle$ is chosen to be the initial magnetization state that can be excited by a right-handed (σ_+) circularly polarized light to an excited state $|3\rangle$ of reversed magnetization, which decays without change in magnetization direction into the reversal state $|1\rangle$.

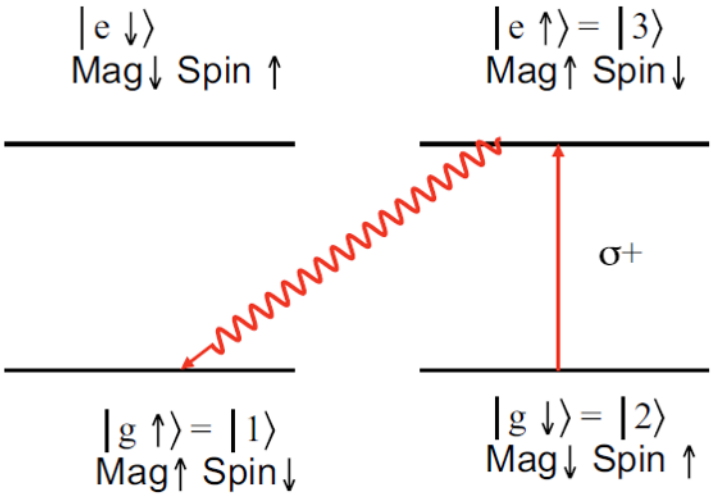

Figure 5-3: Schematic representation of the three-level system. The labels $|g_\uparrow\rangle = |1\rangle$ and $|g_\downarrow\rangle = |2\rangle$ denotes the magnetization-up and the magnetization down in the ground state, respectively. $|e_\uparrow\rangle = |3\rangle$ denotes the magnetization-up excited state. The optical transition from the $|2\rangle$ to $|3\rangle$ is driven by the σ_+ light. The relaxation from $|3\rangle$ to $|1\rangle$ is a fast-non-spin flip process, which is a non-radiative Coulomb interaction induced decay. The fourth state $|e_\downarrow\rangle$ is present to indicate a possible pathway for the σ_- light.

Because the Λ system is open, subject to control and dissipation, we represent its mixed state by a density operator $\hat{\rho}$. We find it useful to transform the matrix elements to the defined Bloch vectors for pairs of states, in particular, the magnetization vector $\mathbf{m}$ between the

magnetization states $|1\rangle$ and $|2\rangle$, the polarization $\mathbf{p}$ between the optically connected states $|2\rangle$ and $|3\rangle$, and, similarly, polarization $\mathbf{d}$ of the fast decaying channel between states $|3\rangle$ and $|1\rangle$:

$$\hat{\rho} = \begin{bmatrix} \rho_{11} & \rho_{12} & \rho_{13} \\ \rho_{21} & \rho_{22} & \rho_{23} \\ \rho_{31} & \rho_{32} & \rho_{33} \end{bmatrix} = \frac{1}{2} \begin{bmatrix} 1+m_z & m_- & d_+ \\ m_+ & -(m_z+p_z) & p_+ \\ d_- & p_- & 1+p_z \end{bmatrix} , \tag{5.1}$$

where the three transverse components are contained in

$$m_\pm = m_x \pm i m_y , \tag{5.2}$$

and, similarly, for $p_\pm$ and $d_\pm$. The unit trace of the density matrix constrains the choice of the longitudinal component to two components

$$m_z = \rho_{11} - \rho_{22} - \rho_{33} , \tag{5.3}$$

$$p_z = -\rho_{11} - \rho_{22} + \rho_{33} , \tag{5.4}$$

which we refer to, respectively, as magnetization and optical polarization for the convenience of computation and their correct limiting case behavior. When state $|3\rangle$ is vacant, $p_z = -1$, then the upper left 2 × 2 submatrix represents the spin sector with the off-diagonal terms as leakage, and similarly for the optical sector for the lower submatrix at the initial magnetization state when $m_z = -1$, and for the decay sector of states 1 and 3 when $m_z = -p_z$.

The density operator is a Hermitian operator subject to two restrictions: (i) it is positive (easily tested by its eigenvalues be $\lambda \geq 0$); (ii) its trace is $\mathrm{Tr}(\hat{\rho}) = 1$. It follows that $\mathrm{Tr}(\hat{\rho}^2) \leq 1$, where the equality holds if and only if the state is pure. In a two-state system, the Bloch vector is confined to a sphere with its surface defined by $\mathrm{Tr}(\hat{\rho}^2) = 1$ for pure states. However, in systems with more than two states, the corresponding hypersphere does not present

a dividing hypersurface for valid representation of states. The issue is discussed in Appendix A. The second issue is that the mapping between the density matrix elements and the polarizations (optical and magnetic) is not a one-to-one mapping [65]. An obvious example is the two dimensional submatrices, where spin 1/2 rotation has a period of 4π and not 2π [66], arising from the phase terms in the non-diagonal elements. Because the three key states are macrospin states, we may consider the mapping one-to-one, neglecting the subtle quantum features such as the spin 1/2 case, whence the complete rotation of the macro-spin polarization vector is 2π .

We model the dynamics of the magnetization as that of the Λ system of three most probable or average states. The continua surround the respective macrospin states and they are treated as an environment that makes the dynamics of an open system. Therefore, the macrospin equations of motion contains coherent driving terms, incoherent pumping terms, and dissipative terms. A formal method to include the dissipation terms in the Markovian approximation is by expressing the master equation of the reduced density matrix of the macrospin state, known as the Lindblad equation[67], in terms of both the unitary Hamiltonian and the Lindblad operators $\hat{L}_k$,

$$\frac{d\hat{\rho}}{dt} = -i[\widehat{\mathcal{H}}, \rho] + \sum_{k=1}^{3}\left(\hat{L}_k \hat{\rho} \hat{L}_k^{\dagger} - \frac{1}{2}\{\hat{L}_k^{\dagger}\hat{L}_k, \hat{\rho}\} \right) . \tag{5.5}$$

The first term on the right drives the unitary dynamics by the Hamiltonian $\widehat{\mathcal{H}}$ in units of frequency, reduced in the rotating wave approximation of the optical frequency between state $|1\rangle$ and $|3\rangle$, to the matrix representation in the basis set of the LLL model,

$$\widehat{\mathcal{H}} = \begin{bmatrix} B_z & B_- & 0 \\ B_+ & -B_z & -\frac{i}{2}\Omega_{\sigma_+} \\ 0 & \frac{i}{2}\Omega_{\sigma_+} & \Delta_{23} - B_z \end{bmatrix}. \tag{5.6}$$

Here, $\mathbf{B} = \gamma \mathbf{H}_{\text{eff}}$, where γ is the gyromagnetic ratio assumed to be the same for the excited and ground states and $\mathbf{H}_{eff}$ is the effective magnetic field including the contribution from the applied, anisotropic, magnetostatic, and mean-field approximation of the micromagnetic exchange defined in Chapter 2. The optical excitation is introduced via the Rabi frequency of the σ_+ light, Ω_{σ_+} defined by:

$$\Omega_{\sigma_+} = \frac{2\mu_{23}E^+}{\hbar}, \tag{5.7}$$

where $\hbar$ is the Plank constant, E^+ is the amplitude of electric field related to the σ_+ light , and μ_{23} is the electron transition dipole moment between state $|2\rangle$ and $|3\rangle$. In addition, Δ_{23} in Eq.(5.6) is the detuning of the light frequency from the resonance frequency between states $|2\rangle$ and $|3\rangle$. The second term in the right-hand side of Eq. (5.5) is composed of the dissipative energy terms given in terms of the Lindblad operators $\hat{L}_k$. Details of the construction of these operators and equations are given in Appendix B.

When the density matrix is converted to the eight components of the polarizations and magnetizations, we obtain a system of equations that describes the magnetization dynamic of the magnetic system excited by a circular polarized light source:

$$\frac{d}{dt}m_x = 2(B_y m_z - B_z m_y) + B_y(1 + p_z) - \frac{1}{2}\Omega_{\sigma_+} d_x \ , \tag{5.8}$$

$$\frac{d}{dt}m_y = 2(B_z m_x - B_x m_z) - B_x(1+p_z) - \frac{1}{2}\Omega_{\sigma_+} d_y \ , \tag{5.9}$$

$$\frac{d}{dt}m_z = 2(B_x m_y - B_y m_x) + \Gamma_l(1+p_z) \ , \tag{5.10}$$

$$\frac{d}{dt}p_z = \Omega p_x - \Gamma_d(1+p_z) \ . \tag{5.11}$$

$$\frac{d}{dt}p_x = -\Delta_{23}p_y - \frac{\Omega_{\sigma_+}}{2}(2p_z + 1 + m_z) + (B_x d_y + B_y d_x) - \Gamma_t p_x \ , \tag{5.12}$$

$$\frac{d}{dt}p_y = \Delta_{23}p_x - (B_x d_x - B_y d_y) - \Gamma_t p_y \ , \tag{5.13}$$

$$\frac{d}{dt}d_x = (2B_z - \Delta_{23})d_y + \frac{1}{2}\Omega_{\sigma_+} m_x - (B_x p_y - B_y p_x) - \Gamma_t d_x \ , \tag{5.14}$$

$$\frac{d}{dt}d_y = -(2B_z - \Delta_{23})d_x - \frac{1}{2}\Omega_{\sigma_+} m_y - (B_x p_x + B_y p_y) - \Gamma_t d_y \ . \tag{5.15}$$

The magnetic relaxation is left out of the equation to focus on the optical excitation. The damping component can be re-inserted by means of the Lindblad operators in the magnetization sector or using the phenomenological damping of the LLB equation. The longitudinal decay rate Γ_l, is taken to be equal to the Coulomb collapse rate Γ_d of the channel d described in Appendix B, while the transverse decay rate Γ_t is a function of the pure dephasing rate Γ^* :

$$\Gamma_t = \frac{\Gamma_d}{2} + \Gamma^* \ . \tag{5.16}$$

In the optical excitation from state $|2\rangle$ to $|3\rangle$, the localized orbital of an electron in the macrospin state goes from d (or f) to p (or d), respectively, with an angular momentum decrease of one $\hbar$ by the σ_+ photon traveling against the spin axis via the optical dipolar interaction. The optical process by itself does not flip the electron spin. The switch is caused by the spin-orbit coupling of the optically involved states to spin-flip states [68,69]. The total angular momentum conservation may be broken by other causes in experiment [70] and in

theory [69]. In the case of HD-AOS, this can be achieved using polarized light, as shown in experiment [71], and can be explained in theory [72] by time-reversal symmetry breaking of the ferromagnetic material. The driving mechanism of the laser pulse is modeled by a coherent drive Ω_{σ_+} between states $|2\rangle$ and $|3\rangle$, which is proportional to the optical electric field.

The relaxation process largely preserves the spin direction through the non-radiative Coulomb collapse, which is much faster than spin relaxation. Since the single electron conserves its spin direction in the electron-electron scattering process, the system favors the decay from $|3\rangle$ to $|1\rangle$ over the decay from $|3\rangle$ to $|2\rangle$. The electron relaxation process also plays a strong role in the sub-picosecond demagnetization under fast optical excitation, as found in a variety of fast optics experiments [73]. The loss of the MOKE contrast of the remnant magnetization saturating at high excitation densities was associated with an instantaneous "Stoner gap collapse" in the same paper. This fast relaxation is explained by an electron scattering theory [74] and computations using the density functional theory [75], which includes the electron-electron interaction in the spin polarized configuration.

5.3 FOUR LEVEL LAMBDA SYSTEM

In the previous section we have developed a model to describe the optical excitation of a magnetic media due to the interaction with the circular polarized light using a three level Λ system. The model can be expanded to take into account all forms of polarization including linear and elliptical light. The system can be described by a two Λ system in which the two optically excited states are not optically connected. The pathway for the σ_- optical excitation is built by symmetry.

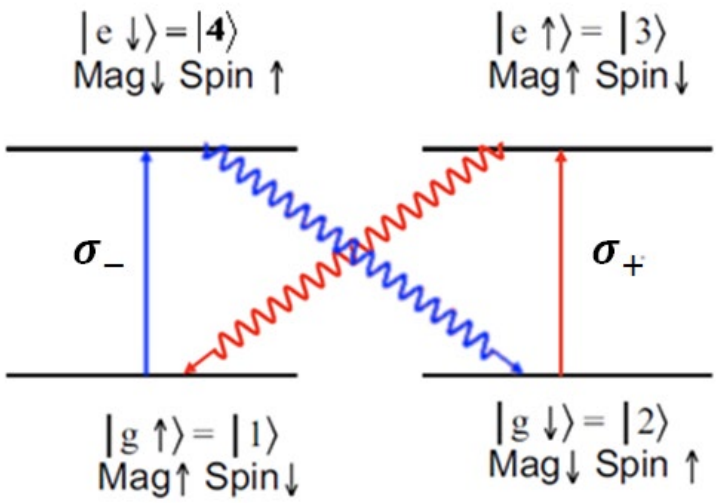

Figure 5-4: Schematic representation of the four-level system. The labels $|g_{\uparrow}\rangle = |1\rangle$ and $|g_{\downarrow}\rangle = |2\rangle$ denotes the magnetization-up and the magnetization down in the ground state, respectively. While $|e_{\uparrow}\rangle = |3\rangle$ and $|e_{\downarrow}\rangle = |4\rangle$ denotes the magnetization-up and magnetization-down excited states, respectively. The optical transition from $|2\rangle$ to $|3\rangle$ is driven by the σ_+ and the optical transition from $|1\rangle$ to $|4\rangle$ is driven by the σ_-. The relaxation from $|2\rangle$ to $|3\rangle$ and from $|4\rangle$ to $|2\rangle$ are fast-non-spin flip processes, which is a non-radiative Coulomb interaction induced decay. The states $|4\rangle$ and $|3\rangle$ are assumed to be decoupled.

The four key basis states are shown in Figure 5.3-1. As before, $|1\rangle$ and $|2\rangle$ are the macrospin ground states, while $|3\rangle$ and $|4\rangle$ are the excited states. It is useful to transform the matrix elements to the defined Bloch vectors for pairs of states. We introduce the polarization $\mathfrak{q}$ between the states $|1\rangle$ and $|4\rangle$, the polarization $\mathfrak{b}$ for the fast decay channel between the states $|4\rangle$ and $|1\rangle$, and the polarization $\mathfrak{r}$ between the excited states $|3\rangle$ and $|4\rangle$. Using this nomenclature, we can write the density matrix for the two Λ system as:

$$\hat{\rho} = \frac{1}{2}\begin{bmatrix} m_z + q_z & m_- & d_+ & q_- \\ m_+ & -(m_z + p_z) & p_+ & b_- \\ d_- & p_- & 1 + p_z & r_- \\ q_+ & b_+ & r_+ & 1 - q_z \end{bmatrix}. \tag{5.17}$$

The unit trace of the density matrix constrains the choice of the longitudinal component to three,

$$m_z = \hat{\rho}_{11} - \hat{\rho}_{22} - \hat{\rho}_{33} + \hat{\rho}_{44}\ , \tag{5.18}$$

$$p_z = -\hat{\rho}_{11} - \hat{\rho}_{22} + \hat{\rho}_{33} - \hat{\rho}_{44}\ , \tag{5.19}$$

$$q_z = \hat{\rho}_{11} + \hat{\rho}_{22} + \hat{\rho}_{33} - \hat{\rho}_{44}\ , \tag{5.20}$$

which, we refer to, respectively, as magnetization and optical polarizations for the convenience of computation and their correct limiting case behavior. The Hamiltonian $\widehat{\mathcal{H}}$ used in Eq. (5.5) is given by:

$$\widehat{\mathcal{H}} = \frac{1}{2}\begin{bmatrix} B_z & B_- & 0 & -i\frac{\Omega_{\sigma_-}}{2} \\ B_+ & -B_z & -i\frac{\Omega_{\sigma_+}}{2} & 0 \\ 0 & i\frac{\Omega_{\sigma_+}}{2} & \Delta_{23} - B_z & 0 \\ i\frac{\Omega_{\sigma_-}}{2} & 0 & 0 & \Delta_{14} + B_z \end{bmatrix} \tag{5.21}$$

where Δ_{41} is the detuning of the light frequency from the resonance frequency between states $|4\rangle$ and $|1\rangle$, and the optical excitation induced by the σ_- light is introduced via the Rabi frequency Ω_{σ_-}:

$$\Omega_{\sigma_-} = \frac{2\mu_{41}E^-}{\hbar} \tag{5.22}$$

where E^- is the amplitude of electric field related to the σ_- light, and $\mu_{41} = \mu_{32}$ is the electron transition dipole moment between state $|4\rangle$ and $|1\rangle$.

For simplicity and symmetry, the decay rate from the channel $|3\rangle \to |1\rangle$ and from the channel $|4\rangle \to |2\rangle$ are assumed to be identical so that we can assume $\Gamma_{l_{41}} = \Gamma_{l_{32}} = \Gamma_l$. Using a similar reasoning for the pure dephasing, we can obtain $\Gamma_{t_{\sigma_+}} = \Gamma_{t_{\sigma_-}} = \Gamma_t$.

When the density matrix is converted into fifteen components of the polarizations and magnetizations, we obtain a system of equation that describes the magnetization dynamic of the magnetic system excited by an elliptical polarized light source:

$$\frac{dm_x}{dt} = 2(B_y m_z - B_z m_y) + B_y(q_z + p_z) - \frac{1}{2}\left(\Omega_{\sigma_+} + \Omega_{\sigma_-}\right) d_x \ , \tag{5.23}$$

$$\frac{dm_y}{dt} = 2(B_z m_x - B_x m_z) - B_x(q_z + p_z) - \frac{1}{2}\left(\Omega_{\sigma_+} + \Omega_{\sigma-}\right) d_y \ , \tag{5.24}$$

$$\frac{dm_z}{dt} = 2(B_x m_y - B_y m_x) + \Gamma_l(q_z + p_z) \ , \tag{5.25}$$

$$\frac{dp_z}{dt} = \Omega_{\sigma_+} p_x - \Gamma_d(1 + p_z) \ , \tag{5.26}$$

$$\frac{dq_z}{dt} = -\Omega_{\sigma_-} q_x + \Gamma_d(1 - q_z) \ , \tag{5.27}$$

$$\frac{dp_x}{dt} = -\Delta_{23} p_y - \frac{\Omega_{\sigma_+}}{2}(2p_z + 1 + m_z) + (B_x d_y + B_y d_x) - \Gamma_t p_x \ , \tag{5.28}$$

$$\frac{dp_y}{dt} = \Delta_{32} p_x - (B_x d_x - B_y d_y) - \Gamma_t p_y \ , \tag{5.29}$$

$$\frac{dq_x}{dt} = -\Delta_{41} q_y + \frac{1}{2}\Omega_{\sigma_-}(2q_z - 1 + m_z) - (B_x b_y + B_y b_x) - \Gamma_t q_x \ , \tag{5.30}$$

$$\frac{dq_y}{dt} = \Delta_{41} q_x + (B_x b_x - B_y b_y) - \Gamma_t q_y \tag{5.31}$$

$$\frac{dd_x}{dt} = (2B_z - \Delta_{23})d_y + \frac{\Omega_{\sigma_+}}{2}m_x - \frac{\Omega_{\sigma_-}}{2}r_x - (B_x p_y - B_y p_x) - \Gamma_t d_x \ , \tag{5.32}$$

$$\frac{dd_y}{dt} = (\Delta_{23} - 2B_z)d_x - \frac{\Omega_{\sigma_+}}{2}m_y - \frac{\Omega_{\sigma_-}}{2}r_y - (B_x p_x + B_y p_y) - \Gamma_t d_y \ , \tag{5.33}$$

$$\frac{db_x}{dt} = (2B_z + \Delta_{41})b_y + \frac{\Omega_{\sigma_-}}{2}m_x - \frac{\Omega_{\sigma_+}}{2}r_x - (B_x q_y - B_y q_x) - \Gamma_t b_x \ , \tag{5.34}$$

$$\frac{db_y}{dt} = -(2B_z + \Delta_{41})b_x - \frac{\Omega_{\sigma_-}}{2}m_y - \frac{\Omega_{\sigma_+}}{2}r_y + (B_x q_x + B_y q_y) - \Gamma_t b_x \ , \tag{5.35}$$

$$\frac{dr_x}{dt} = \left(2Bz - \Delta 1 + \Delta 2\right)r_y + \frac{\Omega_{\sigma_+}}{2}b_x + \frac{\Omega_{\sigma_-}}{2}b_x + \Gamma_l r_x \ , \tag{5.36}$$

$$\frac{dr_y}{dt} = -\left(2Bz - \Delta 1 + \Delta 2\right)r_y + \frac{\Omega_{\sigma_+}}{2}b_y + \frac{\Omega_{\sigma_-}}{2}b_y + \Gamma_l r_y \ . \tag{5.37}$$

It can be shown that if $\Omega_{\sigma_+} \neq 0$ and $\Omega_{\sigma_-} = 0$, the system of Eq.(5.23)-(5.36) reduces to the model derived in Eq. (5.8)-(5.15) since the channels $\mathfrak{q}$, and $\mathfrak{b}$ are excited only if $\Omega_{\sigma_-} \neq 0$, and the channel $\mathfrak{r}$ is excited when both $\Omega_{\sigma_+} \neq 0$ and $\Omega_{\sigma-} \neq 0$. An estimate of the amplitude of the magnetic field E^+ and E^- for all polarization is given in Appendix C.

5.4 THE INCOHERENT REGIME

Let us consider the case in which magnetic system is excited by a σ_+ light source. The population is assumed to be initially in state $|2\rangle$ (i.e. $\hat{\rho} = 1$ or $p_z = -1$, and $m_z = -1$). Let us assume that the excitation provided by the laser is at the resonant frequency (i.e. $\Delta_{23} = 0$) and no external field is applied (i.e. $\mathbf{B} = 0$). For simplicity, we choose the pure dephasing

$\Gamma^* = \Gamma_l / 2$ such that $\Gamma_l = \Gamma_t = \Gamma$. Under these condition it is possible to rewrite the magnetization dynamic for the system as a function of the population p_z and m_z as:

$$\frac{dm_z}{dt} = \Gamma_l \left(1 + p_z\right) , \tag{5.38}$$

$$\frac{d^2 p_z}{dt^2} + 2\lambda\omega \frac{dp_z}{dt} + \omega^2 p_z = -\left(\frac{\Omega^2}{2} + \Gamma^2\right) - \frac{\Omega^2}{2} m_z \ . \tag{5.39}$$

The equation for the p_z given in Eq. (5.38) can be seen as the equation of a damped harmonic oscillator in which $\omega = \sqrt{\Omega^2 + \Gamma^2}$ is the natural frequency and $\lambda = \Gamma / \omega$ is the damping ratio, where the right hand side represent the force acting on the oscillator. The optical excitation induces oscillations of the population between state $|2\rangle$ and state $|3\rangle$. In the absence of a decay (i.e. $\Gamma = 0$), the population fluctuates between the ground state $|2\rangle$ and the excited state $|3\rangle$ without any change in the overall magnetization. When $\Gamma \neq 0$, a fraction of the population leaks from state $|3\rangle$ to state $|1\rangle$ emptying the population in state $|2\rangle$, inducing the magnetization reversal (Figure 5.4-1).

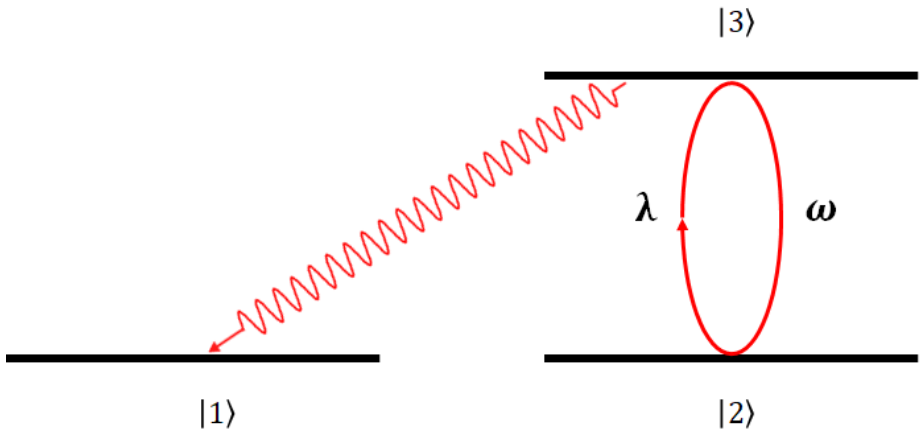

Figure 5-5: The optical excitation induces an harmonic oscillation with frequency ω between state $|2\rangle$ and $|3\rangle$. After every oscillation, a fraction of the population leaks from state $|3\rangle$ to state $|1\rangle$ due to the presence of the damping λ .

When the damping ratio $\lambda \ll 1$ (i.e. $\Omega \gg \Gamma$), the polarization population p_z behaves as an overdamped oscillator (Figure 5.4-2c) and magnetization reversal is characterized by a combination of a coherent magnon excitation, oscillating with frequency ω, and an incoherent magnon excitation driven by the decay rate (Figure 5.4-2a).

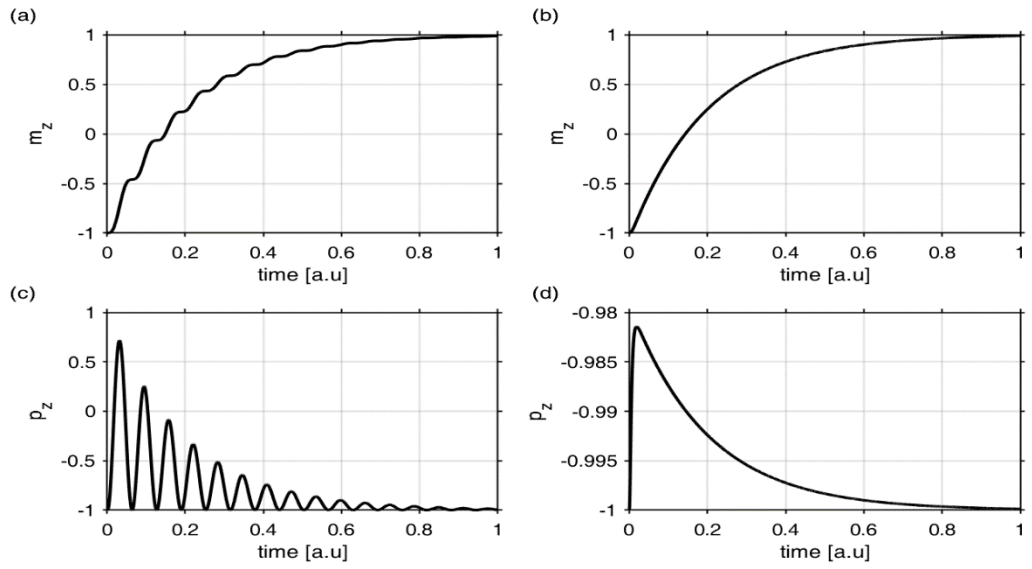

Figure 5-6: Dynamics of the magnetization and polarization population. The results are shown for (a, c) the coherent regime, $\Omega \gg \Gamma$, and (b, d) the incoherent regime, $\Omega \ll \Gamma$.

When the damping ratio $\lambda \gg 1$ (i.e. $\Omega \ll \Gamma$), the polarization population p_z behaves as an overdamped oscillator (Figure 5.4-2d) and no coherent magnon excitation is observed during the magnetization reversal (Figure 5.4-2b).This behavior can be explained with the rapid quenching of the rotation of the off-diagonal components in the density matrix given by Eq. (5.1) or by Eq. (5.17) by the decoherence Γ. When this happens, the contribution of the second derivative in Eq. (5.38) can neglected, and the magnetization reversal can expressed as an incoherent process driven by the effective pumping $G \sim \Omega^2 / \Gamma$.

In many practical case, the decay rate Γ_l and the dephasing Γ^* are much larger than both the Rabi frequency $\Omega_{\sigma_\pm}$ and applied field $\mathbf{B}$ (i.e. $\Gamma_l \geq \Gamma_t \gg \Omega_{\sigma_\pm}, \mathbf{B}$). In this case, the system is said to be in the incoherent regime.

In ferromagnetic materials, such as FePt and CoPt, the decay rate is estimate to be of the order of $\Gamma_d = 0.6 - 1.0\ \text{fs}$, based on the lifetime of the photoexcited electron in Fe [76]. The peak optical power used in the HD-AOS experiments is of the order of $P = 0.01 - 0.04\ \text{TW/cm}^2$, that leads to an electric field inside of the material on the order of $E = 1\times10^8 - 3\times10^8\ \text{V/m}$. If we assume a dipolar transition moment on the order on $\mu_{12} = \mu_{34} = 1\ e\text{Å}$, we obtain a Rabi frequency for the purely circular polarized light on the order of $\Omega_{\sigma_\pm} \approx 0.02 - 0.04\ \text{fs}^{-1}$. These values are consistent with those obtained from ab-initio computation [77]. It is then reasonable to assume for this kind of material that the optical transition happens in the incoherent regime.

Under the assumption of (i) incoherent regime and (ii) negligible detuning (i.e. $\Delta_{34}, \Delta_{12} \ll \Omega_{\sigma_\pm}$) it is possible to rewrite the magnetization dynamics equations produced by the optical excitation only as a function of the two polarization population p_z, q_z, and the magnetization vector $\mathbf{m}$. This allows us to obtain a system of 5N equation, slightly increasing the memory requirement of the system without increasing significantly the complexity of the problem.

If we ignore interactions between the magnetic field $\mathbf{B}$ and the off-diagonal components of the density matrix, we can use the operator method [78] to remove the explicit dependence of the coherence and write the magnetization dynamics as:

$$\frac{dm_x}{dt} = 2(B_y m_z - B_z m_y) + B_y(q_z + p_z) - \frac{\left(G_{t,\sigma_+} + G_{t,\sigma-}\right)}{2} m_x \ , \tag{5.40}$$

$$\frac{dm_y}{dt} = 2(B_z m_x - B_x m_z) - B_x(q_z + p_z) - \frac{\left(G_{t,\sigma_+} + G_{t,\sigma-}\right)}{2} m_y \ , \tag{5.41}$$

$$\frac{dm_z}{dt} = 2(B_x m_y - B_y m_x) + (p_z + q_z)\Gamma_l \ , \tag{5.42}$$

$$\frac{dp_z}{dt} = -\left(\Gamma_{inc} + \frac{G_{l,\sigma_+}}{2}\right)(1 + p_z) - \frac{G_{l,\sigma_+}}{2}(p_z + m_z) \ , \tag{5.43}$$

$$\frac{dq_z}{dt} = \left(\Gamma_{inc} + \frac{G_{l,\sigma_-}}{2}\right)(1 - p_z) - \frac{G_{l,\sigma_-}}{2}(q_z + m_z) \ , \tag{5.44}$$

where $\Gamma_{inc} = \Gamma_l \Gamma_t / (\Gamma_l + \Gamma_t)$ and the effective longitudinal pumping $G_{l,\sigma_{pm}}$ and the effective transverse pumping $G_{l,\sigma_\pm}$ are given by:

$$G_{l,\sigma_\pm} = \frac{{\Omega_{\sigma_\pm}}^2}{2\Gamma_t}, \qquad G_{t,\sigma_\pm} = \frac{{\Omega_{\sigma_\pm}}^2}{(\Gamma_l + \Gamma_t)} \ . \tag{5.45}$$

5.5 ANALYSIS OF THE OPTICAL EXCITATION

The system of equations given by Eq.(5.39)-(5.43) form the basis of the opto-magnetic model. The focus of this section is to estimate the efficiency of the optical excitation, and the error introduced by the incoherent regime approximation.

We consider the effect of a continuous optical excitation (i.e. $\Omega(t) = \Omega_0 \ \forall t \geq 0$) on an isotropic particle, when an external field B_z is applied. Assuming a constant value of the decay rate, it is useful to express the results as a function of the normalized time t' :

$$t' = t\Gamma_l \ . \tag{5.46}$$

In a similar fashion, we introduced the normalized optical and magnetic components:

$$\begin{gathered} B'_z = B_z / \Gamma_l, \quad \Omega'_{\sigma_\pm} = \Omega_{\sigma_\pm} / \Gamma_l, \quad \Gamma'_t = \Gamma_t / \Gamma_l, \\ G'_{l,\sigma_\pm} = G_{l,\sigma_\pm} / \Gamma_l, \quad G'_{t,\sigma_\pm} = G_{t,\sigma_\pm} / \Gamma_l, \quad \Gamma'_{inc} = \Gamma_{inc} / \Gamma_l, \end{gathered} \ . \tag{5.47}$$

Using the normalized unit, it is possible to define the reversal rate $\gamma_t = 1/t'_{rev}$ as the inverse of the reversal time t'_{rev}. The reversal time is chosen as the time at which the magnetic particle can be considered in the final state for the different polarization of the light:

$$m_z(t'_{rev}) = \begin{cases} +0.75 & \text{for } \sigma_+ \\ -0.75 & \text{for } \sigma_- \\ \pm 0.01 & \text{for } \pi \end{cases}. \tag{5.48}$$

The linear polarization π is obtained when $\Omega_{\sigma_+} = \Omega_{\sigma_=} \neq 0$. In this case, the contribution of the two optical excitation are compensated, leading to the same population in the two ground states $\rho_{11} = \rho_{22}$ (i.e. $m_z = 0$ and $p_z = -q_z$). Thus, for linear polarized light, the optical excitation generates an ultrafast optical that can be explained by a Stoner excitation process [79] .

The error introduced by the incoherent regime approximation is defined as a function of the reversal rate:

$$\text{Error} = \frac{\left|\gamma_{rev,0} - \gamma_{rev,1}\right|}{\gamma_{rev,0}}, \tag{5.49}$$

where $\gamma_{rev,0}$ is the reversal rate obtained solving the exact model, and $\gamma_{rev,1}$ is the reversal rate obtained solving the incoherent approximation. In this analysis we considered two cases of interest:

1) The case where the magnetization is parallel to the direction of propagation of the light.

2) The case where the magnetization is at an angle θ with the direction of propagation of the light.

The first case serves as a testbed of the magnetization reversal induced by an elliptical polarized source. The second is used to study the optical damping effect introduced by the exchange of momentum between the light and media. The analysis is focused on the realistic range of values for the optical excitation. Given the range fluency used in the HD-AOS experiments and the decay rate for FePt and CoPt, we focus our analysis to the range of optical excitation $0.01 \le \Omega_{\sigma\pm} \le 1$ and for a transverse decay rate $1/2 \le \Gamma_t \le 1$.

A Magnetization parallel to the light propagation direction

We first consider the case where the magnetization and the field are parallel to the direction of light propagation, assumed in the z-direction:

$$m_z(0) = \begin{cases} -1 & \text{for } \sigma_+ \\ +1 & \text{for } \sigma_- \\ \pm 1 & \text{for } \pi \end{cases} . \qquad (5.50)$$

Given the initial condition for the magnetization, the only channels that are activated in the model are the populations m_z , p_z and q_z, and the coherence channels p_x and q_x. The incoherent regime can be written as:

$$\frac{dm_z}{dt'} = (q_z + p_z) , \qquad (5.51)$$

$$\frac{dp_z}{dt'} = -\left(\Gamma'_{inc} + \frac{G'_{l,\sigma_+}}{2} \right)(1 + p_z) - \frac{G'_{l,\sigma_+}}{2}(p_z + m_z) , \qquad (5.52)$$

$$\frac{dq_z}{dt'} = \left(\Gamma'_{inc} + \frac{G'_{l,\sigma_-}}{2} \right)(1 - q_z) - \frac{G'_{l,\sigma_-}}{2}(q_z + m_z) . \qquad (5.53)$$

In the case $\Gamma_l = \Gamma_t$, the incoherent decay rate is $\Gamma'_{inc} = 1/2$ and the system of Eq. (5.50) -(5.52) has a simple analytical solution for the magnetization of a purely circular polarized source:

$$m_{z,\sigma_\pm}(t') = \pm 1 \mp 2\frac{\left(e^{-G'_{\sigma_\pm} t'} - 2G_{\sigma_\pm} e^{-t'/2}\right)}{1 - 2G'_{\sigma_\pm}} \approx \pm 1 \mp 2e^{-G'_{\sigma_\pm} t'} \quad . \tag{5.54}$$

The last approximation is obtained under the assumption of $G_{l,\sigma_\pm} \ll 1$, valid in the incoherent regime. When the initial magnetization is parallel to the direction of the light propagation, the magnetization is reversed through a purely longitudinal magnetization reversal, where the speed of the reversal is defined by the effective optical pumping. Since the field B_z only affects the precessional motion of the magnetization, in the absence of a longitudinal damping, the magnetization dynamics is unaffected by the presence of the field. Thus, the magnetization dynamics is a function of only the Raby frequency and dephasing.

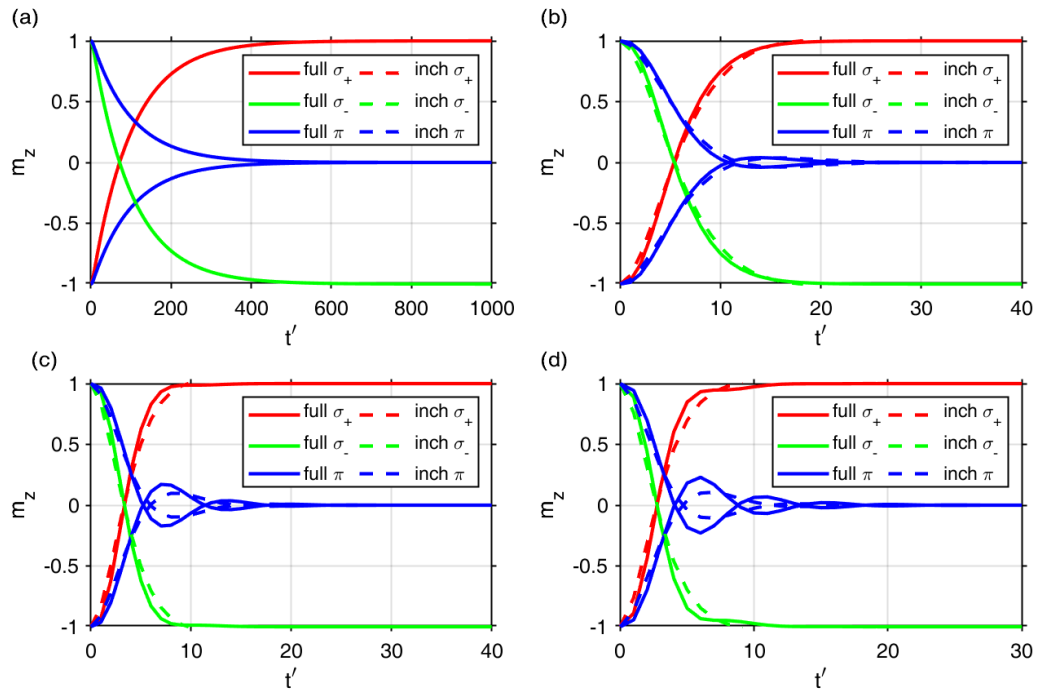

Figure 5-7: Magnetization dynamics induced by a σ_+ (red lines), σ_- (green lines), and π (blue lines) polarized light source, for the two Λ model (solid lines) and the incoherent regime approximation (dashed lines).The results are shown for (a) $\Omega' = 0.1$, (b) $\Omega' = 0.5$, (c) $\Omega' = 0.8$, and (d) $\Omega' = 1.0$. The transverse decay rate is $\Gamma'_t = 1/2$.

For values of $\Omega' < 0.1$, the difference in the magnetization reversal between the full model and the incoherent regime approximation are negligible (Figure 5.5-1). Small difference starts to appear for values of $\Omega' \sim 0.5$ (Figure 5.5-1). For $\Omega'_{\sigma_\pm} \geq 0.8$, the coherent excitation cannot be neglected anymore, and the incoherent excitation approximation in not able to describe correctly the dynamics of the system (Figure 5.5-1c,d).

For a given longitudinal decay rate Γ_l, the reversal rate γ_{rev} is proportional to the $\Omega_{\sigma_\pm}$ and inversely proportional to Γ_t (Figure 5.5-2a,b). Remembering the definition of $\Omega_{\sigma_\pm}$ given in Eq. (5.7), it is logical to assume that stronger absorption would lead to larger Ω and a

faster reversal, since the magnitude of the electric field is proportional to the square root of the optical intensity absorbed by the media $\Omega_{\sigma_\pm} \sim \sqrt{I_0}$. However, a stronger absorption in metals also means higher temperature and higher decay rate Γ_t . The higher temperature introduces an addition source of decoherence in the system through thermal fluctuations, reducing the effectiveness of the optical pumping and introducing a secondary demagnetization when the optical excitation is removed that counter the contribution of the optical excitation.

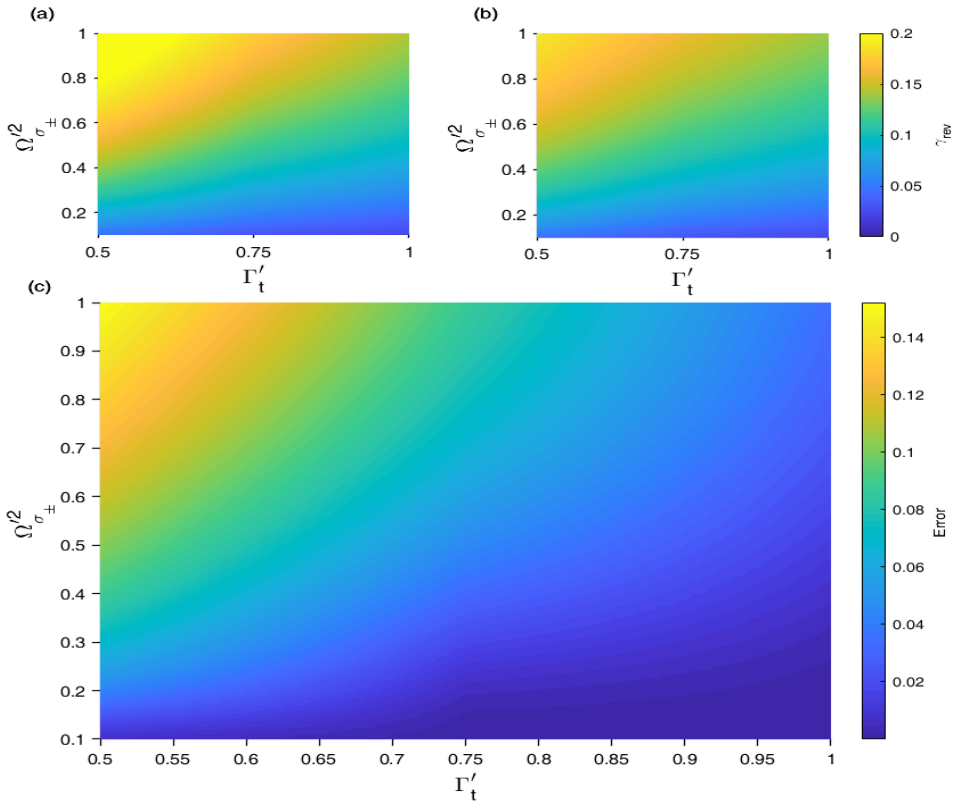

Figure 5-8: Reversal rate as a function of the Rabi frequency and the transverse decay rate for (a) the two Λ model and (b) the incoherent regime approximation. (c) Shows the error introduced by the incoherent regime approximation

In the absence of pure decoherence (i.e. $\Gamma'_t = 1/2$), the incoherent regime approximation leads to accurate results for $\Omega'_{\sigma_\pm} \leq 0.3$ (Figure 5.5-2c). The introduction of decoherence can extend the range of validity of the approximation. The result is expected since

any source of decoherence, being the dephasing, the detuning, or the temperature fluctuation, would rapidly quench any coherent oscillation of the coherence channel.

B Magnetization at angle θ with respect to the light propagation

If the initial magnetization is non-parallel to the direction of the light propagation, the system is subject to a precession effect due to the presence of the external field B_z and to a damping effect due to the momentum exchange between the photons and the spins. In the incoherent regime approximation, we neglect the effect of the field on the coherence channels $p_{\pm}$, $d_{\pm}$, $b_{\pm}$, and $r_{\pm}$. This assumption is valid for an applied field on the order of several Tesla ($B_z \ll \Gamma_l$), which is usually the case in experiments.

In the absence of an external field, the incoherent approximation has a simple analytical solution for the purely circular polarization light $\sigma_{\pm}$ when $\Gamma_t = \Gamma_l$ and $G_{l,\sigma_{\pm}} = G_{t,\sigma_{\pm}} = G_{\sigma_{\pm}}$. Considering an initial magnetization $\mathbf{m}_{\sigma_{\pm}} = \{\sin(\theta), 0, \mp\cos(\theta)\}$, the solution for the magnetization is given by:

$$m_{z,\sigma_{\pm}} \approx \pm 1 \mp \left(1 + \cos(\theta)\right) \mathrm{e}^{-G'_{\sigma_{\pm}} t'} , \tag{5.55}$$

$$m_{x,\sigma_{\pm}} = \sin(\theta) \mathrm{e}^{-G'_{\sigma_{\pm}} t'/2} . \tag{5.56}$$

Solving numerically for θ it is possible to cast the result as a function of the polar angle $\theta_{\sigma_{\pm}}$ in time. It is possible to define the optical pumping induced by the optical excitation as:

$$\theta_{\sigma_{\pm}}(t) = \operatorname{acos}\left(\frac{m_{z,\sigma_{\pm}}(t)}{\sqrt{m^2_{z,\sigma_{\pm}}(t) + m^2_{x,\sigma_{\pm}}(t)}} \right) . \tag{5.57}$$

Using the analytical solution for the magnetization given by Eq. (5.54)-(5.55) in Eq. (5.56) we can obtain the optical damping related angle $\theta_{\sigma_\pm}$ induced by the circular polarized light (Figure 5.5-3). For a σ_+ light, if the magnetization is $m_z < 0$ (i.e. $\theta \le \pi/2$), the optical excitation acts as an anti-damping, pushing the magnetization in plane; if the magnetization is $m_z > 0$ (i.e. $\theta > \pi/2$), the optical excitation acts as an effective damping pushing the magnetization in the final direction of the magnetization.

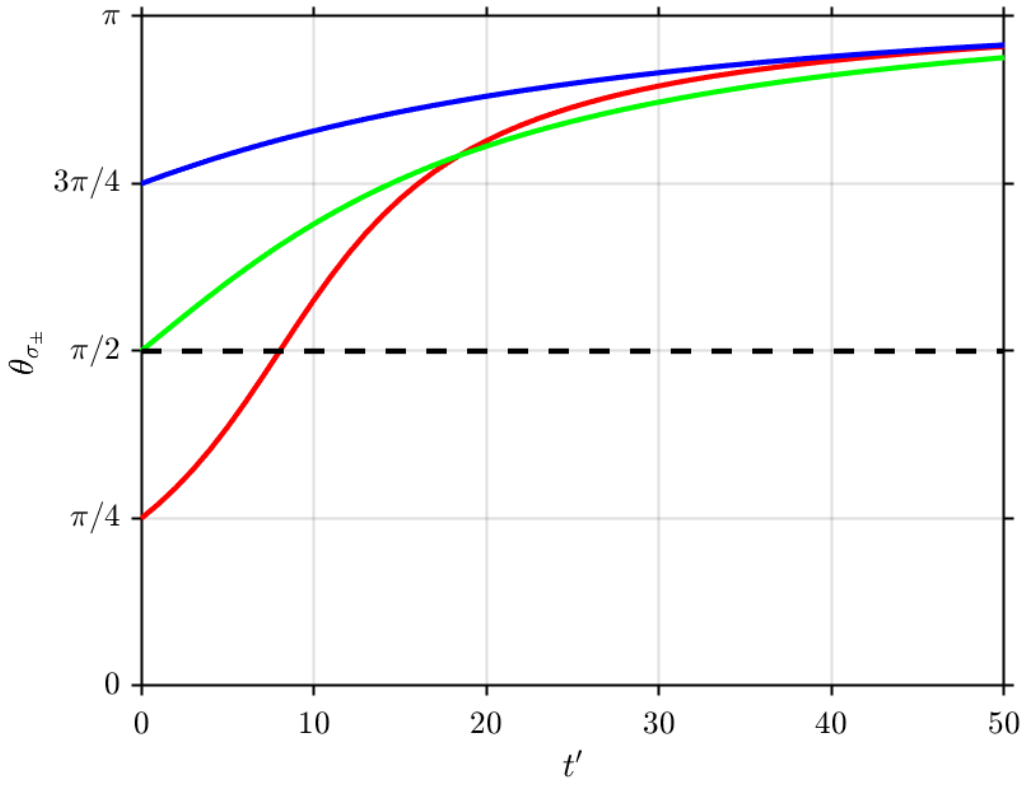

Figure 5-9: Dynamics of the optical damping $\theta_{\sigma_\pm}$ for an initial polar angle of $\theta = \pi/4$ (red line), $\theta = \pi/2$ (green line), and $\theta = 3\pi/4$ (blue line). The black dashed line represents the point at which the magnetization is reversed, if the initial magnetization is $m_z < 0$ for σ_+ or $m_z > 0$ for σ_-.

The damping/anti-damping effect explains the displacement of the domain wall. Let us consider a magnetic film with out-of-plane anisotropy. An optical excitation σ_+, tends to increase the magnetization with $m_z > 0$ aligning in the direction of the easy axis (optical damping). At the same time, the optical excitation tries pushing the magnetization with $m_z < 0$ reducing their overall magnetization (optical anti-damping). The overall contribution of the damping/anti-damping effect expands the domain "up" and contracts the domain "down", resulting in an effecting optical displacement of the domain wall (Figure 5.5-4).

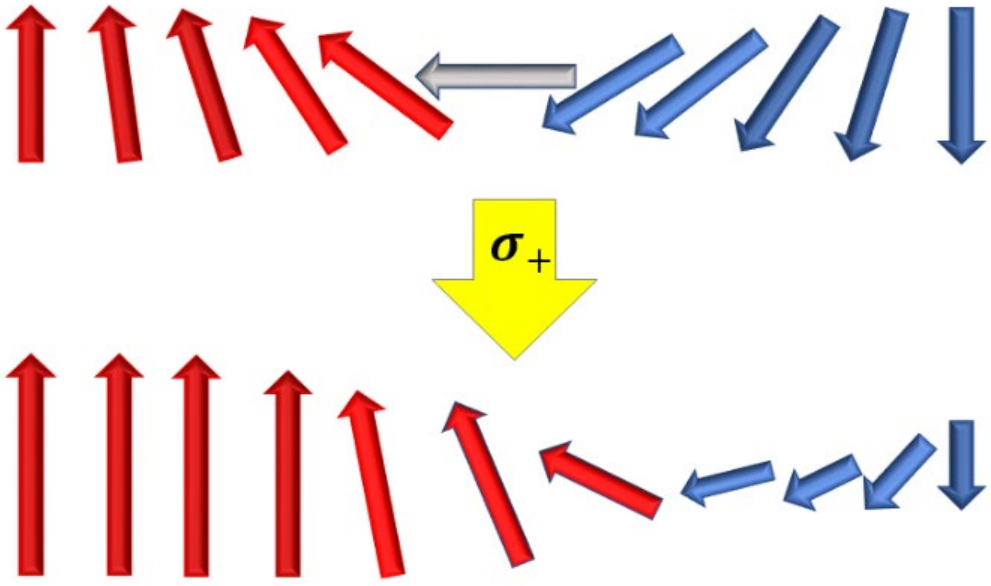

Figure 5-10: Domain wall displacement induced by a circularly polarized excitation σ_+ .

As in the case win which the magnetization is parallel to the direction of propagation of the light, the reversal rate γ_{rev} is proportional to the $\Omega_{\sigma_\pm}$ and inversely proportional to Γ_t. In the absence of an external applied field, the error introduced by the incoherent regime approximation when the magnetization is at an angle θ with respect to the direction of the light

propagation is the same observed for the magnetization parallel to the light propagation (Figure 5.5-5a). The presence of the precessional effect driven by the external field B_z, does not modify the accuracy of the incoherent regime approximation (Figure 5.5-5).

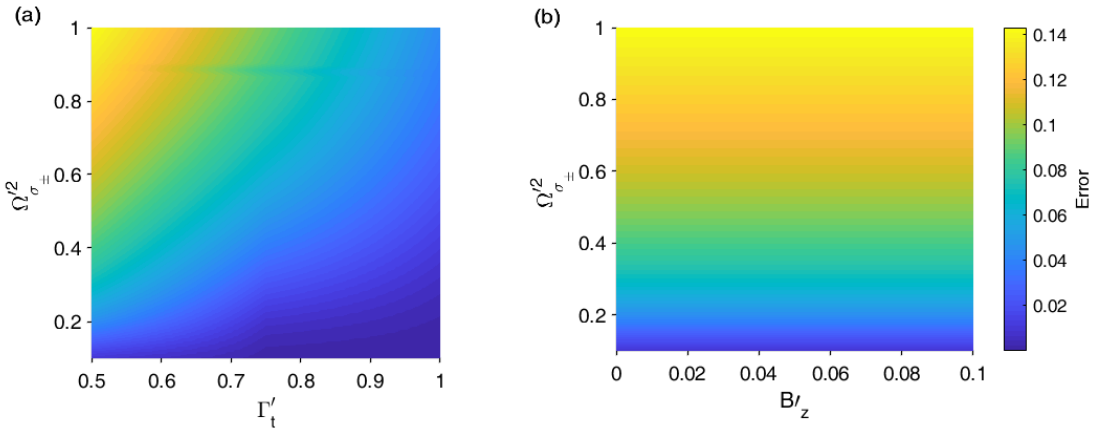

Figure 5-11: Error introduced by the Incoherent regime approximation for an initial angle of the magnetization $\theta = \pi / 4$ (a) as a function of Γ'_t and $\Omega'_{\sigma_\pm}$ for $B'_z = 0$, and (b) as a function of B'_z and $\Omega'_{\sigma_\pm}$ for $\Gamma'_t = 1/2$.

The results show that in the range of optical excitation and applied fields realistically used in the HD-AOS and in the HD-DWD, it is possible to describe correctly the magnetization dynamics using the incoherent regime approximation.

ACKNOWLEDGEMENT

This chapter, in part, is currently being prepared for submission for publication of the material. M. Menarini, V. Lomakin and L. J. Sham "A Theory of Optoelectronic Reversal of Ferromagnetic Magnetization". The dissertation author was the primary investigator and author of the text used in this chapter.

CHAPTER 6 - MODELLING OF OPTICAL PHENOMENA IN FERROMAGNETIC THIN FILM

In this chapter, we present an analysis of the optical excitation of ferromagnetic thin film excited by elliptical polarized laser source. We first introduce the equation of motion for ferromagnetic material augmented by the relaxation coefficients and the thermal fluctuations acting on the magnetization sector. The model is then used to study the opto-magnetic excitation induced by a series of sub-picosecond laser pulses on a thin FePt film.

6.1 LANDAU-LIFSHITZ-LAMBDA MODEL

Using the incoherent regime approximation derived in the previous chapter, it is possible to derive a system of equation that combines the optical excitation with the magnetization dynamics driven by the effective field H_{eff} and the molecular field H_E. Given the different timescale of the optical excitation and the magnetic relaxation, it is possible to introduce the damping in the two Λ system by adding the longitudinal and perpendicular damping to the equation as a phenomenological effect. The thermal fluctuations are assumed to interact only with the coupled ground state $|1\rangle$ and $|2\rangle$, leading to the same thermal fluctuation derived for the LLB model. The magnetization dynamics can then be described as:

$$\begin{aligned}\frac{dm_x}{dt} = {} & \gamma\left[\mathbf{m}\times\mathbf{H}_{eff}\right]_x - \frac{\gamma\alpha_\perp}{m^2}\left[\mathbf{m}\times\left(\mathbf{m}\times\left(\mathbf{H}_{eff}+\boldsymbol{\zeta}_\perp\right)\right)\right]_x - \gamma\alpha_{||}\left(\frac{1-B_S/m}{\mu_0\beta B'_S}-\frac{\mathbf{m}\cdot\boldsymbol{\zeta}_{||}}{m^2}\right)m_x \\ & + \frac{\gamma}{2}H_{eff,y}(q_z+p_z) - \frac{\left(G_{t,\sigma_+}+G_{t,\sigma_-}\right)}{2}m_x\end{aligned}, \tag{6.1}$$

$$\frac{dm_y}{dt} = \gamma\left[\mathbf{m}\times\mathbf{H}_{eff}\right]_y - \frac{\gamma\alpha_\perp}{m^2}\left[\mathbf{m}\times\left(\mathbf{m}\times\left(\mathbf{H}_{eff}+\boldsymbol{\zeta}_\perp\right)\right)\right]_y - \gamma\alpha_{\|}\left(\frac{1-B_S/m}{\mu_0\beta B'_S} - \frac{\mathbf{m}\cdot\boldsymbol{\zeta}_{\|}}{m^2}\right)m_y$$
$$-\frac{\gamma}{2}H_{eff,x}(q_z+p_z) - \frac{\left(G_{t,\sigma_+}+G_{t,\sigma_-}\right)}{2}m_y \quad , \tag{6.2}$$

$$\frac{dm_z}{dt} = \gamma\left[\mathbf{m}\times\mathbf{H}_{eff}\right]_z - \frac{\gamma\alpha_\perp}{m^2}\left[\mathbf{m}\times\left(\mathbf{m}\times\left(\mathbf{H}_{eff}+\boldsymbol{\zeta}_\perp\right)\right)\right]_z - \gamma\alpha_{\|}\left(\frac{1-B_S/m}{\mu_0\beta B'_S} - \frac{\mathbf{m}\cdot\boldsymbol{\zeta}_{\|}}{m^2}\right)m_z \quad , \tag{6.3}$$
$$+\Gamma_l(q_z+p_z)$$

$$\frac{dp_z}{dt} = -\left(\Gamma_{inc}+\frac{G_{l,\sigma_+}}{2}\right)(1+p_z) - \frac{G_{l,\sigma_+}}{2}(p_z+m_z), \tag{6.4}$$

$$\frac{dq_z}{dt} = \left(\Gamma_{inc}+\frac{G_{l,\sigma_-}}{2}\right)(1-p_z) - \frac{G_{l,\sigma_-}}{2}(q_z+m_z) \ . \tag{6.5}$$

The model for the magnetization dynamics described by the incoherent approximation of the two Λ system and augmented by the Bloch dissipative terms given by Eq. (6.1)-(6.5) is called Landau-Lifshitz-Lambda (LLL) model. When the system is not excited by a circular polarized laser and after enough time has passed to observe a complete relaxation of the polarization and fast decay channels (i.e. $p_z = -1$ and $q_z = 1$) , it is easy to show that the LLL formulation reduced to the classical LLB formulation [5]. The speed of the relaxation from the excited state to the ground state is governed by the decay rate, which was assumed to be $\Gamma_d = 0.6\ \text{rad/fs}$. The choice of the decay rate is dictated by experimental observations. A higher value of Γ_d, up to $1\ \text{rad/fs}$, has not shown any significant difference in the numerical simulations. Smaller values of Γ_d would lead to accumulation of spins in the $|3\rangle$ state and a delayed re-magnetization that has not been observed experimentally.

In the simulations, the decay rate is assumed to be constant during the entire duration of the optical excitation, while the effective pumping coefficients are assumed to be a function of

the instantaneous optical intensity absorbed by the laser (i.e. $G \sim I(t)/I_0$ where I_0 is the peak absorbed intensity).

6.2 MODELING OF FEPT FILMS

To test the LLL model for a realistic case, we consider a continuous FePt film excited by a series of 100 helicity polarized sub-picosecond laser pulses ($\tau_{pulse} = 50$ fs) with a repetition rate of ~ 1 kHz.

The laser is modelled as combination of an optical source through the Rabi frequency, and a thermal pulse modeled through the 2TM described in Sec.3.4. Both the optical and the thermal source acting on the i-th cell is modeled by the laser intensity absorbed inside the material:

$$I_i(\mathbf{r}_i, z_{1,i}, z_{2,i}, t) = \epsilon_i(z_{1,i}, z_{2,i}) I_0 \exp\left[-\frac{x_i^2 + y_i^2}{w_0^2} - 2.77\left(\frac{t - 2\tau_{pulse}}{\tau_{pulse}} \right) \right], \tag{6.6}$$

where $I_0 = 0.94F_0/\tau_{pulse}$ is the peak Intensity of the laser, $\mathbf{r}_i = \{x_i, y_i\}$ is the position of the center of mass of the i-th cell on the xy-plane, and ϵ_i is the average intensity absorbed by the cell:

$$\epsilon_i(z_{1,i}, z_{2,i}) = \frac{1-R}{V_i}\left[\exp\left(-\frac{z_{1,i}}{\delta} \right) - \exp\left(-\frac{z_{2,i}}{\delta} \right) \right] \frac{\delta}{d_i} \ . \tag{6.7}$$

Here, R is the reflectivity of the material, δ is the optical penetration length, $z_{1,i}$ and $z_{2,i}$ are the top and bottom vertical coordinates of the cell, and the height of the cell is given by $d_i = z_{2,i} - z_{1,i}$. The z-axis is oriented in the direction of the light propagation (i.e. $z_{1,i} \le z_{2,i}$),

where the origin $z = 0$ is set at the interface between the laser and the film (Figure 6-1a). The position of the center of mass $\mathbf{r}_i$ is given with respect to the center of the laser pulse, where the absorbed optical intensity I is at its maximum (Figure 6-1b).

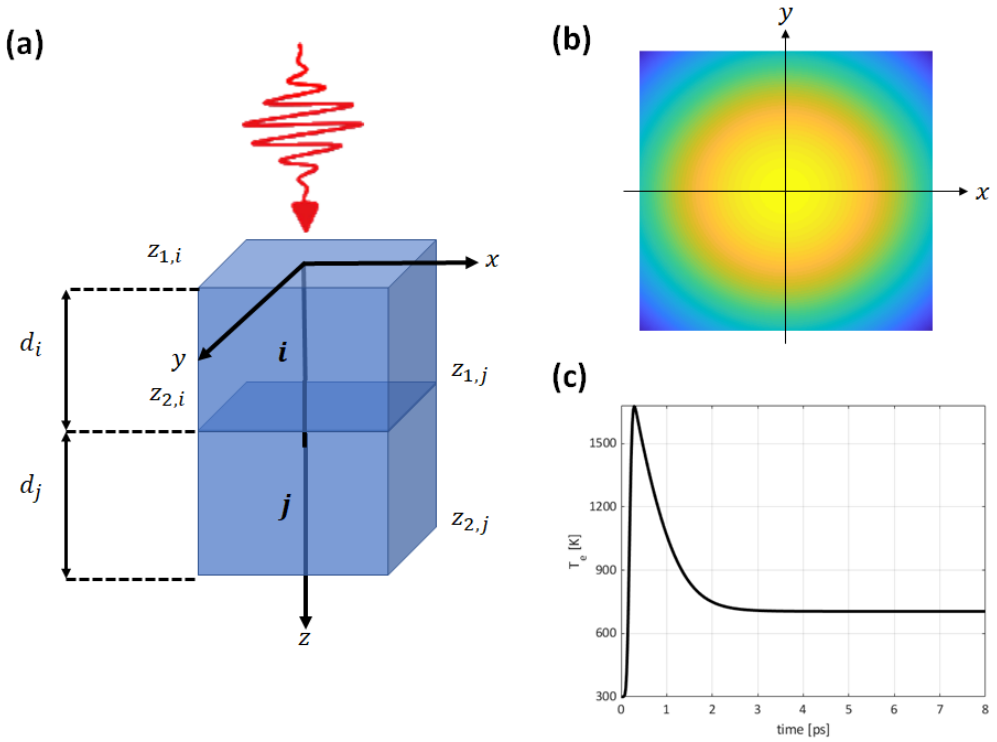

Figure 6-1: Modeling of the thermo-optical pulse. (a) Vertical discretization of the elements excited by an optical pulse. (b) Spatial profile of the absorbed laser intensity and (c) temperature dynamics induced at the center of an FePt film for a peak intensity of $I_0 = 0.8\ \mathrm{TW/cm^2}$ and an average absorbed intensity $\epsilon = 6\%$.

The temperature dynamics induced by the absorbed laser intensity I is precomputed at the beginning of the simulation (Figure 6-1c) using the 2TM introduced in Sec.3.4 and the thermal parameters used in computing the temperature dynamics are given by fitting the experimental results given in Ref. [33] with the thermal properties of typical non-noble transition metals thin films [80,81]. The thermal parameters used in the simulations are given in Table 6-I.

Table 6-I: Thermal parameters used in the simulations of FePt.

Parameter	Value	Unit	Description
γ_e	750	$Jm^{-3}K^{-2}$	Atomistic damping coefficient
C_{ph}	2.6×10^{6}	$Jm^{-3}K$	Specific heat of the lattice
$G_{e\text{-}ph}$	11×10^{17}	$Wm^{-3}K^{-1}$	Coupling constant between baths
K_{e0}	73	$Wm^{-1}K^{-1}$	Thermal conductivity at T_{amb}
τ_{pulse}	50	fs	Curie Temperature
δ	24.5	nm	Optical penetration length
η	3.2	fs^{-1}	Index of refraction
k	2.6	fs^{-1}	Extinction index
T_{amb}	300	K	Room temperature

After the laser excitation is removed, the electron bath reaches the equilibrium with the phonon bath in few picoseconds. This fast-thermal relaxation is followed by a secondary one that is dominated by the conduction in the phonon bath, that brings the system down to room temperature in $\Delta \sim 50$ ns. Given the magnetic relaxation time for FePt at room temperature and the repetition rate of the laser, it is reasonable to assume that the system has time to relax completely and that no accumulation of heat is present between pulses. Thus, the temperature profile precomputed at the beginning of the simulation is used as an input for the LLL model for all pulses.

For temperatures $T_1 \leq 0.8T_C$, no significant changes in the magnetization are observed for an FePt in the microsecond timescale. For the largest value of the peak intensity I_0 used in the current work, the blocking temperature T_1 is reached at the center of the laser beam after ~ 1 ns. After each pulse, the dynamics of the magnetization is let to evolve for 2 ns to account for the relaxation of the system. The system is then forced to relax to room temperature to eliminate any thermal accumulation effect, and the next pulse is applied.

A Helicity Dependent All Optical Switching

Let us consider a continuous square $1.2\ \mu\text{m} \times 1.2\ \mu\text{m}$ FePt film and $6\ \text{nm}$ thickness. The film is initially saturated along the negative z direction. A laser with a beam radius of $w_0 = 2.5\ \mu\text{m}$ is focused at the center of the film. The laser has a peak fluence of $F_0 = 45\ \text{mJ/cm}^2$. The peak fluence F_0 is chosen such that the temperature at the center of the beam is above T_C when the electron bath relaxes to the value of the phonon bath. This guarantees that any magnetization changes induced by the optical excitation are negated by the thermal demagnetization during cooldown. Thus, at the center of the beam, only thermal demagnetization is observed.

Table 6-II: Magnetic parameters used in simulation of FePt film.

Parameter	Value	Unit	Description	Source
λ	0.01		Atomistic damping coefficient	Ref. [33]
μ_0	3.24	μ_B	Magnetic moment for FePt	Ref. [51]
A_{ex}^0	2.2×10^{-6}	emu/cm	Exchange constant at $T = 0$ K	Ref. [33]
H_K^0	20	kOe	Anisotropy field at $T = 0$ K	Ref. [33]
T_C	700	K	Curie Temperature	Ref. [51]
S	3/2		Effective spin number	Ref.[82]
Γ_l	0.6	fs^{-1}	Optical longitudinal decay rate	Ref.[76]
Γ_t	0.6	fs^{-1}	Optical transverse decay rate	Ref.[76]
μ_e	0.7	eÅ	Transition dipole moment	

The system is discretized over identical strongly coupled cubic cells of length $\Delta = 6\ \text{nm}$. Hence, the three-dimensional system is reduced to a two-dimensional (2D) problem. Since the effective thickness of the film $d = 6\ \text{nm}$ is much smaller than the optical penetration length

$\delta = 24.5\ \text{nm}$, the average intensity ϵ_i absorbed by each cell can be obtained by using the transmission line model for a film on a substrate [83]. Let us consider the thin film deposited on a dielectric substrate and in contact with air (Figure 6-2a). The optical power absorbed can be obtained by modeling the film as a shunt impedance in a transmission line model with impedance given by the surface impedance

$$Z_S = \frac{Z_0}{\mathrm{i}k_0(\varepsilon - 1)d}\ , \tag{6.8}$$

where $Z_0 = 120\pi\ \Omega$ is the impedance of free space $k_0 = 2\pi / \lambda_{\text{photon}}$ is the wavenumber with $\lambda_{\text{photon}} = 800\ \text{nm}$ is the wavelength of the photons, and $\varepsilon = n - \mathrm{i}k$ is the complex refractive index. By solving for the transmission line model in Figure 6-2b, it is possible to estimate the fraction of optical power absorbed in the thin film as:

$$\epsilon_i = \frac{Z_0 V^2}{|Z_S|}\cos(\varphi) \qquad V = 1 + \frac{Z_{\text{in}} - Z_0}{Z_{\text{n}} + Z_0} \qquad Z_{\text{in}}^{-1} = Z_S^{-1} + Z_1^{-1}\ , \tag{6.9}$$

where Z_{in} is the input impedance and V is the voltage the entrance of the transmission line, and φ is the phase of Z_S. Assuming an index of refraction $n_1 = 3$ for the dielectric substrate, the average intensity absorbed into the film is $\epsilon_i = 6\%$.

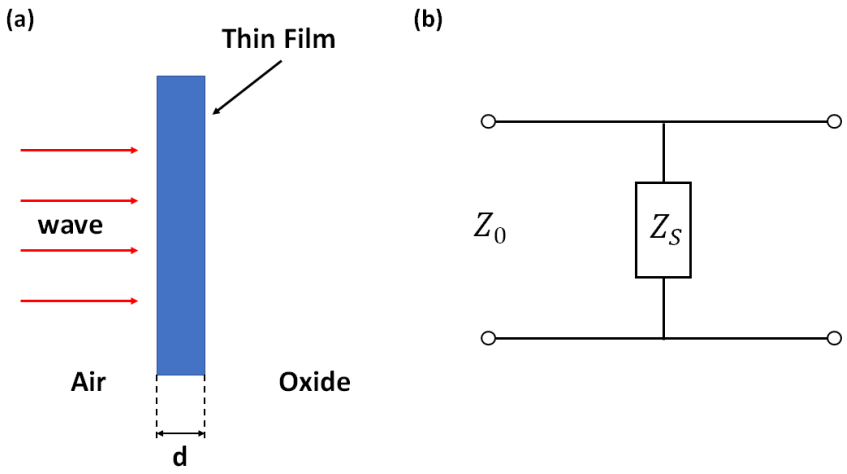

Figure 6-2: Schematic view of the thin film deposited on a dielectric substrate: (a) Geometry and (b) equivalent transmission line circuit.

The magnetic parameters used in the simulations are summarized in Table 6-II. The exchange constant $A_{ex}(T)$ and the anisotropy field coefficient $H_K(T)$ scale with the temperature as $A_{ex}(T) = A_{ex}^0 m_e(T)^{1.76}$ and $H_K(T) = H_K^0 m_e(T)^{0.1}$, respectively.

Let us considered the case of purely circularly polarized light σ_+ (i.e. $\Omega_{\sigma_+} = \Omega_0$ and $\Omega_{\sigma_-} = 0$) and of a purely linearly polarized light π (i.e. $\Omega_{\sigma_+} = \Omega_{\sigma_-} = \Omega_0 / \sqrt{2}$). After several pulses, it is possible to distinguish three different regions inside the film (Figure 6-3): region (1) where no change of magnetization is observed, region (2) where an effective magnetization reversal is observed only for the σ_+ polarization, and region (3) where the material is completely demagnetized. The observed optical reversal is cumulative effect that happens over the course of a set of sub-picosecond optical excitations, and its efficiency is a function of the local peak intensity $I(r) = I_0 \exp\left[-\left(r / w_0\right)^2\right]$. We define the local peak intensity absorbed at

the boundary between region (1) and region (2) as I_1 , and the local intensity absorbed at the boundary between region (2) and region (3) as I_2.

In region (1), $I(r) \leq I_1$, the intensity of the light, is below the threshold required to nucleate a domain or to displace the domain nucleated in a neighbor region within the duration of the pulse.

In region (3), $I(r) \geq I_2$, and the electron bath relaxes to the value of the phonon bath at a temperature close or above T_C. Since the secondary thermal relaxation of the phonon is order of magnitude slower than the electronic relaxation, the system is subjected to an extended thermal demagnetization that negates the effect of the optical contribution.

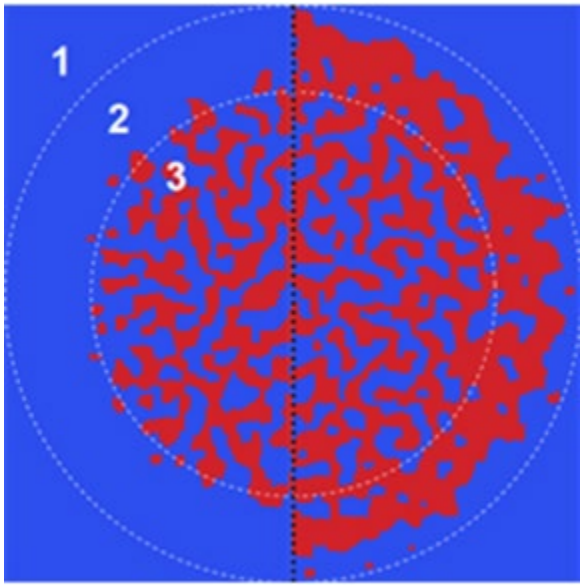

Figure 6-3: Effect of the laser beam on a saturated film in the "down" direction. On the left side the laser pulse is linearly polarized (π), on the right side it is circularly polarized σ_+.

In region (2), $I_1 \le I(r) \le I_2$, and different behavior can be observed for the σ_+ and π polarized light. To study the behavior of the optical excitation in this region, let up define two parameters:

- $n_\uparrow(I(\mathbf{r}))$ is the probability of nucleating a domain with magnetization up during a single pulse with local optical intensity $I(\mathbf{r})$.
- $n_\downarrow(I(\mathbf{r}))$ is the probability of nucleating a domain with magnetization down during a single pulse with local optical intensity $I(\mathbf{r})$.

For the π light, random nucleation is present in observed at the interface between region (2) and region (3). The equal contribution of σ_+ and σ_- leads to an optically driven demagnetization of the film as discussed in Sec. 5.5A. Thus, the probability of nucleating a domain in the up or down direction is identical in this region ($n_\uparrow = n_\downarrow$).

For the σ_+ light, the contribution of σ_+ near the interface between region (2) and (3) leads to an optically induced reduction of the saturation magnetization $M_{S_\downarrow}(T)$ for domains in the "down" direction, and an increment of the saturation magnetization $M_{S_\uparrow}(T)$ for domains in the "up" direction with respect to the expected saturation magnetization in the absence of optical excitation $M_S(T)$, as discussed in Sec. 5.5. During the cool down, the difference is magnetization between the two domains leads to different stability against the thermally induced reversal during cooldown.

Hence, the domain "up" nucleated during the previous pulses ($M_{S_\uparrow} > M_S$) are made more stable by the optical excitation with respect to the domains with magnetization down (

$M_{S_\downarrow} < M_S$), leading to a higher probability to nucleate domain "up" (i.e. $n_\uparrow > n_\downarrow$) after each pulse, leading to an effective magnetization reversal [49].

Moreover, in continuous films, the σ_+ optical excitation is able to produce a helicity-dependent reversal towards the down state [58]. This secondary mechanism increases the dimension of the "up" states domains and merges them together, creating a continuous switching ring after several pulses at the interface between region (1) and (2). The presence of this switching ring is consistent with what is observed in the experimental work on FePt and CoPt of Refs. [11,49,52].

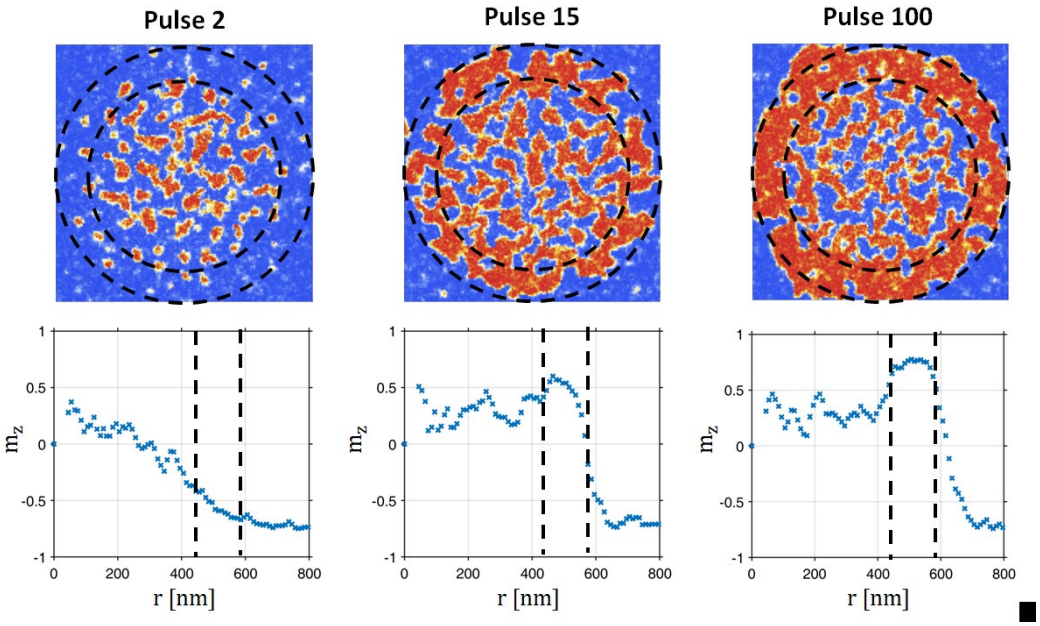

Figure 6-4: Optical magnetization reversal induced by σ_+ light after 2,15, and 100 pulses. The plots show the average magnetization as a function of the distance r from the center of the beam. The black dotted lines delimit the region of the optical reversal ring.

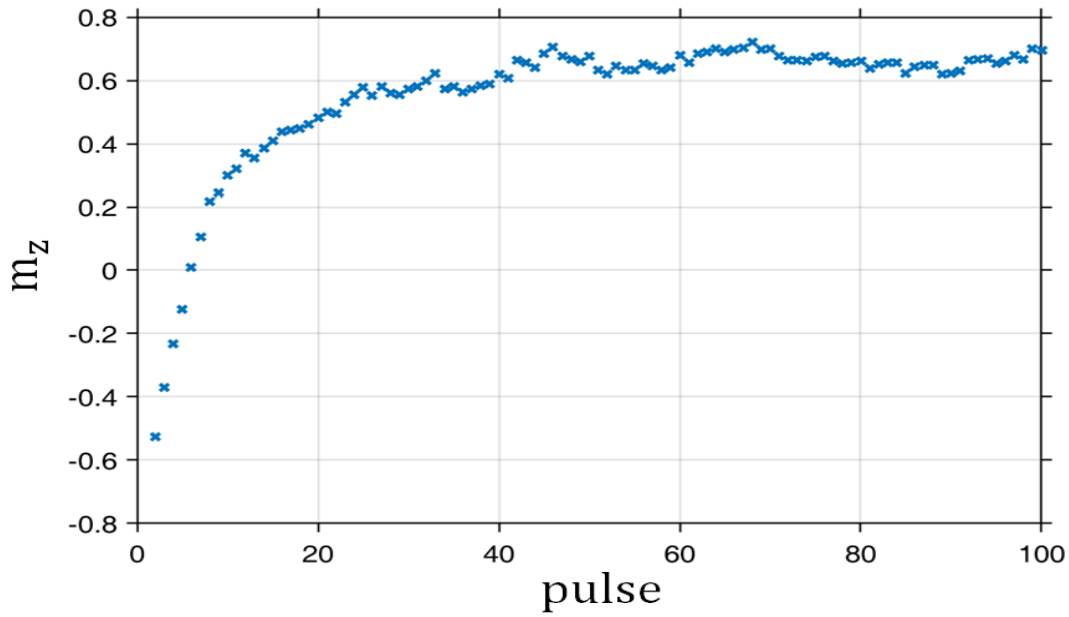

Figure 6-5: Average magnetization inside the optical reversal ring as a function of the number of pulses.

The magnetization inside the optical reversal ring, region (2), follows a rapid demagnetization in the first few pulses, followed by a slow re-magnetization in the up state. The domain up generated at the interface between region (3) and region (2) are slowly pushed outward by an optically induced domain expansion over several hundred pulses (Figure 6-4). The net magnetization inside the ring increases linearly with the number of pulses until a plateau is reached, and the optical excitation is balanced by the effect of the thermal demagnetization (Figure 6-5). These simulation shows the same behavior observed experimentally in multilayer Pt/Co/Pt through indirect measure of the anomalous Hall voltage [58].

B Helicity Dependent Domain Wall Displacement

Let us consider a long FePt strip $1.2\ \mu\text{m} \times 0.2\ \mu\text{m}$ FePt film and $6\ \text{nm}$ thickness. A domain wall is created at the center of the strip (Figure 6-6). The strip is divided into an up domain on the right side of the strip and a down domain on the left side of the strip. A laser with a beam radius of $w_0 = 40\ \mu\text{m}$ is focused at the center of the strip. The laser has a peak fluence in the range $F_0 = 40 - 44\ \text{mJ/cm}^2$. These peak fluences are chosen to ensure $I_1 < I_0 \ll I_2$, so that no nucleation is observed inside the strip. Given the large beam radius and the relatively low fluence, the temperature gradient between the center of the strip and the edge at the equilibrium is of the order of $\Delta T \sim 0.2\ \text{K}$.

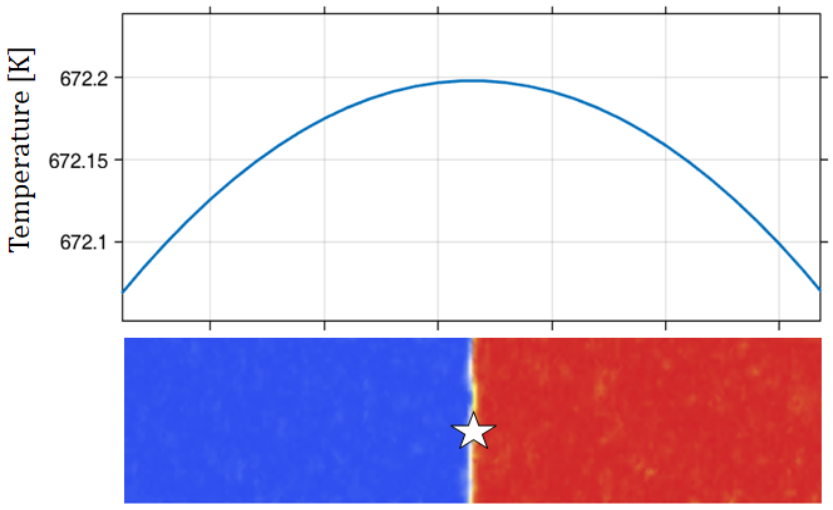

Figure 6-6: Initial setup for the HD-DWD simulation. A domain wall is generated at the center of the strip. The white star indicated the center of the laser beam spot and the temperature profile along the x direction is given in the plot.

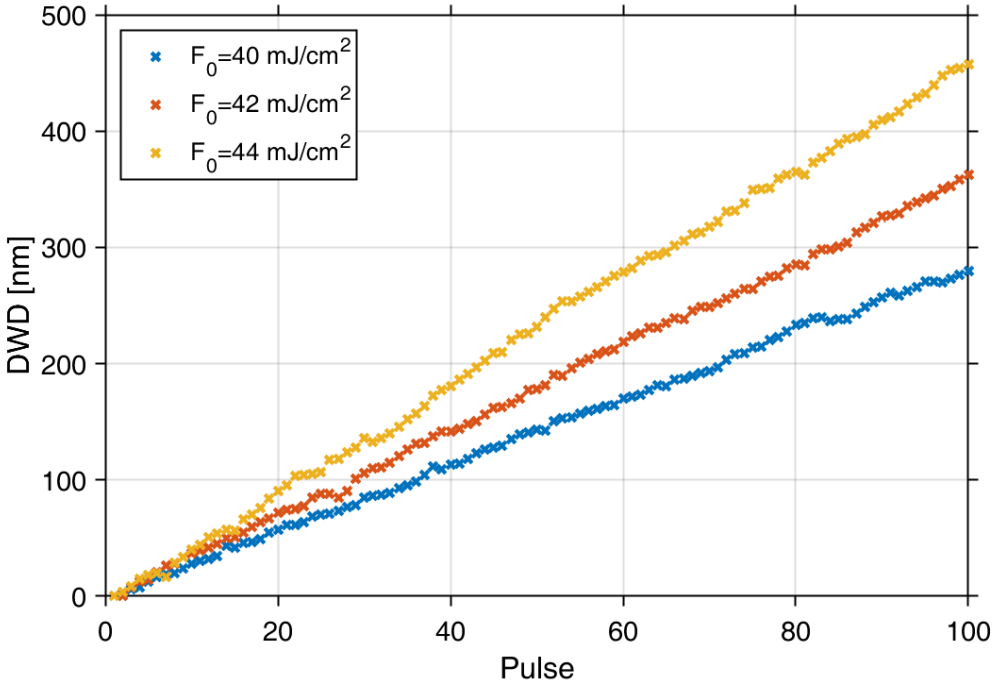

Figure 6-7: Domain wall displacement in nm as a function of the number of pulses for different peak fluence.

The temperature gradient moves the domain wall toward the center of the beam (hot spot) whereas the optical excitation σ_+ increases the dimension of the up domain by pushing the domain wall via the ultrafast optical damping/anti-damping described in Sec. 5.5B. The balance between the thermal and the optical effect on the domain wall, determined the elementary displacement induced by the optical excitation after each pulse (Figure 6-7). The results show that the average displacement per pulse is a linear function of the local peak intensity $I(r)$. Hence, for a Gaussian pulse, the speed of the domain wall displacement, v_{DWD}, is expected to be maximum during the first pulses when the peak intensity at the domain wall is maximum and decreases linearly with $I(r)$, finally stopping when $I(r) \leq I_1$. This behavior

is qualitatively consistent with the experimental observation on CoPt thin films carried over by Medapalli and Quessab [52,59].

ACKNOWLEDGEMENT

The author thanks Professor Eric E. Fullerton, Professor Stéphane Mangin, Dr. Rajasekhar Medapalli, Dr. Yassine Quessab, and Philippe Sched for the discussions on experimental and simulation data.

CHAPTER 7 - EVALUATION OF THE THERMAL FLUCTUATIONS IN THE LANDAU-LIFSHITZ-BLOCH MODEL

Understanding the magnetization dynamics at high temperature is important for our fundamental understanding of nanomagnetism and for a set of applications, such as heat assisted magnetic recording technologies (HAMR) [84-86] and ultrafast optical processes [24,52,58,59]. Numerically modeling such systems is complicated because the material properties change significantly at elevated temperatures, especially at temperatures near or above the Curie temperature.

Atomistic spin models have been used to provide parameterization of thermal properties, such as the equilibrium magnetization $m_e(T)$, anisotropy, and susceptibility [87]. The atomistic models, however, are not fit to simulate large-scale systems, such as those of common interest in magnetic recording and opto-magnetic simulations. To solve this problem, several micromagnetic models have been proposed that use a macrospin to represent the behavior of an ensemble of atoms. The field acting on this magnetization vector is obtained from the atomistic Hamiltonian via the mean field approximation as shown in Chapter 1. In micromagnetic models, the average magnetization of the system at a certain temperature is described by the equilibrium magnetization obtained from the atomistic model. Additionally, elevated temperatures result in thermal noise. The introduction of stochastic fluctuations that correctly model the behavior of this noise is of practical importance to study the magnetization behavior, such as reversal time, signal to noise ratio, and jitter in HAMR.

Several stochastics forms have been proposed to introduce the thermal fluctuations in the LLB model [6,7,88]. These models have several limitations when applied to thin films and granular media, because they either:

- Overestimate the strength of the thermal fluctuations, leading to a value of the magnetization at equilibrium for the macrospin different than the one expected from the atomistic model [7].
- Neglect to introduce the thermal fluctuation on the magnetization length, ignoring the thermal effect when the thermal energy is comparable to the molecular field (i.e. $T \sim T_C$) [88].

Overestimating the strength of the fluctuation might leads to the wrong estimation of the SNR in numerical model, in particular for small granular structures, making these models unable to correctly describe the noise effect HAMR simulations. Moreover, the shift from the equilibrium magnetization make these stochastic models unfit to be used in multiscale modeling frameworks.

Neglecting the thermal fluctuation on the direction of the magnetization length, allow to preserve the value of the equilibrium magnetization at elevated temperature, making these kinds of models more suited to multiscale modeling. However, ignoring the contribution of the thermal fluctuations even above the curie temperature T_C, leads to an incorrect thermal demagnetization dynamics when the material is subjected to an ultrafast thermal pulse [33].

In this chapter, we introduce an alternative form for the stochastic LLB and LLL model which is consistent with the solution of the Fokker-Planck (FP) equation and it is consistent at low temperature with the fluctuations obtained using the Fluctuation-Dissipation Theorem

(FDT). The main feature of this stochastic model is the ability to preserving the magnitude of the equilibrium magnetization without ignoring the stochastic contribution of the longitudinal component, allowing the model to correctly describe the thermal magnetization dynamic induced by an ultrafast laser pulse.

The model is based on the formalism introduced by Garcia-Palacios [17] and Garanin [6]. The model is validated against other existing formulation of the stochastic LLB by considering the distribution of the magnetization at equilibrium for a single macrospin particle.

7.1 THE LLB-LANGEVIN EQUATION

The starting point of our derivation is the LLB equation introduced in Sec 2.3. We construct the Langevin form by introducing the stochastic fluctuations in the orthogonal components of Eq.(2.39) an additive term to the field, including precession, longitudinal relaxation, and transverse relaxation components. This leads to three orthogonal multiplicative noises. The Langevin form of the magnetization dynamics can be written as:

$$\frac{dm_i}{dt} = A_i(\mathbf{m},t) + \sum_{k=1}^{3} B_{ik}^{(0)}(\mathbf{m},t)L_k^{(0)}(t) + \sum_{k=1}^{3} B_{ik}^{(1)}(\mathbf{m},t)L_k^{(1)}(t) + \sum_{k=1}^{3} B_{ik}^{(2)}(\mathbf{m},t)L_k^{(2)}(t) \ , \tag{7.1}$$

$$A_i = \gamma\left[\mathbf{m}\times\mathbf{H}_{eff}\right]_i - \gamma\alpha_{\|}\left(\frac{1-B_S(m\beta\tilde{J}_0)/m}{\mu_0\beta B_S^{'}(m\beta\tilde{J}_0)}\right)m_i - \gamma\alpha_{\perp}\frac{\left[\mathbf{m}\times\left(\mathbf{m}\times\mathbf{H}_{eff}\right)\right]_i}{m^2} \ , \tag{7.2}$$

$$B_{ik}^{(0)} = \gamma\sum_{j=1}^{k}\epsilon_{ijk}m_j \qquad B_{ik}^{(1)} = \frac{\gamma\alpha_{\|}}{m^2}m_i m_k \qquad B_{ik}^{(2)} = \frac{\gamma\alpha_{\perp}}{m^2}\left(m^2\delta_{ik} - m_i m_k\right) \ , \tag{7.3}$$

where $\mathbf{m} = \left\{m_x, m_y, m_z\right\}$ with $i = x, y, z$, ϵ_{ijk} is the Levi-Civita symbol defining the totally antisymmetric unit tensor, and δ_{ik} is the delta function. The "Langevin" sources $L_k^{(v)}$ are modelled as Wiener stochastic processes and are assumed to be (i) Gaussian with zero mean,

(ii) stationary, (iii) and such that $L_k^{(v)}(t)$ and $L_k^{(v)}(t+\tau)$ are correlated only for a time interval τ that is much shorter than the time required to observe an appreciable change in the magnetization (i.e. we assume that the collision time between spins is much shorter than the micromagnetic relaxation time). Under these assumptions the Langevin sources can be written as:

$$\left\langle L_k^{(v)}(t)\right\rangle = 0, \qquad \left\langle L_k^{(v)}(t) L_l^{(v)}(s)\right\rangle = 2D_v \delta_{kl}\delta(t-s)\ , \tag{7.4}$$

Where D_v with $v = 0,1,2$ are the diffusion coefficients to be determined by solving the associated FP equation at equilibrium.

7.2 THE FOKKER-PLANCK EQUATION

The time evolution of the transitional probability density function $f(m,t)$ governing the magnetization can be obtained by solving the Fokker-Planck equation associated to the LLB-Langevin equation, Eq. (7.1). Since the noise enters in the system in a multiplicative way, the correct Langevin equation has to be solved using the Stratonovich calculus interpretation to obtain the correct thermal equilibrium properties [17]. Using the Stratonovich calculus it is possible to write the FP equation in the form of a continuity equation for the probability density f :

$$\frac{\partial f}{\partial t} = -\sum_i \frac{\partial}{\partial m_i}\left\{\left[A_i - \sum_{v=0}^{2} D_v \left[\sum_k B_{ik}^{(v)} \left(\sum_j \frac{\partial B_{jk}^{(v)}}{\partial m_j} \right) - \sum_k B_{ik}^{(v)} B_{jk}^{(v)} \frac{\partial}{\partial m_j} \right] \right] f \right\}\ . \tag{7.5}$$

The derivate of the functions $\partial B_{jk}^{(v)} / \partial m_j$ can be expressed explicitly as:

$$\sum_{j=1}^{3} \frac{\partial B_{jk}^{(1)}}{\partial m_j} = \gamma \sum_{j,i=1}^{3} \epsilon_{jik} = 0 \qquad \sum_{j=1}^{3} \frac{\partial B_{jk}^{(1)}}{\partial m_j} = 2\frac{\gamma \alpha_{\parallel}}{m^2} m_k \qquad \sum_{j=1}^{3} \frac{\partial B_{jk}^{(2)}}{\partial m_j} = -2\frac{\gamma \alpha_{\perp}}{m^2} m_k\ . \tag{7.6}$$

The noise-induced drift coefficient $\sum_k B_{ik}^{(v)} \sum_j \partial B_{jk}^{(v)} / \partial m_j$ in the FP equation can be written, using the result in Eq. (7.6) as:

$$\sum_{k=1}^{3} B_{ik}^{(0)} \sum_{j=1}^{3} \frac{\partial B_{jk}^{(0)}}{\partial m_j} = \sum_{k=1}^{3} B_{ik}^{(2)} \sum_{j=1}^{3} \frac{\partial B_{jk}^{(2)}}{\partial m_j} = 0 \qquad \sum_{k=1}^{3} B_{ik}^{(1)} \sum_{j=1}^{3} \frac{\partial B_{jk}^{(1)}}{\partial m_j} = \frac{2\gamma\alpha_{\parallel}}{m^2} m_i \ . \tag{7.7}$$

Using Eq.(7.7) in Eq.(7.5) it is possible to rewrite the FP equation in an explicit form:

$$\begin{aligned} \frac{\partial f}{\partial t} = & -\frac{\partial}{\partial \mathbf{m}} \left\{ \gamma \mathbf{m} \times \mathbf{H}_{eff} - \gamma\alpha_{\parallel} \left(\frac{1 - B_S\left(m\beta\tilde{J}_0\right)/m}{\mu_0 \beta B_S'\left(m\beta\tilde{J}_0\right)} \right) \mathbf{m} - \frac{\gamma\alpha_{\perp}}{m^2} \left[\mathbf{m} \times \left(\mathbf{m} \times \mathbf{H}_{eff} \right) \right] \right\} \\ & - \frac{\partial}{\partial \mathbf{m}} \left\{ \gamma^2 \left(D_0 + \frac{\alpha_{\perp}^2 D_2}{m^2} \right) \left[\mathbf{m} \times \left(\mathbf{m} \times \frac{\partial f}{\partial \mathbf{m}} \right) \right] - \frac{\gamma^2 \alpha_{\parallel}^2 D_2}{m^2} \left(\mathbf{m} \cdot \frac{\partial f}{\partial \mathbf{m}} \right) \mathbf{m} \right\} \\ & - \frac{\partial}{\partial \mathbf{m}} \left(2\gamma^2 \alpha_{\parallel}^2 D_2 \frac{\mathbf{m}}{m^2} f \right) \end{aligned} \ , \tag{7.8}$$

where the last term in the equation is due to the noise-drift component acting on the magnetization length. The FP equation should be solved in the stationary case (i.e. $\partial f / \partial t = 0$) to obtain the value of the diffusion coefficients. The solution of Eq.(7.8) in the stationary state diverges from the Boltzmann distribution due to the presence of the noise-drift component. This difference is negligible at low temperature and becomes significant for temperature close to T_C. The solution can instead be found in the form of a Poisson-like distribution:

$$f(\mathbf{m}) = f_0 m^2 \exp\left(-\frac{\mathcal{E}_M(\mathbf{m})}{k_b T} \right) = f_0 m^2 \exp\left(-\frac{M_S^0 V \left(\mathbf{m} \cdot \mathbf{H}^{MFA} \right)}{k_b T} \right) , \tag{7.9}$$

where $\mathcal{E}_M(\mathbf{m})$ is the micromagnetic free energy of the system defined in Eq.(2.19), and f_0 is a scaling factor. The solution of the FP equation associated to the LLB-Langevin is not unique, but the physical quantities obtained by averaging over different realizations are the same if the choice of the diffusion coefficients solve the FP equation, as shown for the Landau-Lifshitz

equation in Ref. [17]. Under the assumption of uncorrelated fluctuations, we can choose to set $D_0 = 0$ in Eq.(7.8) and set the following condition for the fluctuating strength at the equilibrium:

$$\mathbf{m} \times \mathbf{H}_{eff} = 0 \ , \tag{7.10}$$

$$\frac{\gamma^2 \alpha_{\|}^2 D_1}{m^2} \mathbf{m} \left(M_S^0 V \frac{\mathbf{m} \cdot \mathbf{H}^{MFA}}{k_b T} + 2 \right) f = -\gamma \alpha_{\|} \mathbf{m} \left(\frac{1 - B_S / m}{\mu_0 \beta B_S^{'}} \right) f + 2\mathbf{m} \frac{\gamma^2 \alpha_{\|}^2 D_1}{m^2} f \ , \tag{7.11}$$

$$\frac{\gamma^2 \alpha_{\perp}^2 D_2}{m^2} \left[\mathbf{m} \times \left(\mathbf{m} \times \mathbf{H}^{MFA} \right) \right] = \frac{\gamma \alpha_{\perp}}{m^2} \left[\mathbf{m} \times \left(\mathbf{m} \times \mathbf{H}_{eff} \right) \right]. \tag{7.12}$$

The diffusion coefficient can then be found in the form:

$$D_1 = \frac{k_b T}{\gamma \alpha_{\|} M_S^0 V} \eta \qquad D_2 = \frac{k_b T}{\gamma \alpha_{\perp} M_S^0 V}, \tag{7.13}$$

where the diffusion coefficient D_2 has been found by noticing $\mathbf{m} \times \mathbf{m} \times \mathbf{H}_E = 0$ for any $\mathbf{m}$, and the η coefficient at the equilibrium is a function of the temperature:

$$\eta = \frac{1 - B_S(m_0 \beta \tilde{J}_0) / m_0}{\beta \tilde{J}_0 B_S^{'}(m_0 \beta \tilde{J}_0)} \ . \tag{7.14}$$

Below T_C, the value of the instantaneous magnetization at the equilibrium is well defined and $\eta = 0$, whereas above T_C, the solution can be obtained by expanding the Brillouin function in Taylor series around 0, leading to:

$$\eta = \frac{1 - \beta \tilde{J}_0 / 3}{\beta \tilde{J}_0 / 3} \approx \frac{T - C(S) T_C}{C(S) T_C} \ , \tag{7.15}$$

where $C(S) = S / (3S + 3)$, with S being the effective spin number for the ferromagnetic material, and where the approximation in Eq. (7.15) has been obtained under the assumption $|H_E| \gg |H_{eff}|$. The diffusion coefficient D_1 can then be rewritten as:

$$D_1 = \begin{cases} 0 & \text{for } T < T_C \\ \dfrac{k_b\left(T - C(S)T_C\right)}{2\gamma\lambda C(S)M_S^0 V} & \text{for } T \geq T_C \end{cases} . \tag{7.16}$$

The diffusion coefficient shows that below T_C the effect of the fluctuation on the longitudinal component of the magnetization is negligible. The micromagnetic magnetization is obtained by averaging over random dissipative processes where the spin exchange interaction is the dominant force of the system. When the temperature rises above the T_C, the contribution of the thermal fluctuation and the contribution of the spin-exchange interaction are comparable and a fluctuation has to be included on the direction of the magnetization. Since the vector length cannot assume negative values, the distribution of the magnetization for an isotropic ferromagnetic particle cannot be represented by a symmetric Boltzmann distribution. This kind of non-Boltzmann distribution is common in physics to describe the distribution of a vector length in the presence of an external fluctuation source, e.g. the wind speed in many wind power generation models.

To understand this behavior we can consider the magnetization length for a small particle as the sum of a discrete population of N contained inside the elementary volume V. For simplicity we consider the spin to be able to assume only states $S_z = \pm 1$. The magnetization length can then be expressed as:

$$|m| = \frac{1}{N}\left|\sum_{i=1}^{N} S_i\right| . \tag{7.17}$$

At low temperature (i.e. $T \ll T_C$) the spin tends to locally align in the same direction inside V. When the temperature is close to the Curie point (i.e. $T \geq T_C$), the number of spin

up and spin down are almost the same, providing a value of the equilibrium magnetization close to zero and a wider standard deviation. Since the magnetization length is a positive number, the spin flipping cannot produce a negative magnetization length creating an asymmetric Poisson-like distribution as expected from Eq. (7.9). It has to be noticed that this deviation from the Boltzmann distribution is a proportional to the size of the single domain particle, since the diffusion coefficient is proportional to $D_2 \sim V^{-1}$. For larger magnetic particle, (i.e. $N \to \infty$) the contribution of the thermal fluctuation on the longitudinal component of the magnetization becomes negligible at all temperature. It is important to note, however, that in various applications, e.g. HAMR, the dimension of the grains is of the order of [86,89], and a correct assessment of the noise in this range is important for providing quantitative and qualitative information on the contribution of the noise. Moreover, the intensity of the longitudinal noise can influence the intensity of the optical source necessary to describe the optical reversal in ferromagnetic and ferrimagnetic media [49,90].

7.3 FLUCTUATION-DISSIPATION THEOREM

In the previous section, we obtained the diffusion coefficients for the thermal fluctuation by solving the FP equation associated with the Langevin form of the LLB equation. Using that approach we deal with a complete non-linear problem resulting from multiplicative noise in term of the probability distribution f. The absence of fluctuations at low temperature obtained in Eq.(7.16) may seems counter-intuitive. One would expect that the result we obtained be equivalent to the one obtained using the fluctuation dissipation theorem (FDT).

The FDT is a linear-response theory, valid for small deviation from the equilibrium. Generally speaking, the noise in the LLB equation is multiplicative. However, at low temperatures and for small fluctuations of the magnetization δm near the equilibrium magnetization (i.e. $\delta m \ll m_0$), we can linearize the equation converting the multiplicative noise into an additive noise variable. The linearized system of equation can then be written in the absence of thermal fluctuations as:

$$\frac{dx_i}{dt} = \sum_{j=1}^{3N} L_{ij} m_j \ , \tag{7.18}$$

where $i = 1,\ldots,3N$ are the degrees of freedom of the system, N is the number of particles in the system, $x_i = \delta m_i$ is the deviation of the subsystem i from the equilibrium, and L_{ij} are the components of the linearize matrix $\mathbf{L}$. Following the formulation in Ref. [91,92], the general linearized Langevin equation of motion is written as:

$$\frac{dx_i}{dt} = -\sum_{j=1}^{3N} \gamma_{ij} X_j + f_i \ , \tag{7.19}$$

where γ_{ij} are the kinetic coefficients, f_i represent random forces responsible for the spontaneous fluctuation, and X_i are thermodynamically conjugate variables related to the entropy $\mathcal{S}$ of the magnetic system by:

$$X_i = -\frac{\partial \mathcal{S}}{\partial x_i} \ , \tag{7.20}$$

and for a close system is an external medium, Eq.(7.20) can be written as:

$$X_j = \beta \frac{\partial \mathcal{E}_M(\mathbf{x})}{\partial x_j} = -\beta M_S V h_j = -\beta M_S V \sum_{i=1}^{3N} B_{ij} x_i \ , \tag{7.21}$$

where the free energy of the system $\mathcal{E}_M(\mathbf{x})$ in function of the term x_i, and $h_i = \sum_j B_{ij} x_j$ defines the field variation due to the small fluctuations of the magnetization. The statistical properties of the random forces f_i in Eq. (7.19) can be obtained by using the Onsager principle:

$$\langle f_i(t) \rangle = 0 \qquad \langle f_i(0) f_j(t) \rangle = (\gamma_{ij} + \gamma_{ji}) \delta(t) \tag{7.22}$$

where $\sigma_{ij} = (\gamma_{ij} + \gamma_{ji})$. The kinetic coefficients can be obtaining by setting Eq.(7.18) equal to Eq. (7.19) in the absence of fluctuations:

$$\gamma_{ij}^{\mu\nu} = \frac{L_{ij}^{\mu\nu}}{\beta M_S V B_{ij}^{\mu\nu}} \tag{7.23}$$

where $i, j = 1, \ldots, N$ and $\mu, \nu = x, y, z$. To evaluate the kinetic coefficients, let us consider an initial magnetization $\mathbf{m}_i = \{0, 0, m_0\}$, and we introduce a small fluctuation of the magnetization (i.e. $\delta m_{i,x}, \delta m_{i,y}, \delta m_{i,z} \ll m_0$) . The components of the field matrix B_{ij} are given by:

$$B_{ij}^{xx} = \left[\frac{2A_{ex}}{M_S h^2} (\delta_{i,j+1} - 2\delta_{i,j} + \delta_{i,j-1}) - H_K \delta_{ij} \right], \tag{7.24}$$

$$B_{ij}^{yy} = \left[\frac{2A_{ex}}{M_S h^2} (\delta_{i,j+1} - 2\delta_{i,j} + \delta_{i,j-1}) - H_K \delta_{ij} \right], \tag{7.25}$$

$$B_{ij}^{zz} = \left[\frac{2A_{ex}}{M_S h^2} (\delta_{i,j+1} - 2\delta_{i,j} + \delta_{i,j-1}) + \frac{J_0}{\mu_0} \delta_{ij} \right], \tag{7.26}$$

and $B_{ij}^{\mu\nu} = 0$ for $\mu \neq \nu$. Similarly, we can obtain the elements of the linearized matrix L_{ij} as:

$$L_{ij}^{xx} = \frac{\gamma \tilde{\alpha}_\perp}{m_0^2} \left[\frac{A_{ex}}{M_S h^2} (\delta_{ij-1} - 2\delta_{ij} + \delta_{ij}) - H_k \delta_{ij} \right], \tag{7.27}$$

$$L_{ij}^{yy} = \frac{\gamma \tilde{\alpha}_\perp}{m_0^2} \left[\frac{A_{ex}}{M_S h^2} (\delta_{ij-1} - 2\delta_{ij} + \delta_{ij}) - H_k \delta_{ij} \right], \tag{7.28}$$

$$L_{ij}^{zz} = \frac{\tilde{\alpha}_{\|}}{m_0^2 \beta \mu_0 B'(\xi_0)} \left[B_S\left(\xi_0\right) + m_0 \frac{\delta\xi_0}{\delta m} B'(\xi_0) - 2m_0 \right], \tag{7.29}$$

$$L_{ij}^{xy} = -L_{ij}^{yx} = -\gamma \left[\frac{A_{ex}}{h^2}\left(\delta_{ij-1} - 2\delta_{ij} + \delta_{ij}\right) - H_k \delta_{ij} \right], \tag{7.30}$$

$$L_{ij}^{xz} = L_{ij}^{yz} = L_{ij}^{zx} = L_{ij}^{zy} = 0 \ , \tag{7.31}$$

where $\delta\xi_0 = \mu_0 \beta h$ is the fluctuation of the reduced magnetization induced by the small changes in the magnetization. Using the relationship $\delta m / \delta\xi_0 = B_S^{'}(\xi_0)$ in Eq. XX we can show that $L_{ij}^{zz} = 0$. The symmetrized kinetic coefficient σ_{ij} is given by:

$$\sigma^{xx} = \sigma^{yy} = \frac{2\alpha_{\perp} k_b T \gamma}{M_s V} \qquad \sigma^{zz} = 0 \ . \tag{7.32}$$

Hence, the longitudinal fluctuation in our system is zero. And the random forces are given by:

$$\left\langle f_i(t) \right\rangle = 0 \qquad \left\langle f_i(t) f_j(s) \right\rangle = 0 \qquad \text{for } i \neq j \ , \tag{7.33}$$

$$\left\langle f_x(t) f_x(s) \right\rangle = \sigma^{xx} \delta(t-s) \quad \left\langle f_y(t) f_y(s) \right\rangle = \sigma^{yy} \delta(t-s), \tag{7.34}$$

$$\left\langle f_z(t) f_z(s) \right\rangle = 0 \ . \tag{7.35}$$

This result is equivalent to the stochastic fluctuations solving the FDT agrees to the result obtained by solving the FP equation below the Curie point.

7.4 MODEL COMPARISON

Let us define the stochastic LLB formulation derived in this chapter as LLB-III. The current formulation has similarities and differences with respect to the stochastic LLB-I and LLB-II introduced in Sec.2.4.

Compared to the LLB-I formulation [11], the LLB-III only differs in the value of the longitudinal diffusion coefficient by a factor η. For $\eta = 1$, the two formulation leads to the same diffusion coefficient (i.e. $D_1 = D_{\parallel,LLB-I}$ and $D_2 = D_{\perp,LLB-I}$). In general, $\eta < 1$ for LLB-III. The greater longitudinal fluctuations introduced in the LLB-I may lead to underestimation of the mean value of the magnetization as compared to the equilibrium magnetization $m_e(T)$.

In the LLB-II, the noise is introduced via a multiplicative noise acting on the transverse damping component, and an additive noise. The use of an additive and multiplicative stochastic fields leads to overestimate the value of the equilibrium magnetization obtained numerically with respect to the input equilibrium magnetization $m_e(T)$. This overestimation can be understood by considering that a strong additive noise in multidimensional systems with nonlinearities can generate a random shift far from the deterministic attractor, referred to as a "phantom attractor" [93]. Increasing the volume of the single domain particle reduces the intensity of this additive noise thus removing the effect of the phantom attractor. However, for various applications the particles can be small, and one needs to be able to model their behavior.

To study the behavior of the LLB-III compared to the LLB-I and LLB-II model, we considered the magnetization distribution around the equilibrium for (i) an isotropic single-domain particle and (ii) and anisotropic particle with uniaxial anisotropy along the z-direction. The considered particles has Curie Temperature $T_C = 700\text{K}$ ($J_0 = 3k_bT_C$), saturation magnetization $M_S^0 = 500\ \text{emu/cm}^3$, and magnetic moment of $\mu_0 = 5\mu_B$. Since we are interested in the equilibrium, we use the atomistic damping coefficient of its the critical value. For the integration scheme we used a time-step of $\Delta t = 1\ \text{fs}$.

The magnetization of the system is initially set equal to the equilibrium magnetization obtained from the atomistic model for an ideal SC lattice material [94] and the system is equilibrated for 1ns. The magnetization distribution is obtained from the equilibrated system by sampling the distribution over 10ns.

A Isotropic Particle

We first consider the case of an isotropic particle (i.e. $H_K = 0$). In the absence of an isotropic component there is no energy barrier in the direction transverse to the magnetization. Thus, the distribution of the magnetization with respect to the polar angle θ is uniform for all 3 models.

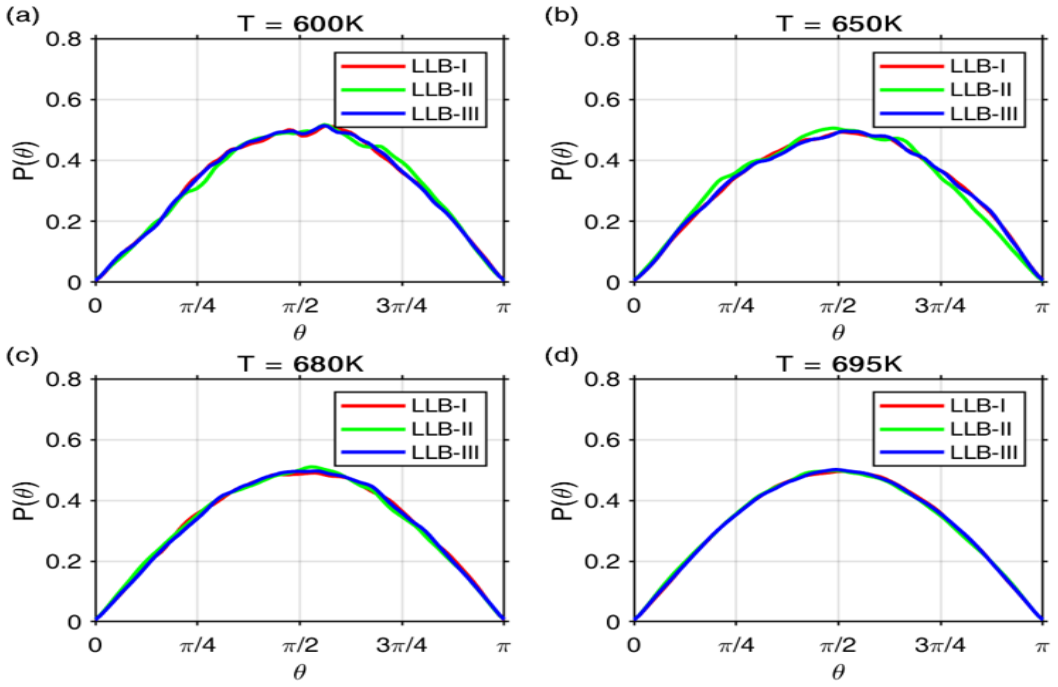

Figure 7-1: Distribution with respect to the polar angle θ for an isotropic particle ($L = 5$ nm) for the LLB-I (red lines), LLB-II (green lines), and LLB-III (blue lines) models. The results are given at different temperatures for (a) $T = 600$ K , (b) $T = 650$ K , (c) $T = 680$ K , and (d) $T = 695$ K .

Since below T_C the LLB-III model does not have any fluctuations along the longitudinal direction of the magnetization, the average length of the magnetization for $T \leq T_C$ is preserved (Figure 7-2a). For temperature close to T_C, due to the presence of a longitudinal fluctuation component, the LLB-I model underestimate the value of the equilibrium magnetization, whereas the LLB-II overestimate it (Figure 7-2b). The overestimation of m_e close to T_C can be explained by the presence of a "phantom" aggregator when the strength of the longitudinal fluctuation is comparable with the strength of the molecular field. For $T > T_C$, this effect leads to large mean magnetization magnitude values (around 10% of the saturation value) for the LLB-II model, which are significantly higher than the values obtained using either the LLB-I and LLB-II.

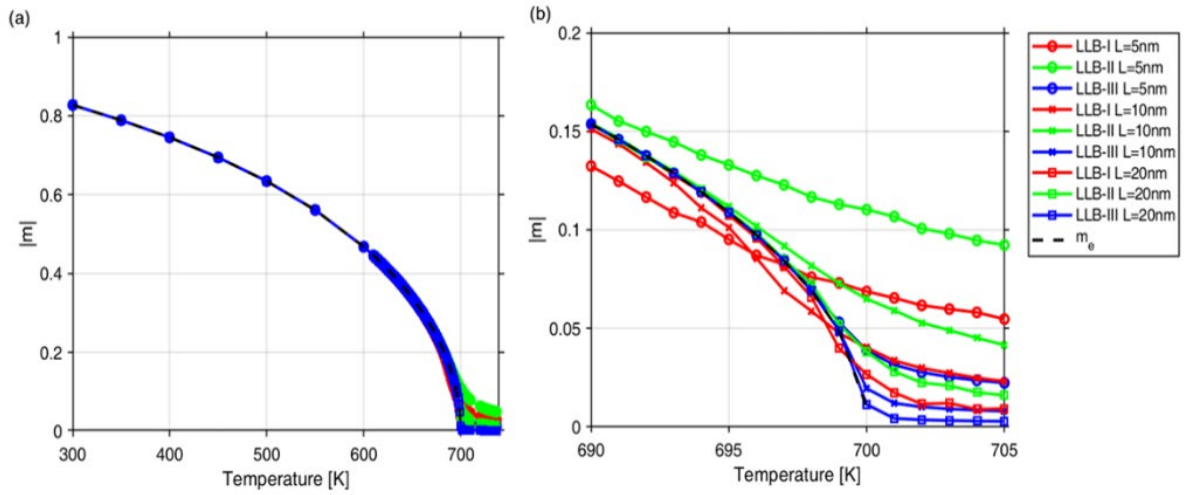

Figure 7-2: (a) Magnetization length versus temperature.(b) Magnetization length for the range of temperature near T_C. The results are presented for particle of different sizes: $L = 5$ nm (circles), $L = 10$ nm (crosses), and $L = 20$ nm (squares). The results are presented for the LLB-I (red lines), the LLB-II (green lines), and the LLB-III (blue lines) models.

The displacement from the expected equilibrium magnetization m_e is a function of the particle volume. Increasing the diameter of the particle, reduces the diffusion coefficient in all 3 models, and for particles with size of the order of $L = 20\ \text{nm}$, the difference between the models becomes negligible. Above T_C, the LLB-I and LLB-III model shows qualitatively the same Poisson-like distribution of the magnetization, whereas the LLB-II model follow a Boltzmann distribution for the magnetization length (Figure 7-3).

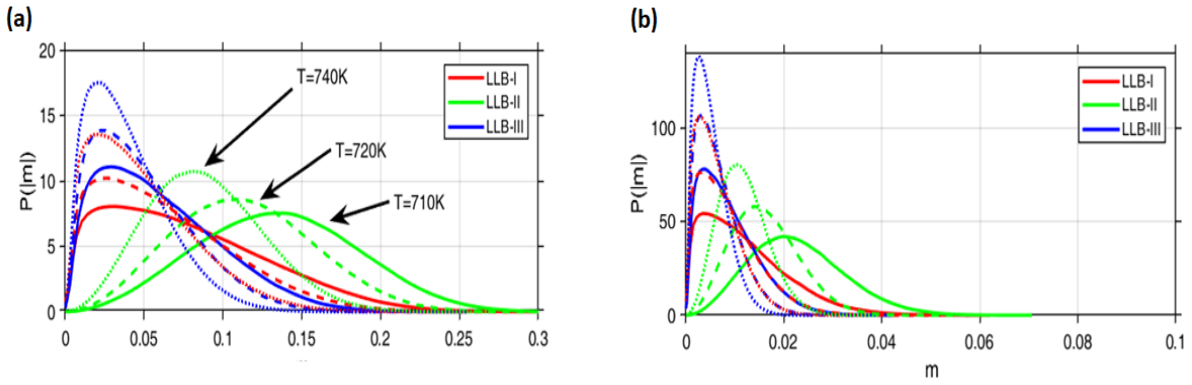

Figure 7-3: Distribution of the magnetization for an isotropic particle above $T_C = 700\ \text{K}$. The results are shown for (a) small ($L = 5\ \text{nm}$), and (b) large ($L = 20\ \text{nm}$) magnetic particles.

B Anisotropic Particle

We consider a particle with a uniaxial anisotropy field along the z-axis given by $H_K = 1.0\ \text{T}$. Due to the presence of the uniaxial anisotropy, an energy barrier is introduced in the direction transverse to the magnetization. The probability distribution along θ shows two peaks around $\theta = 0$ and $\theta = \pi$ at low temperature (Figure 7-4a) due to the presence of the uniaxial anisotropy that gives the magnetization a preferential direction along the axis z. The two peaks decrease with the temperature (Figure 7-4b,c), and the distribution becomes identical

to the isotropic case for temperature close to T_C (Fig. 4d). For $T > T_C$, the mean magnetization and the probability density of the magnetization length becomes identical to the isotropic case and they are not shown.

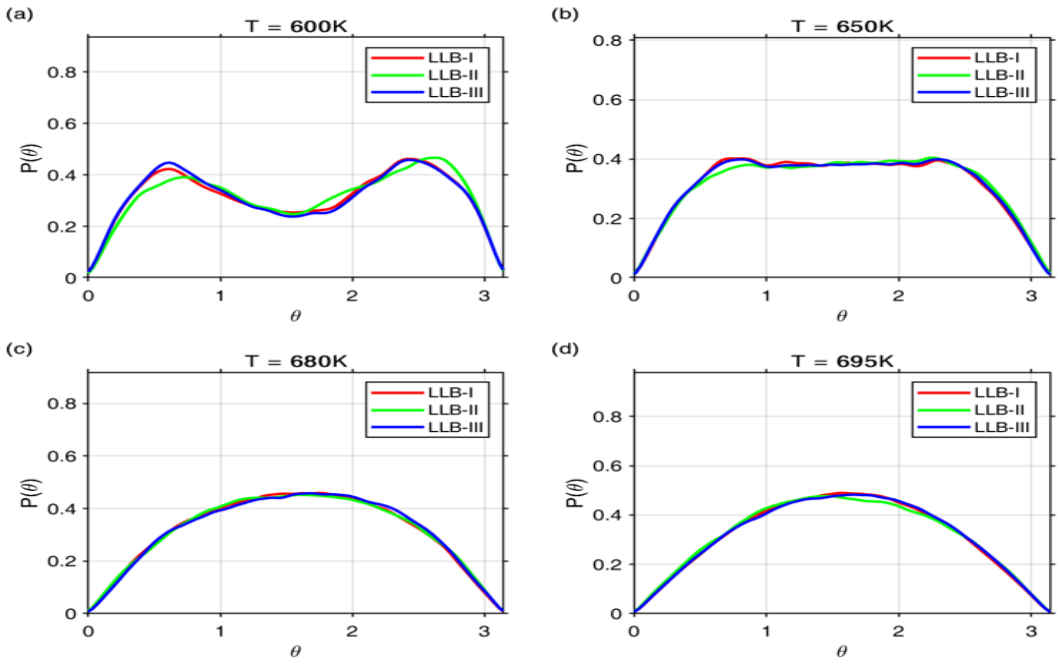

Figure 7-4: Distribution with respect to the polar angle θ for an anisotropic particle ($L = 5$ nm) for the LLB-I (red lines), LLB-II (green lines), and LLB-III (blue lines) models. The results are given at different temperatures for (a) $T = 600$ K, (b) $T = 650$ K, (c) $T = 680$ K, and (d) $T = 695$ K.

7.5 SUMMARY

We introduced a new formulation for the stochastic LLB equation, LLB-III, and I tested the model with respect to the equilibrium magnetization and the distribution of the magnetization along θ for particles of different sizes. The results have been compared with the existing formulations used in micromagnetics.

The LLB-III formulation differs from the previous model for its treatment of the thermal fluctuations in the direction of the magnetization. Similarly to the stochastic self-consistent

Bloch (SCB) model for the magnetization dynamics [88,95], the LLB-III model has a vanishing longitudinal fluctuations for $T < T_c$, similar to stochastic model. However, the SCB diverges from the LLB-III, where the strength of the longitudinal fluctuation is a function of $\eta(T) \sim T$.

An important property of the LLB-III model is that it recovers the expected mean value of the magnetization at the equilibrium for small and large magnetic particles. The distribution of the magnetization length is a Poisson-like distribution rather than the classical Boltzmann distribution as typically assumed for such systems. The preservation of the equilibrium magnetization makes the presented model appealing for HAMR [96] and multiscale atomistic-micromagnetic modeling [87].

ACKNOWLEDGEMENT

This chapter is, in part, a reproduction of the material presented in M. Menarini and V. Lomakin, "Thermal Fluctuations in the Landau-Lifshitz-Bloch model" currently under review in Physical Review B. A previous version of the same is available online on arXiv [97]. The dissertation author was the primary investigator and author of this material.

CHAPTER 8 - CONCLUSIONS AND OUTLOOK

This work introduced a micromagnetic simulator to study the magnetization dynamics of mesoscopic ferri- and ferro-magnetic system subjected to optical and thermal excitation via ultrafast laser pulses.

The simulator was used to efficiently simulate large granular structures and thin films. To showcase the potential of the code, we studied the THz signal induced in a thin FeRh/Pt bilayer by a sub- picosecond thermal pulse. The numerical results suggest that the first-order phase transition from an antiferromagnetic to a ferromagnetic exchange inside the FePt induced by the rapid change in temperature is at the origin of the signal.

To describe the optical interaction of an elliptical polarized light source with the magnetic system, we developed a theoretical framework based on a double Λ system, called Landau-Lifshitz-Lambda model (LLL). In this model, the optical excitation emerges naturally from the equation of motion, instead of being introduced as an external effective field or via the coupled two temperature model. This makes the model a good candidate to describe the magnetization dynamics and switching in a wide range of magnetic materials subjected to any linear, circular, or elliptical polarized optical excitations.

The LLL model was used to study the helicity-dependent all optical switching and the helicity-dependent domain wall displacement observed experimentally in FePt and CoPt thin films. The simulations show that the optical excitation introduced in the LLL is able to induce a magnetization reversal in these kinds of material and to reproduce the characteristic features observed in the experiments, such as a switching ring and the optical displacement of a domain wall. The efficiency of the optical excitation is determined by the interplay of three effects: (i)

the ultra-fast demagnetization induced by a thermal laser pulse, (ii) the effective pumping introduced by the interaction between photons and spins, and (iii) the thermal relaxation taking place after the optical source has been removed.

The last chapter introduced a new stochastic form of the LLL equation, which is consistent with the solution of the Fokker-Planck equation associated to the Langevin form of the equation of motion for the magnetization. This new form was shown to be able to preserve the equilibrium value of the magnetization for magnetic particle of any size without neglecting the contribution of longitudinal fluctuations near the Curie point, making this new stochastic form appealing to multiscale atomistic/micromagnetic models or to study the signal statistics in high density recording system at elevated temperature.

In conclusion, the results outlined in this dissertation expand the range of knowledge on the interaction between light and magnetic system in the meso-scale. Understanding the physical origin of these optical induced excitation is paramount for the development of new magnetic sensors and logic devices. The introduced LLL reproduce qualitatively the results observed experimentally in ferromagnetic material. The work can be extended to accurately evaluate the optical parameters used in the equation through first principle computation or experiments. A natural extension of the work presented in this dissertation, is to derive the LLL equation for a two sublattice system to be able to study the optical excitation in ferrimagnetic material with strong spin-orbit coupling, such as GdFeCo and FeRh.

APPENDICES

APPENDIX A: VECTOR REPRESENTATION OF THE DENSITY OPERATOR FOR THE Λ SYSTEM

We consider the mathematical structure that leads to the decomposition of the density matrix into the components in Sec. IIA. Its difference from the standard decompositions as generalized Bloch vectors [65,98] and the physical consequences is detailed. The density matrix in Eq. (5.1) can be rewritten in terms of the linear combination of nine Hermitian operators,

$$\hat{\rho} = \frac{1}{2}\left[m_x \hat{\Sigma}_{12}^{x} + m_y \hat{\Sigma}_{12}^{y} + p_x \hat{\Sigma}_{23}^{x} + p_y \hat{\Sigma}_{23}^{y} + d_x \hat{\Sigma}_{13}^{x} + m_z \hat{\Sigma}_{12}^{z} + p_z \hat{\Sigma}_{23}^{z} + \hat{I}_{13} \right] . \tag{A.1}$$

The matrix representations of the Hermitian operators associated with the polarization components $m_x, m_y, p_x, p_y, d_x, d_y$ are, respectively,

$$\begin{aligned} \hat{\Sigma}_{12}^{x} &= \begin{bmatrix} 0 & 1 & 0 \\ 1 & 0 & 0 \\ 0 & 0 & 0 \end{bmatrix}, \quad \hat{\Sigma}_{12}^{y} = \begin{bmatrix} 0 & -i & 0 \\ i & 0 & 0 \\ 0 & 0 & 0 \end{bmatrix}, \quad \hat{\Sigma}_{23}^{x} = \begin{bmatrix} 0 & 0 & 0 \\ 0 & 0 & 1 \\ 0 & 1 & 0 \end{bmatrix} \\ \hat{\Sigma}_{23}^{y} &= \begin{bmatrix} 0 & 0 & 0 \\ 0 & 0 & i \\ 0 & -i & 0 \end{bmatrix}, \quad \hat{\Sigma}_{13}^{x} = \begin{bmatrix} 0 & 0 & 1 \\ 0 & 0 & 0 \\ 1 & 0 & 0 \end{bmatrix}, \quad \hat{\Sigma}_{13}^{y} = \begin{bmatrix} 0 & 0 & i \\ 0 & 0 & 0 \\ -i & 0 & 0 \end{bmatrix} \end{aligned} , \tag{A.2}$$

which are the same of the generators in the group SU(3) [99]. Our diagonal matrices associated with the coefficients $m_z, p_z, 1$ are

$$\hat{\Sigma}_{12}^{z} = \begin{bmatrix} 1 & 0 & 0 \\ 0 & -1 & 0 \\ 0 & 0 & 0 \end{bmatrix}, \quad \hat{\Sigma}_{23}^{z} = \begin{bmatrix} 0 & 0 & 0 \\ 0 & -1 & 0 \\ 0 & 0 & 1 \end{bmatrix}, \quad \hat{I}_{23}^{x} = \begin{bmatrix} 1 & 0 & 0 \\ 0 & 0 & 0 \\ 0 & 0 & 1 \end{bmatrix}, \tag{A.3}$$

These nine operators are the Pauli operators and a unit operator of the spin $1/2$ subspaces and may be regarded as a linearly independent set of basis states in a vector group.

The diagonal elements are not orthogonal but may be rendered so, for example, as the standard SU(3) generators [100].

We note that due to our definition for the vectors $\mathbf{m}$ and $\mathbf{p}$, in the case of full demagnetization, $\mathbf{m}=0$, and no polarization $\mathbf{p}=0$, an incoherent state $\hat{\rho}=1/2\cdot\hat{I}_{13}$ is observed in the subspace of states 1 and 3. This effect is in a contrast with the case of the standard generalized Bloch operators whose zero values lead to the no-coherence state of the density matrix with diagonal elements $1/3$. Thus, if we also call these polarization vectors "the generalized Bloch operators", it extends the meaning from the usual usage.

Our chosen generalized Bloch operators are under the restrictions of a Hermitian matrix representing a density matrix given by:

1) The unit trace condition $Tr(\hat{\rho})=1$, which is satisfied by the form of the diagonal elements in Eq. (A.3) involving only the longitudinal components m_z, p_z.

2) The condition of a positive matrix leads to

$$m_z \geq -1, \qquad p_z \geq -1, \qquad m_z + p_z \leq 0 \tag{A.4}$$

The inequality of $Tr(\hat{\rho}^2)\leq 1$ derived from the unit trace condition yields,

$$m^2 + p^2 + d^2 + m_z p_z + m_z + p_z \leq 2 \tag{A.5}$$

where m^2, p^2 are the squared magnitudes of the polarization vectors $\mathbf{m}$, $\mathbf{p}$, and d^2 is the squared magnitude of the truncated vector $(d_x, d_y, 0)$.

In the two-state system, the unit trace and positive requirements of the density matrix yields the same restriction as $Tr(\hat{\rho}^2)\leq 1$ for the Block vectors within a unit sphere with the pure states on the surface. Such a coincidence does not occur in systems with more than two states

since $Tr(\hat{\rho}^2) \le 1$ is a weaker condition than $Tr(\hat{\rho}) = 1$. This is seen in Fig. A-1, where the triangular domain inside the three lines given by Eq. (A.4) in the m_z, p_z plane when all the transverse (i.e., x, y) components of the polarization vectors are zero. The states on the triangle border are pure states and those inside are mixed states. The ellipse domain in the same m_z, p_z plane given by Eq.(A.5) contains but does not coincide with the triangular domain of legitimate states. This is similar to the sectional diagrams in the standard generalized Bloch vectors on p. 86 of Ref. [101], the difference being only the skewed basis of our density matrix. The relevant feature of the triangle in our case is that the three vertices $(m_z, p_z) = (-1,-1),(-1,1),(1,-1)$ correspond respectively to the initial magnetization state 2, the optically excited state 3 and the reversed magnetization state 1. The counterclockwise motion along the rims of the triangle is a possible dynamical path.

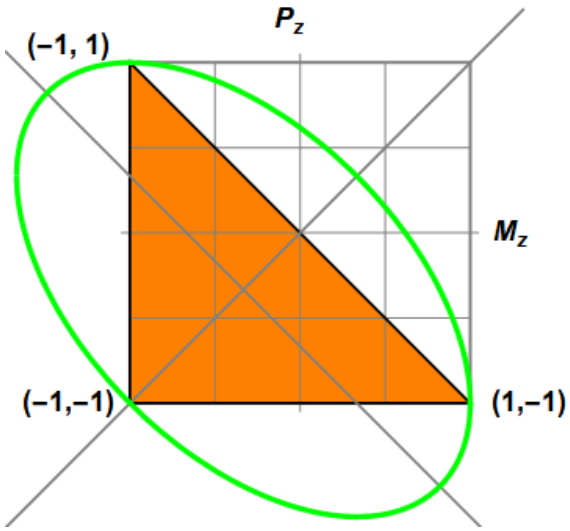

Figure A-1: The polarization cross-section (m_z, p_z) in the eight dimension polarization space. The ellipse centered at $(-1/3, 1/3)$ with the major axis in the $(-1,+1)$ direction and the minor axis along $(+1,+1)$ contains inside the region of $\mathrm{Tr}(\hat{\rho}^2) \le 1$. The valid density matrices are in the shaded region bound by the triangle with the vertices at the three pure states important to the optical processes, viz., the initial magnetization

state $|2\rangle$ at $(-1,-1)$, the optically excited state $|3\rangle$ at $(-1,+1)$ and the final magnetization reversal state $|1\rangle$ at $(+1,-1)$.

APPENDIX B: EQUATIONS OF MOTION

The equation of motion of the density matrix Eq. (5) is based on the formulation of the Lindblad operators [67] as the generators of the semigroup that is not time reversible. The evolution operators of the three state Hamiltonian form a unitary group SU(3) that is time reversible. The dissipation terms would drive the system only in the forward time direction and hence, the formulation is to utilize the semigroup of transformations which reflects the time direction for dissipative effects. The generators of the transformations are called the Lindblad operators. Explicit formulation of similar operators in N-state systems, especially $\mathrm{N}=2$, are given in Ref. [102] and are clearly explained in Ref. [103]. These generators simulate the dissipative and dephasing effects, which may be derived from the quantum dynamics of the quantum system plus its environment defined as a quantum system. When the environment system is traced out of the evolution operators, the rate results are given in terms the Kraus operators [104], which are modeled by the Lindblad operators. We model the equation of motion of the Λ system, as the dynamics of the open system by the formalism of Lindblad [67]. The relaxation from state 3 to state 1 with similar magnetization directions is powered by the electron-electron interaction, whose rate Γ_d is modeled by the Lindblad operator for dissipation, known as the longitudinal relaxation rate,

$$\hat{L}_d = \begin{bmatrix} 0 & 0 & \sqrt{L_d} \\ 0 & 0 & 0 \\ 0 & 0 & 0 \end{bmatrix}, \tag{B.1}$$

where $\sqrt{\Gamma_d}$ leads to the fast relaxation in the decay sector $|3\rangle \to |1\rangle$. The longitudinal relaxation rate is obtained by substituting $\hat{L}_k$ into the last term of Eq.(5.5). The longitudinal relaxation from state 3 back to 2 involves spin-orbit interactions and is much weaker than the fast $|3\rangle \to |1\rangle$ decay, and its contribution is neglected in the model.

While the longitudinal relaxation effect also produces a decoherence effect, i.e., the dissipation of the off-diagonal density matrix elements (the transverse polarization components), there is also a physical source of pure decoherence, known as dephasing. In the magnetization dynamics, the phase between the two magnetization states is randomized to a certain extent by the distributions of the two states, caused by the spin waves or Stoner-type low energy collective spin excitations [60,61]. The distributions of the three energies create the phase dissipation with the corresponding Lindblad operators,

$$\hat{L}_1 = \begin{bmatrix} \sqrt{L_1^*} & 0 & 0 \\ 0 & 0 & 0 \\ 0 & 0 & 0 \end{bmatrix}, \quad \hat{L}_2 = \begin{bmatrix} 0 & 0 & 0 \\ 0 & \sqrt{L_2^*} & 0 \\ 0 & 0 & 0 \end{bmatrix}, \quad \hat{L}_3 = \begin{bmatrix} 0 & 0 & 0 \\ 0 & 0 & 0 \\ 0 & 0 & \sqrt{L_3^*} \end{bmatrix}. \tag{B.2}$$

These operators cause changes only in the off-diagonal density matrix elements, i.e., the transverse optical polarization and magnetization operators, from Eq.(5.5):

$$\sum_{k=1}^{3}\left(\hat{L}_k \hat{\rho} \hat{L}_k^{\dagger} - \frac{1}{2}\left\{ \hat{L}_k^{\dagger} \hat{L}_k, \hat{\rho} \right\} \right) \Rightarrow - \begin{bmatrix} 0 & \Gamma_m^* \rho_{12} & \Gamma_d^* \rho_{13} \\ \Gamma_m^* \rho_{21} & 0 & \Gamma_o^* \rho_{23} \\ \Gamma_d^* \rho_{31} & \Gamma_o^* \rho_{32} & 0 \end{bmatrix}, \tag{B.3}$$

where the dephasing rates in the dissipation, optical, and magnetization channels are, respectively,

$$\begin{aligned}\Gamma_d^* &= \Gamma_3^* + \Gamma_1^* \\ \Gamma_o^* &= \Gamma_2^* + \Gamma_3^* \\ \Gamma_m^* &= \Gamma_1^* + \Gamma_2^*\end{aligned} \quad . \tag{B.4}$$

For the uniaxial magnetic anisotropy, the two magnetization states are equivalent and so, $\Gamma_1^* = \Gamma_2^*$. This leads to the use of $\Gamma^* = \Gamma_d^* = \Gamma_o^*$ in Eqs.(5.8)-(5.15). The magnetic sector Γ_m^* is omitted in the short time optical excitation phase.

APPENDIX C: ELLIPTICAL POLARIZED LIGHT

Any polarization can be seen as a combination of two waves: one left circularly polarized σ_+, and one right circularly polarized σ_-. Using the Jones vector, we can write any polarization as a combination of the two waves:

$$E = \frac{E^+}{\sqrt{2}}\begin{bmatrix}1\\ i\end{bmatrix} + \frac{E^-}{\sqrt{2}}\begin{bmatrix}1\\ -i\end{bmatrix} . \tag{C.1}$$

The final polarization of the light E is given by the relative contribution of the amplitude of the electric field produced by the contribution of component of the electric field produced by the left circularly polarized wave E^+ and the contribution of the electric field produced by the right circularly polarized wave E^-. In particular, if

- $E^- = 0$ and $E_+ \neq 0$: the light is left circularly polarized (σ_+);
- $E_+ = 0$ and $E_- \neq 0$: the light is right circularly polarized (σ_+);
- $E_+ = E_- \neq 0$: the light is linearly polarized (π),
- $E_- \neq E_+$ and $E^+, E^- \neq 0$ the light is elliptically polarized.

If we assume an ideal σ_+ polarized is placed in front of the incident elliptical polarized light, we can define the relative contribution of left and right circular polarized light using Malus's law. Given a laser intensity I_0 , the relative intensity of left circular polarized light is given by:

$$I_{\sigma_+} = I_0 f_{\sigma_+} \ , \tag{C.2}$$

$$I_{\sigma_-} = I_0 \left(1 - f_{\sigma_+}\right) = I_0 f_{\sigma_-} \ , \tag{C.3}$$

where f_{σ_+} is the fraction of light with σ_+ polarization and $f_{\sigma_-} = 1 - f_{\sigma_+}$ is the fraction of light with σ_- polarization. Using the relationship given in Eq. (C.2)-(C.3), it is possible to relate the amplitude of the electric field of the left circular polarization E^+ and the amplitude of the electric field of the right circular polarization E^- to the quarter wave plate angle used to generate the elliptical polarization as:

$$E^+(t) = \sqrt{\frac{2Z_0}{n} I(t) f_{\sigma_+}} \ , \tag{C.4}$$

$$E^-(t) = \sqrt{\frac{2Z_0}{n} I(t) f_{\sigma_-}} \ , \tag{C.5}$$

where $I(t)$ is the instantaneous intensity of the optical pulse absorbed inside of the material, $Z_0 \approx 120\pi\ \Omega$ is the impedance of free space, and n is the refractive index inside the media. Using the electric field so obtained it is possible to estimate the instantaneous Rabi frequency generated inside the material by the two waves $\sigma_\pm$ as:

$$\Omega_\pm(t) = \frac{2\mu_{14/23}}{\hbar} E^\pm(t) \ . \tag{C.6}$$

REFERENCES

[1] J. H. Van Vleck, The Theory of Electric and Magnetic Susceptibilities (Clarendon Press., 1932).

[2] W. F. B. Jr., Journal of Applied Physics 49, 1937 (1978).

[3] L. Landau and E. Lifshitz, (New York: Pergamon Press, 1965).

[4] T. L. Gilbert, IEEE Trans. Magn. 40, 3443 (2004).

[5] D. A. Garanin, Physical Review B 55, 3050 (1997).

[6] D. A. Garanin and O. Chubykalo-Fesenko, Physical Review B 70, 212409 (2004).

[7] R. F. L. Evans, D. Hinzke, U. Atxitia, U. Nowak, R. W. Chantrell, and O. Chubykalo-Fesenko, Physical Review B 85, 014433 (2012).

[8] R. E. Rottmayer, S. Batra, D. Buechel, W. A. Challener, J. Hohlfeld, Y. Kubota, L. Li, B. Lu, C. Mihalcea, and K. Mountfield, IEEE Trans. Magn. 42, 2417 (2006).

[9] T. Matsumoto, K. Nakamura, T. Nishida, H. Hieda, A. Kikitsu, K. Naito, and T. Koda, Applied Physics Letters 93, 031108 (2008).

[10] Y. Huai, AAPPS bulletin 18, 33 (2008).

[11] C.-H. Lambert, S. Mangin, B. C. S. Varaprasad, Y. Takahashi, M. Hehn, M. Cinchetti, G. Malinowski, K. Hono, Y. Fainman, and M. Aeschlimann, Science 345, 1337 (2014).

[12] J. Gorchon, C.-H. Lambert, Y. Yang, A. Pattabi, R. B. Wilson, S. Salahuddin, and J. Bokor, Applied physics letters 111, 042401 (2017).

[13] M. J. Donahue, OOMMF user's guide, version 1.0, 1999.

[14] G. Mollon and J. Zhao, Granular matter 14, 621 (2012).

[15] S. Fortune, Algorithmica 2, 153 (1987).

[16] M. Menarini, M. V. Lubarda, R. Chang, S. Li, S. Fu, B. Livshitz, and V. Lomakin, Journal of Magnetism and Magnetic Materials 482, 350 (2019).

[17] J. L. García-Palacios and F. J. Lázaro, Physical Review B 58, 14937 (1998).

[18] P. E. Kloeden and E. Platen, Numerical Solution of Stochastic Differential Equations (Springer Science & Business Medi, 1994).

[19] J. Mentink, M. Tretyakov, A. Fasolino, M. Katsnelson, and T. Rasing, Journal of Physics: Condensed Matter 22, 176001 (2010).

[20] N. Sukumar, in First MIT Conference on Computational Fluid and Solid Mechanics2001), p. 1667.

[21] N. Sukumar, International Journal for Numerical Methods in Engineering 57, 1 (2003).

[22] D. Weller, O. Mosendz, G. Parker, S. Pisana, and T. S. Santos, physica status solidi (a) 210, 1245 (2013).

[23] T. Seki, Y. Takahashi, and K. Hono, Journal of Applied Physics 103, 023910 (2008).

[24] C. H. Lambert, S. Mangin, B. S. D. C. S. Varaprasad, Y. K. Takahashi, M. Hehn, M. Cinchetti, G. Malinowski, K. Hono, Y. Fainman, M. Aeschlimann, and E. E. Fullerton, Science 345, 1337 (2014).

[25] D. Weller, G. Parker, O. Mosendz, E. Champion, B. Stipe, X. Wang, T. Klemmer, G. Ju, and A. Ajan, IEEE Trans. Magn. 50, 1 (2014).

[26] R. Chang, S. Li, M. Lubarda, B. Livshitz, and V. Lomakin, Journal of Applied Physics 109, 07D358 (2011).

[27] D. Wilton, S. Rao, A. Glisson, D. Schaubert, O. Al-Bundak, and C. Butler, IEEE Transactions on Antennas and Propagation 32, 276 (1984).

[28] D. Tzou, J. Beraun, and J. Chen, J. Heat Transfer 124, 284 (2002).

[29] D. Tzou, J. Chen, and J. Beraun, Journal of Thermal Stresses 28, 563 (2005).

[30] T. Qiu and C. Tien, (1993).

[31] J. Zhang, Y. Chen, M. Hu, and X. Chen, Journal of Applied Physics 117, 063104 (2015).

[32] J. Douglas Jr and S. Kim, Mathematical Models and Methods in Applied Sciences 11, 1563 (2001).

[33] J. Mendil, P. Nieves, O. Chubykalo-Fesenko, J. Walowski, T. Santos, S. Pisana, and M. Münzenberg, Scientific Reports 4, 3980 (2014).

[34] C. Burrowes, A. Mihai, D. Ravelosona, J.-V. Kim, C. Chappert, L. Vila, A. Marty, Y. Samson, F. Garcia-Sanchez, and L. Buda-Prejbeanu, Nature Physics 6, 17 (2010).

[35] C. Burrowes, D. Ravelosona, C. Chappert, S. Mangin, E. E. Fullerton, J. Katine, and B. Terris, Applied Physics Letters 93, 172513 (2008).

[36] H. Szambolics, J.-C. Toussaint, A. Marty, I. M. Miron, and L. Buda-Prejbeanu, Journal of Magnetism and Magnetic Materials 321, 1912 (2009).

[37] D.-H. Kim, S.-C. Yoo, D.-Y. Kim, K.-W. Moon, S.-G. Je, C.-G. Cho, B.-C. Min, and S.-B. Choe, Applied Physics Letters 104, 142410 (2014).

[38] J. Barker and R. W. Chantrell, Physical Review B 92, 094402 (2015).

[39] R. Khymyn, I. Lisenkov, V. Tiberkevich, B. A. Ivanov, and A. Slavin, Scientific Reports 7, 43705 (2017).

[40] I. Radu, C. Stamm, N. Pontius, T. Kachel, P. Ramm, J.-U. Thiele, H. Dürr, and C. Back, Physical Review B 81, 104415 (2010).

[41] C. Baldasseroni, C. Bordel, C. Antonakos, A. Scholl, K. H. Stone, J. B. Kortright, and F. Hellman, Journal of Physics: Condensed Matter 27, 256001 (2015).

[42] R. Khymyn, I. Lisenkov, V. Tiberkevich, B. A. Ivanov, and A. Slavin, Scientific Reports 7, 43705 (2017).

[43] H. Nakayama, K. Ando, K. Harii, T. Yoshino, R. Takahashi, Y. Kajiwara, K.-i. Uchida, Y. Fujikawa, and E. Saitoh, Physical Review B 85, 144408 (2012).

[44] G. Ju, J. Hohlfeld, B. Bergman, R. J. van de Veerdonk, O. N. Mryasov, J.-Y. Kim, X. Wu, D. Weller, and B. Koopmans, Physical review letters 93, 197403 (2004).

[45] I. Tudosa, C. Stamm, A. B. Kashuba, F. King, H. C. Siegmann, J. Stöhr, G. Ju, B. Lu, and D. Weller, Nature 428, 831 (2004).

[46] C. Stanciu, F. Hansteen, A. Kimel, A. Kirilyuk, A. Tsukamoto, A. Itoh, and T. Rasing, Physical review letters 99, 047601 (2007).

[47] I. Radu, K. Vahaplar, C. Stamm, T. Kachel, N. Pontius, H. Dürr, T. Ostler, J. Barker, R. Evans, and R. Chantrell, Nature 472, 205 (2011).

[48] T. A. Ostler, J. Barker, R. F. L. Evans, R. W. Chantrell, U. Atxitia, O. Chubykalo-Fesenko, S. El Moussaoui, L. Le Guyader, E. Mengotti, L. J. Heyderman, F. Nolting, A. Tsukamoto, A. Itoh, D. Afanasiev, B. A. Ivanov, A. M. Kalashnikova, K. Vahaplar, J. Mentink, A. Kirilyuk, T. Rasing, and A. V. Kimel, Nature Communications 3, 666 (2012).

[49] Y. K. Takahashi, R. Medapalli, S. Kasai, J. Wang, K. Ishioka, S. H. Wee, O. Hellwig, K. Hono, and E. E. Fullerton, Physical Review Applied 6, 054004 (2016).

[50] M. O. A. Ellis, E. E. Fullerton, and R. W. Chantrell, Scientific Reports 6, 30522 (2016).

[51] R. John, M. Berritta, D. Hinzke, C. Müller, T. Santos, H. Ulrichs, P. Nieves, J. Walowski, R. Mondal, and O. Chubykalo-Fesenko, Scientific reports 7, 4114 (2017).

[52] R. Medapalli, D. Afanasiev, D. K. Kim, Y. Quessab, S. Manna, S. A. Montoya, A. Kirilyuk, T. Rasing, A. V. Kimel, and E. E. Fullerton, Physical Review B 96, 224421 (2017).

[53] K. Hild, J. Maul, T. Meng, M. Kallmayer, G. Schönhense, H. J. Elmers, R. Ramos, S. K. Arora, and I. V. Shvets, Journal of Physics: Condensed Matter 20, 235218 (2008).

[54] Z. H. Cen, B. X. Xu, J. F. Hu, J. M. Li, K. M. Cher, Y. T. Toh, K. D. Ye, and J. Zhang, Optics Express 21, 9906 (2013).

[55] J. Holzrichter, R. Macfarlane, and A. Schawlow, Physical Review Letters 26, 652 (1971).

[56] P. S. Pershan, J. P. van der Ziel, and L. D. Malmstrom, Physical Review 143, 574 (1966).

[57] J. Van der Ziel, P. Pershan, and L. Malmstrom, Physical Review Letters 15, 190 (1965).

[58] M. S. El Hadri, P. Pirro, C. H. Lambert, S. Petit-Watelot, Y. Quessab, M. Hehn, F. Montaigne, G. Malinowski, and S. Mangin, Physical Review B 94, 064412 (2016).

[59] Y. Quessab, R. Medapalli, M. S. El Hadri, M. Hehn, G. Malinowski, E. E. Fullerton, and S. Mangin, Physical Review B 97, 054419 (2018).

[60] I. Galanakis and E. Şaşıoğlu, Journal of Materials Science 47, 7678 (2012).

[61] J. Glazer and E. Tosatti, Solid state communications 52, 905 (1984).

[62] M. O. Scully and M. S. Zubairy, Quantum Optics (Cambridge University Press, Cambridge, 1997).

[63] M. Yamanoi and J. H. Eberly, JOSA B 1, 751 (1984).

[64] P. R. Berman and R. G. Brewer, Physical Review A 32, 2784 (1985).

[65] R. A. Bertlmann and P. Krammer, Journal of Physics A: Mathematical and Theoretical 41, 235303 (2008).

[66] S. A. Werner, R. Colella, A. W. Overhauser, and C. Eagen, Physical Review Letters 35, 1053 (1975).

[67] G. Lindblad, Communications in Mathematical Physics 48, 119 (1976).

[68] Ł. Cywiński and L. J. Sham, Physical Review B 76, 045205 (2007).

[69] G. P. Zhang and T. F. George, Physical Review B 78, 052407 (2008).

[70] A. F. Bartelt, A. Comin, J. Feng, J. Nasiatka, T. Eimüller, B. Ludescher, G. Schütz, H. A. Padmore, A. Young, and A. Scholl, Applied physics letters 90, 162503 (2007).

[71] A. R. Khorsand, M. Savoini, A. Kirilyuk, A. V. Kimel, A. Tsukamoto, A. Itoh, and T. Rasing, Physical Review Letters 108, 127205 (2012).

[72] V. N. Gridnev, Physical Review B 88, 014405 (2013).

[73] D. Cheskis, A. Porat, L. Szapiro, O. Potashnik, and S. Bar-Ad, Physical Review B 72, 014437 (2005).

[74] M. Krauß, T. Roth, S. Alebrand, D. Steil, M. Cinchetti, M. Aeschlimann, and H. C. Schneider, Physical Review B 80, 180407(R) (2009).

[75] G. Zhang, M. Si, and T. F. George, Journal of Applied Physics 117, 17D706 (2015).

[76] A. Schmidt, M. Pickel, M. Donath, P. Buczek, A. Ernst, V. Zhukov, P. Echenique, L. Sandratskii, E. Chulkov, and M. Weinelt, Physical review letters 105, 197401 (2010).

[77] P. Scheid, G. Malinowski, S. Mangin, and S. Lebègue, Physical Review B 100, 214402 (2019).

[78] D. Y. Tzou, Macro- to Microscale Heat Transfer: The Lagging Behavior (Wiley, 2015), pp. 13-15.

[79] E. Turgut, D. Zusin, D. Legut, K. Carva, R. Knut, J. M. Shaw, C. Chen, Z. Tao, H. T. Nembach, and T. J. Silva, Physical Review B 94, 220408 (2016).

[80] A. P. Caffrey, P. E. Hopkins, J. M. Klopf, and P. M. Norris, Microscale Thermophysical Engineering 9, 365 (2005).

[81] J. Hohlfeld, S. S. Wellershoff, J. Güdde, U. Conrad, V. Jähnke, and E. Matthias, Chemical Physics 251, 237 (2000).

[82] A. Lyberatos and K. Y. Guslienko, Journal of applied physics 94, 1119 (2003).

[83] P. H. Q. Pham, W. Zhang, N. V. Quach, J. Li, W. Zhou, D. Scarmardo, E. R. Brown, and P. J. Burke, Nature Communications 8, 2233 (2017).

[84] W. Hsu and R. H. Victora, IEEE Trans. Magn. 55, 1 (2019).

[85] J. Miao and D. Wei, IEEE Trans. Magn. 55, 1 (2019).

[86] S. Hernández, P. Krivosik, P. Huang, W. R. Eppler, T. Rausch, and E. Gage, IEEE Trans. Magn. 52, 1 (2016).

[87] N. Kazantseva, D. Hinzke, U. Nowak, R. W. Chantrell, U. Atxitia, and O. Chubykalo-Fesenko, Physical Review B 77, 184428 (2008).

[88] L. Xu and S. Zhang, Journal of Applied Physics 113, 163911 (2013).

[89] H. Li, M. Alex, and J. J. Zhu, IEEE Trans. Magn. 51, 1 (2015).

[90] G. Zhang and T. F. George, Journal of Physics: Condensed Matter 25, 366002 (2013).

[91] A. Lyberatos, D. V. Berkov, and R. W. Chantrell, Journal of Physics: Condensed Matter 5, 8911 (1993).

[92] O. Chubykalo, R. Smirnov-Rueda, J. Gonzalez, M. Wongsam, R. W. Chantrell, and U. Nowak, Journal of magnetism and magnetic materials 266, 28 (2003).

[93] I. Bashkirtseva and L. Ryashko, Physics Letters A 380, 3359 (2016).

[94] R. F. Evans, W. J. Fan, P. Chureemart, T. A. Ostler, M. O. Ellis, and R. W. Chantrell, Journal of Physics: Condensed Matter 26, 103202 (2014).

[95] L. Xu and S. Zhang, Physica E: Low-Dimensional Systems and Nanostructures 45, 72 (2012).

[96] H. Li, M. Alex, and J.-G. J. Zhu, IEEE Transactions on Magnetics 51, 1 (2015).

[97] M. Menarini and V. Lomakin, arXiv preprint arXiv:2001.02403 (2020).

[98] G. Kimura, Physics Letters A 314, 339 (2003).

[99] M. Gell-Mann, Physical Review 125, 1067 (1962).

[100] M. Gell-Mann and Y. Ne'eman, THE EIGHTFOLD WAY: A Review-With A Collection of Reprints (W. A. Benjnmin, Inc., 1964).

[101] G. Mahler and V. A. Weberruß, Quantum Networks - Dynamics of Open Nanostructures (Springer, 1998).

[102] V. Gorini, A. Kossakowski, and E. C. G. Sudarshan, Journal of Mathematical Physics 17, 821 (1976).

[103] B. Schumacher and M. Westmoreland, Quantum processes systems, and information (Cambridge University Press, 2010).

[104] K. Kraus, States, Effects, and Operations Fundamental Notions of Quantum Theory (Springer-Verlag).